Fall 2017

Study of Modified Deposition Process for Cu(In,Ga)Se2 Solar Cell Back Contact

Tasnuva Ashrafee
Old Dominion University

Recommended Citation

Ashrafee, Tasnuva. "Study of Modified Deposition Process for Cu(In,Ga)Se2 Solar Cell Back Contact" (2017). Doctor of Philosophy (PhD), dissertation, Electrical/Computer Engineering, Old Dominion University, DOI: 10.25777/n77c-2668
https://digitalcommons.odu.edu/ece_etds/24

STUDY OF MODIFIED DEPOSITION PROCESS FOR Cu(In,Ga)Se_2 SOLAR CELL BACK CONTACT

By

Tasnuva Ashrafee
M. S. 2008, University of Dhaka

A Dissertation Proposal Submitted to the Faculty of
Old Dominion University in Partial Fulfillment of the
Requirements for the Degree of

Doctor of Philosophy

ELECTRICAL AND COMPUTER ENGINEERING

OLD DOMINION UNIVERSITY
December 2017

Approved by:

Sylvain Marsillac (Director)

Mounir Laroussi (Member)

Christopher Bailey (Member)

Orlando Ayala (Member)

ABSTRACT

Study of Modified Deposition Process for Cu(In,Ga)Se_2 Solar Cell Back Contact

Tasnuva Ashrafee
Old Dominion University, 2017
Director: Dr. Sylvain Marsillac

As the worldwide demand for renewable energy is increasing, growth of the global share of alternative energy sources would improve overall energy security as well as bring environmental benefits. So far, solar cells - the devices that convert direct sunlight into electricity - are dominated by silicon devices. Another alternative is thin film solar cell, whose main inspiration is to reduce the electricity production cost. Cu(In, Ga)Se_2 (CIGS) solar cells are considered to have a great prospective because of reduced material and energy consumption during manufacturing. Many CIGS solar cell manufacturers are already exhibiting GW-scale production capacity. With the development of CIGS applications, it is essential to modify the properties of each of the constituent material to adapt to the new requirements.

Molybdenum is the most appropriate material used as the back contact for CIGS solar cells, and is commonly deposited by sputtering onto soda lime glass (SLG). Mo thin films act as the metal contact. The formation of an Ohmic contact at the Mo/CIGS interface is one of the most important properties apart from high conductivity, strong adhesion of the film as well as chemical and mechanical compatibility with the CIGS layer. A suitable amount of sodium is necessary for enhanced solar cell performance. When using soda lime glass (SLG) as a sodium source, the Mo layer acts like a barrier for sodium diffusion and the deposition process provides proper control of sodium supply from the SLG. Structural,

thermal, and chemical properties of the Mo film have a direct influence on the growth and nucleation of the CIGS layer as well.

In the first part of the thesis, *in-situ* and e*x-situ* characterization techniques were used to understand the growth, as well as the morphology and structural properties of the Mo films grown on various substrates, namely Si (100) wafer, soda lime glass and borosilicate glass, at a fixed deposition power and pressure. Real time spectroscopic ellipsometry (RTSE) analysis demonstrated a Volmer-Weber growth mechanism for all films. Dielectric functions extracted from the ex-situ analysis illustrate a Drude oscillator, characteristic of metals. Resistivity values were extracted from this oscillator and correlated with Hall Effect and 4-point probe measurements. Substrates with sodium produced slightly less resistive films. AFM images showed that the films were deposited conformally on the substrates, and that the roughness of the films was inversely related to the resistivity values. XRD analysis showed that all the Mo films deposited were preferentially oriented along the (110) direction regardless of the substrates. SEM surface images showed good correlation with XRD analysis. Na depth profiles, obtained by SIMS analysis, were then compared for Mo/CIGS structures deposited on SLG and BSG. A clear difference between the two was seen with a much higher intensity of Na for the SLG substrates. Devices were then fabricated on both substrates and analyzed by J-V and QE measurements. Even though no change occurred for the current, a clear decrease in V_{OC} and FF was observed for the BSG substrate compared to the SLG substrate.

The influence of the substrate temperature (T_{SS}) at a fixed deposition power and pressure was studied in the second part of this thesis. Correspondence between the X-ray diffraction (XRD), four-point probe resistivity measurements, and SEM analysis are presented. Films deposited at a higher substrate temperature exhibit better crystallinity, lower sheet resistance and larger grain size. Secondary ion mass spectrometry (SIMS) demonstrated the influence of substrate temperature on sodium diffusion. X-ray photoelectron spectroscopy (XPS) analysis was performed on the films to understand the molybdenum oxidation states as a function of substrate temperature. Theoretical simulation models were developed to further understand the sodium diffusion, allowing extraction of $D_{boundary}$ and D_{grain} for the first time.

The third objective of this thesis was to focus on the effect of substrate temperature on the traditional bilayer molybdenum films used as the back contact for CIGS solar cells, where the first layer is deposited at comparatively higher pressure to fabricate porous films to allow better adhesion of the films and the 2nd layer is deposited at relatively lower pressure to produce denser films with better electrical properties. These films were subject to post-deposition annealing and both as-deposited and annealed films were investigated with XRD, SIMS, AFM and Hall Effect measurement. The films deposited at T_{SS} of 100°C were found to be outliers after an in depth examination. Solar cells were fabricated using these different substrate temperatures to study the effect on the device parameters. The device analysis reveals that the room temperature device exhibits better device efficiency, mostly because of lower series resistance and reverse saturation current. Improvement in electrical properties for higher deposition temperature was not assisted by higher sodium diffusion in the film, therefore no noteworthy changes were witnessed from the devices performance, specifically for V_{OC} and FF.

This dissertation is dedicated to all those who have the courage to dream and the tenacity to make it real.

ACKNOWLEDGEMENTS

I would like to express my genuine gratitude and heartfelt acknowledgement to Dr. Sylvain Marsillac, my PhD advisor for his exceptional support and irreplaceable guidance for my project. I am extremely grateful to Dr. Marsillac for his advice and inspiration and encouragement throughout the entire time of this research project and in the course of the writing of this dissertation. His direction and guidance have driven me profoundly to be not only believe in myself and work hard to be a better scientist but also a better human being in my life.

I am grateful to my committee members Dr. Mounir Laroussi, Dr. Christopher Bailey, and Dr. Orlando Ayala for their valuable time, vital suggestions and feedbacks. I would like to thank the former and current Graduate Program Director, Dr. Dimitrie Popescu and Dr. ChunSheng Xin respectively for supporting me immensely to complete my doctoral studies. I would like to show my thankfulness to Dr. Khan Iftekharuddin for having faith in me and support me to complete my studies.

I also would like to show my gratitude to all of my previous and current research teammates, Dr. Yunus Erkaya, Dr. Krishna Aryal, Dr. Patrick Boland, Dr. Vikash Ranjan, Grace Rajan, and Shankar Karki.

I would like to thank my beloved family and valuable friends for their immeasurable support throughout my educational accomplishments. Without their boundless love and kind support I would be lost.

TABLE OF CONTENTS

LIST OF TABLES

LIST OF FIGURES

Figure Page

Figure Page

Figure Page

Figure Page

Figure Page

CHAPTER 1

INTRODUCTION

1.1 Motivation and Background

With increasing population along with economic development all around the world, global energy demand is expected to escalate continuously every year. Approximately 30 TWh of energy is required by the end of 2050, this is necessary so that the energy demand is fulfilled with time. Currently most of these energy demands are fulfilled by burning fossil fuels, for instance, coal, petroleum, and natural gas. The peak supply of these energies from conventional resources has been achieved by now or is about to be achieved within the next 20-30 years [1]. In addition, the greenhouse gases produced from the burning of fossil fuels considerably affect the environment and will threaten human survival in the future. To fulfill these future energy requirements, we need to develop and deploy environmentally friendly renewable sources of energy such as solar energy. Hydroelectric, geothermal, biomass, wind, and solar energy are a few among many available renewable energy resources, which are not only abundant sources but are also cleaner. U.N. studies show that around 120,000 TW of solar power is absorbed by Earth's surface every year, which is 10,000 times the existing annual requirement of energy [2]. At present time, the price of electricity produced from conventional sources in the USA is on average ~ \$0.10/kWh while electricity from PV plants costs roughly \$0.27/kWh [3]. However, the electricity cost from conventional sources will continue to increase where the electricity from PV is decreasing due to the advancement of the technology, which results in improved efficiency and large scale utilities. “Grid parity” which is the cross over between these prices, will take place in the near future and has occurred in particular locations or applications [4].

Numerous technology choices exist currently to harvest the power of the sun, a sustainable energy source, and produce electricity directly from this source by means of the photovoltaic effect. Among them, $Cu(In,Ga)Se_2$ has achieved substantial momentum as a potential high efficiency and low cost thin film solar cell material. With 22.6% efficiency, $Cu(In,Ga)Se_2$ (CIGS) solar cells are the most efficient polycrystalline thin films solar cells at present [5]. In addition to high conversion efficiencies, CIGS cells have proved to have enduring outdoor stability and radiation hardness [6-7]. The capacity to scale up any photovoltaic technology is one of the measures that will define its long-term sustainability. Several manufacturers such as Solar Frontier, Miasolé, and Solibro are showing the way for GW-scale production capacity in the case of CIGS solar modules.

1.2 Solar Cell Background

A solar cell is a semiconductor device, which converts sunlight into electrical energy by generating current and voltage**.** This conversion process always involves: a) electron-hole pairs (e-h) generation in the semiconductor materials by absorbing the incident photon with an energy (E_{ph}) greater than or equal to the band gap (E_g) of the materials, (b) separation of these light generated e-h pairs via some internal mechanism, and (c) collection of these carriers by appropriate electrodes connected in the external circuit. A p-n junction is one of the extensively used structures for separating the photogenerated e-h pairs.

For converting incident sunlight into electrical power, photons from a range of energies are required to create electron-hole pairs. An electron-hole pair is generated as long as the energy of the incident photon is sufficient to overcome the band gap of the materials. Nevertheless, for solar cell applications, photon energy greater than the band gap is lost in the form of thermalization. The current-density vs. voltage (J-V) characteristics of the solar cells measured in the dark resemble the exponential response of a diode with higher current under the forward bias and smaller current under reverse bias condition. Under illumination, there is also a photocurrent in the cell, which flows in the opposite direction of the dark current and the J-V characteristics are obtained by the superposition of the dark characteristics and the photocurrent. The diode equation under illumination [9] is given by:

$$J = J_0 \left(e^{qV/AKT} - 1 \right) - J_{ph} \tag{1.1}$$

where J is the current density, V is the applied voltage, J_0 is the reverse saturation current density of the diode, J_{ph} is the photocurrent density, q is the elementary charge, A is the ideality factor, k is the Boltzmann constant, and T is the temperature.

Figure 1.1 displays the J-V characteristics of a solar cell under illumination illustrating the most important performance parameters such as the open circuit voltage (V_{oc}), the short circuit current density (J_{sc}), the fill factor (FF), and the maximum power point with maximum voltage and current density of V_{MP} and J_{MP} respectively. The equations involving the above parameters to the power conversion efficiency (PCE) are also provided.

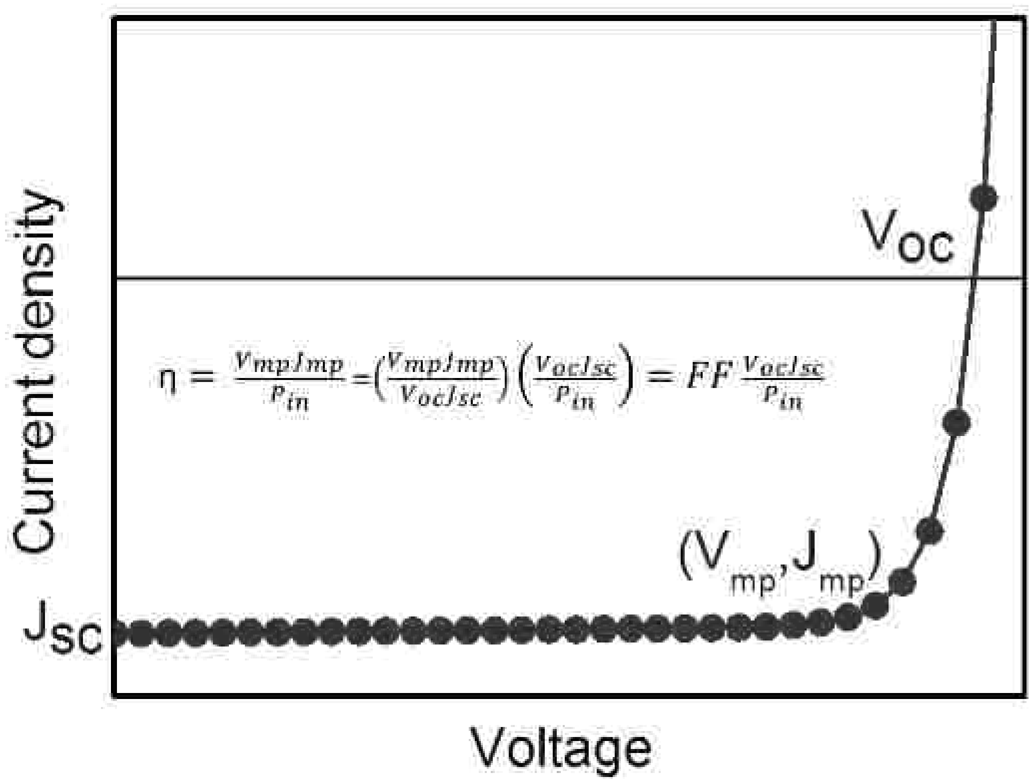

Figure 1.1: J-V characteristics of a solar cell under illumination showing the open circuit voltage (V_{oc}), the short circuit current (I_{sc}) and the maximum power point with maximum voltage and current of V_{mp} and Imp respectively.

1.2.1 Short-circuit Current Density

The short-circuit current density, J_{SC}, is the maximum current density through the solar cells at zero voltage, which is similar to the condition when the two electrodes of the cell are short-circuited together. When V=0, no power is generated at this point since power is the product of current and voltage, however J_{sc} marks the onset of power generation. J_{sc} of a solar cell is determined by the incident photon flux density, which depends on the spectrum of the incident light. The maximum current that can be generated by the solar cell is strongly related to the optical properties, such as absorption in the absorber layer and other layers, shadowing and total reflection of the solar cell.

1.2.2 Open-circuit Voltage

The open-circuit voltage, V_{OC}, is the voltage at which no current flows through the solar cell, which is similar to the condition when the device is open-circuited. This is the optimum voltage that a cell can provide. When J= 0, no power is produced but it marks the limit for voltages at which power can be generated. The V_{OC} relates to the amount of voltage under forward bias condition at which the dark current compensates the photocurrent in the solar cell. The V_{OC} can be calculated from the equation provided below, where it was assumed that that the net current is zero:

$$V_{OC} = \frac{AkT}{q} ln\left(\frac{J_{ph}}{J_o} + 1\right) \qquad (1.2)$$

where kT/q is the thermal voltage, J_{ph} is the photocurrent density and J_0 is the reverse saturation current density.

The above equation demonstrates that V_{OC} is influenced by two parameters: the reverse saturation current and the light generated current in the solar cell. Since J_{ph} tends to not have a significant deviation, the main effect on V_{OC} is the reverse saturation current, which may differ by orders of magnitude. The reverse saturation current density, J_0, is related to the recombination in the solar cell, so V_{OC} is very sensitive to the amount of recombination in the cell.

1.2.3 Fill Factor

The fill factor is expressed as the ratio of the maximum power ($P_{max} = J_{mp}$ x V_{mp}) generated by the solar cell to the product of V_{OC} and $J_{SC.}$

$$FF = \frac{J_{mp}V_{mp}}{J_{SC}V_{OC}} \qquad (1.3)$$

It specifies how close J_{mp} and V_{mp} come to the boundaries of power generation of J_{sc} and V_{oc}. It also indicates the sharpness of the J-V curve that links J_{sc} and V_{oc}. High FF is always preferred as this indicates higher maximum power however the diode-like characteristics of solar cells results in FF always being less than one.

1.2.4 Power Conversion Efficiency

The most commonly used parameters to compare the performance of a solar cell is the power conversion efficiency, which is defined as the ratio of energy output from the solar cells to input energy from the sun. The efficiency of a solar cell is determined as

$$\eta = \frac{P_{max}}{P_{in}} = \frac{J_{mp}V_{mp}}{P_{in}} = \frac{V_{OC}J_{SC}\,FF}{P_{in}} \tag{1.4}$$

The above equation evidently demonstrates that FF, J_{sc}, and V_{oc} have direct effects on the efficiency, η. Since the device area used to calculate J will impact the efficiency of the cell, the inactive part of the device such as grids and interconnects should be counted in while calculating the efficiency for large area devices or modules. The efficiency of the solar cells is also influenced by the power and spectrum of the incident light source and the temperature of the solar cell, as solar cells do not absorb and convert photons into electrons at all wavelengths in the same manner and efficiency. So while comparing various solar cells, all the conditions under which the conversion efficiency of the cell is measured should be controlled with caution. Although the solar spectrum at the earth's surface differs based on location, clouds coverage and other factors, the AM1.5 G spectrum shown in Figure 1.2 is the most frequently used standard spectrum to measure and compare the performance of photovoltaic devices. The term air mass intensity (AM) is generally used to represent the ratio of the optical path to a normal path at sea level on a cloudless day and expressed with the following equation:

$$AM = \frac{1}{Cos\theta} \tag{1.5}$$

where θ is the angle of the path Sun light travels with respect to the vertical. If θ is 48.19^0 then AM condition is denoted as AM 1.5 (AM=1/Cos (48.19) = 1.5). So the AM 1.5 is equivalent to the sunlight passing through 1.5 times the air mass of vertical illumination (AM 1). The term G represents “global”, where both direct and indirect illumination are taken into consideration.

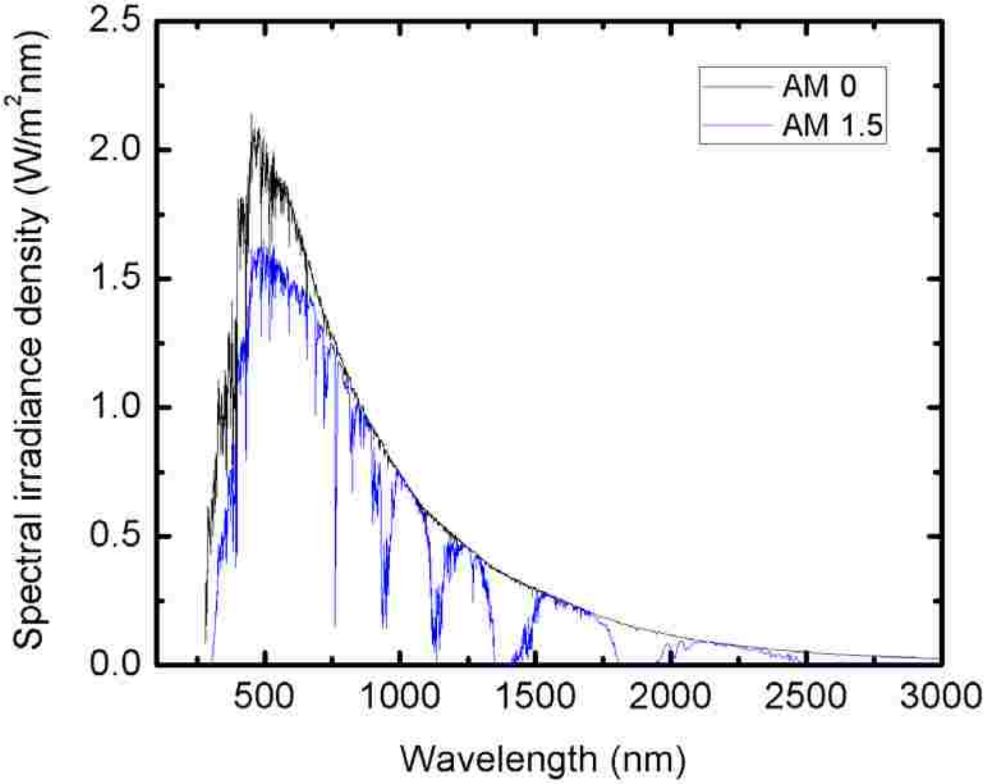

Figure 1.2: Spectral irradiation densities: AM1.5 irradiation (blue), AM0 irradiation (black).

1.2.4 Practical Requirements for a Solar Cell Material

Various materials are available that show the photovoltaic effect and can be taken into account for solar cell manufacturing. However, materials for efficient solar cells require to fulfill several necessities for instance i) materials used for practical PV application must have optical properties matched to the spectrum of the available light, ii) the materials need to be economical, benign, and available in abundance, iii) the PV device fabrication process should be fast, low-cost, and eco-friendly, and iv) the PV device must have reliable performance for outdoor application for a long period of time.

1.3 Overview of Progress in Photovoltaic (PV) Technology

1.3.1 Introduction

The utilization of the sun’s energy to convert into electricity started two centuries ago. In 1839, Alexandre-Edmond Becquerel reported the photovoltaic effect. He observed that electric current can be produced by exposing two metal electrodes to light which are immersed in a conducting solution. Willoughby Smith found the photo-conductivity of solid selenium in 1873 [12]. In the 1950s, a single crystal silicon photovoltaic cell with efficiency around 6 % was fabricated by Calvin Fuller, Daryl Chapin, and Gerald Pearson at the Bell Laboratories [13]. Since then, as the advancements in the technology continues, semiconductor based devices have been developed to make more efficient solar cells. They are categorized into three generations known as First, Second, and Third generation of photovoltaic technology.

1.3.2 First Generation PV

First generation photovoltaic cells are wafer based single junction solar cells, which are comprised of crystalline silicon (c-Si) and crystalline GaAs. Silicon cells and modules are the leading technology in the solar cell market, accounting for more than 86% of the solar cells production. However, production cost is the major challenge because of the requirement of high purity materials to eliminate recombination issues, although much improvement have been accomplished in recent years with module costs reduced to below

\$0.6/W. These silicon semiconductors, used in commercial manufacturing, permit power conversion efficiencies up to 25%, despite the fact that the fabrication technologies at the present time set a limit of efficiencies to about 15 to 20% [14]. C-Si is an indirect band gap material with a band-gap value of ~ 1.17 eV, which leads to some issues: it is a poor absorber of sunlight and requires comparatively thicker layers in the order of hundreds of microns so that most of the incident light is absorbed.

GaAs is a direct band gap material with a value of 1.4 eV. Band gap tunability is possible to achieve by adding Al and forming (Al,Ga)As materials. Conversion efficiencies of 30% to 45% for single and multi-junction devices, respectively, make this technology the most efficient among any technology in any generation and a very good apparent choice. However, the manufacturing cost is high due to the high purity requirements (similar to c-Si technology) and the fabrication process. It can be observed that second generation technology has the benefit of being much more flexible during the manufacturing process. The high cost of GaAs cells during manufacturing is the reason behind the applications for this technology being limited to space applications such as satellite and space stations.

1.3.3 Second Generation PV

In order to achieve the demand of lower cost and enhanced large scale manufacturing, a second generation PV, also called thin films PV, has been established. Three types of solar cells are considered in this generation, namely Cadmium Telluride (CdTe), Copper indium gallium diselenide (CIGS) and amorphous silicon (a-Si). These thin films are better absorbers of the solar spectrum compared to c-Si and require only a couple of microns of active materials in energy conversion. It also allows deposition technique that increase the unit of manufacturing by a factor of 100 from first generation

PV i.e. Silicon wafer (~ 100 cm^2) to a glass sheet (~ 1 m^2) [15]. The recorded efficiency of CIGS (22.6%) [5] and CdTe (22.1 %) [14] has given sufficient demonstration of the potential of thin-film PV. Even though the development of second generation PV is slower than anticipated, it still has excellent potential to lower the manufacturing cost of PV in large-scale production by cutting down on material usage.

1.3.4 Third Generation PV

The primary goal of third generation PV is to reduce the production costs to lower than that of second generation PV, either by increasing the efficiency or reducing the manufacturing costs. In order to accomplish such progress in efficiency, PV technology is looking for a method to overcome the Shockley-Queisser limit of 31-41% efficiency for single-band gap devices [16]. The most crucial power-loss mechanism in single band gap cells is the lack of ability to absorb incident light with the energy less than the band gap and thermalization of light energies beyond the band gap. These two loss mechanisms can possibly be addressed by developing a series of new device structure based on state-of-the-art technologies. These new devices comprise multi-junction/tandem cells, quantum dot cells, intermediate band solar cells, hot-carrier cells, and organic cells (including polymer and dye-sensitized solar cells). A new idea based on ‘inorganics-organics’ structure delivers improved solar cell efficiency compared to that of purely organic devices. The hybrid active materials combining low cost conducting polymers films (organic) and the stability in lifetime of the novel nano-structure (inorganic) increases the harvesting cross-section, the charge dissociation and charge transport within the PV devices [10]. These new devices primarily consist of mNPs, metal oxides, nano-hybrids, and carbon nanostructures. The development in the major solar cell technologies in terms of efficiency is shown in Figure 1.3.

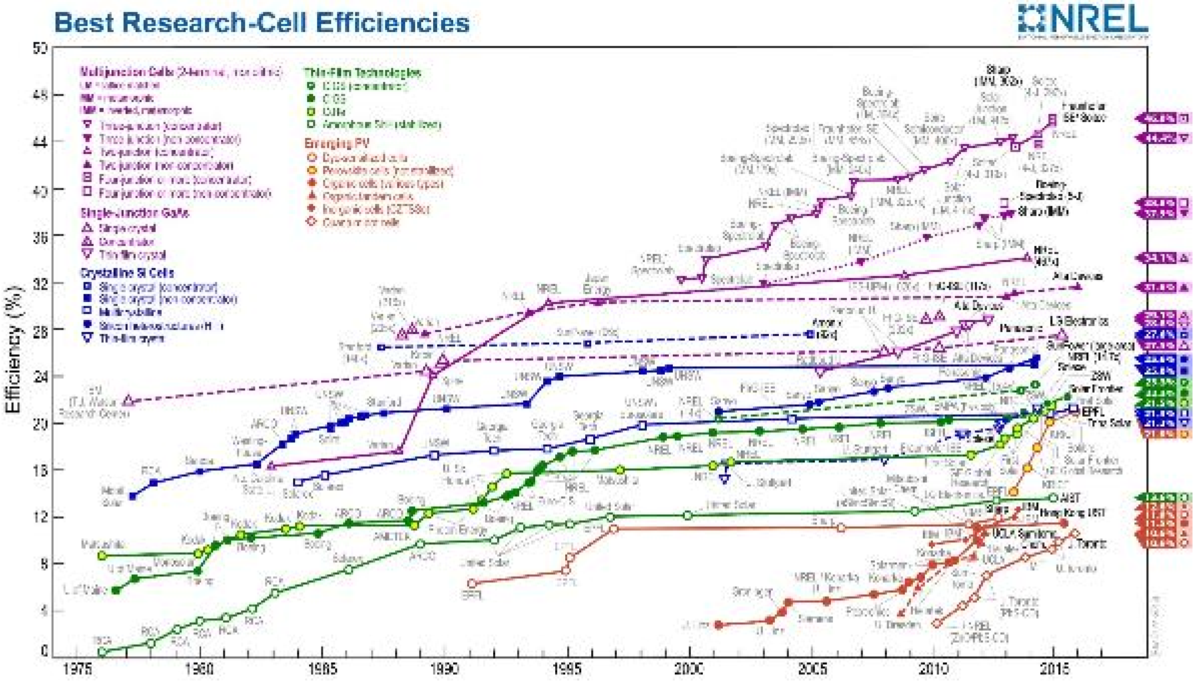

Figure 1.3: Evolution of the solar cell efficiency and technology over the past 40 years [11].

1.4. CIGS Properties

1.4.1 Structural and Compositional Properties

Cu(In,Ga)Se_2 forms a quaternary compound when Indium (In) atoms are partially substituted by Gallium (Ga) atoms in the $CuInSe_2$ ternary system. The CIGS possess a chalcopyrite tetragonal structure, comparable to that of the $CuInSe_2$ structure as depicted in Figure 1.4. The tetragonal structure of the chalcopyrite compound can be described as a super lattice Zinc Blende structure by stretching the unit cube along the z-axis twice the length that turns into the c-axis of the chalcopyrite structure [18]. The ratio of the tetragonal lattice parameters c/a, which is called tetragonal deformation, is close to 2 and varies due to the difference in bond strength in Cu-Se, In-Se or Ga-Se. So, the c/a ratio is a function of $x \equiv Ga/(In+Ga)$, where $c/a>2$ for $x = 0$ and $c/a<2$ for $x = 1$.

CIGS can be either p-type or n-type depending on the dominant defects. Usually, n-type CIGS is grown under Cu-rich and Se-deficient environment whereas p-type CIGS is grown under Cu-poor and Se-rich environment [19]. Thus Se vacancy (V_{Se}) and Cu vacancy (V_{Cu}) are believed to be the dominant defects in n- and p-type CIGS respectively [19]. P-type CIGS thin films are used as absorber layers in solar cell application.

Figure 1.5 (a) shows the ternary phase diagram with possible phases in the Cu-In-Se system. The pseudo-binary In_2Se_3-Cu_2Se equilibrium phase diagram, which is derived from the Cu-In-Se ternary system, is shown in Figure 1.5 (b). In the phase diagram, α is the chalcopyrite $CuInSe_2$ phase, δ is a high-temperature phase and β is an ordered defect compound phase (ODC). The α phase is the most important phase in the Cu-In-Se system for high efficient CIGS solar cell. It can be clearly seen that the single phase field for $CuInSe_2$ at low temperature is narrower than at higher temperature, and becomes maximum around 600^0C. So the best suited growth temperature for CIGS thin film is around 600^0C. The average copper (Cu) compositions of high quality CIGS films deposited at high temperature is 22-24 at%, which lie within the single phase region.

CIGS is formed by alloying $CuInSe_2$ in any proportion with $CuGaSe_2$. In high performance CIGS cell, the Ga/(In+Ga) and the Cu/(In+Ga) ratios are typically 0.2-0.3 and 0.7-1, respectively. There is the possibility of high defect density in Cu-poor films but these defect densities should be reasonably low and electronically inactive to avoid adverse effects on solar cells performance [20]. At the Cu-poor boundary, the α-phase coexists with the β-phase, which represents a number of ODC like $CuIn_3Se_5$, $CuIn_5Se_8$ etc. The addition of Ga or Na suppresses the formation of ordered defect compounds [20] and thus widens the α-phase towards the Cu poor boundary. Thus, these provide slightly more freedom in terms of deposition conditions.

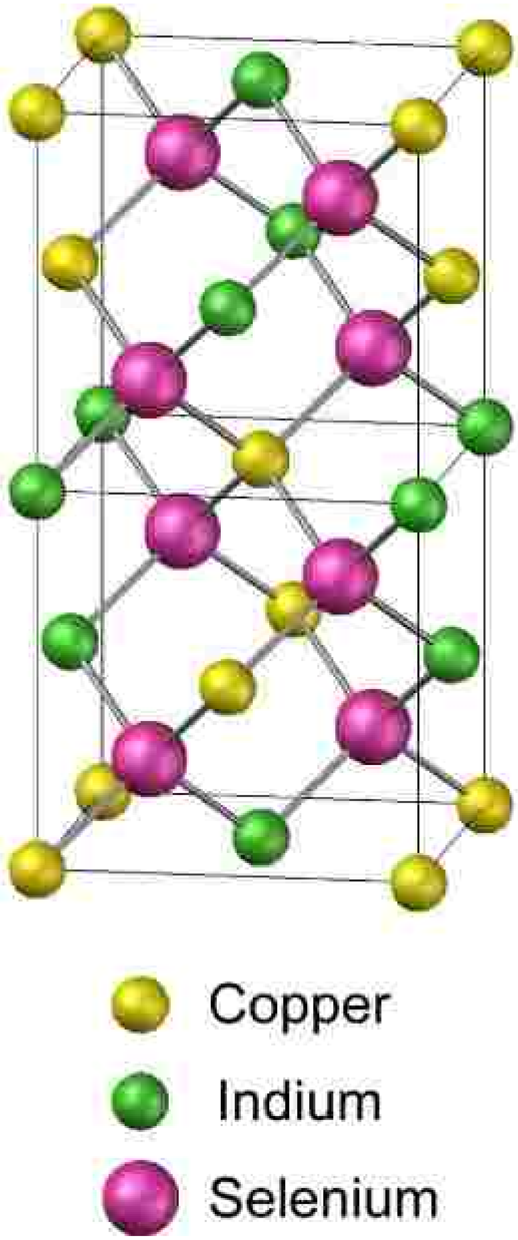

Figure 1.4: Chalcopyrite crystal structure of CIGS [21]

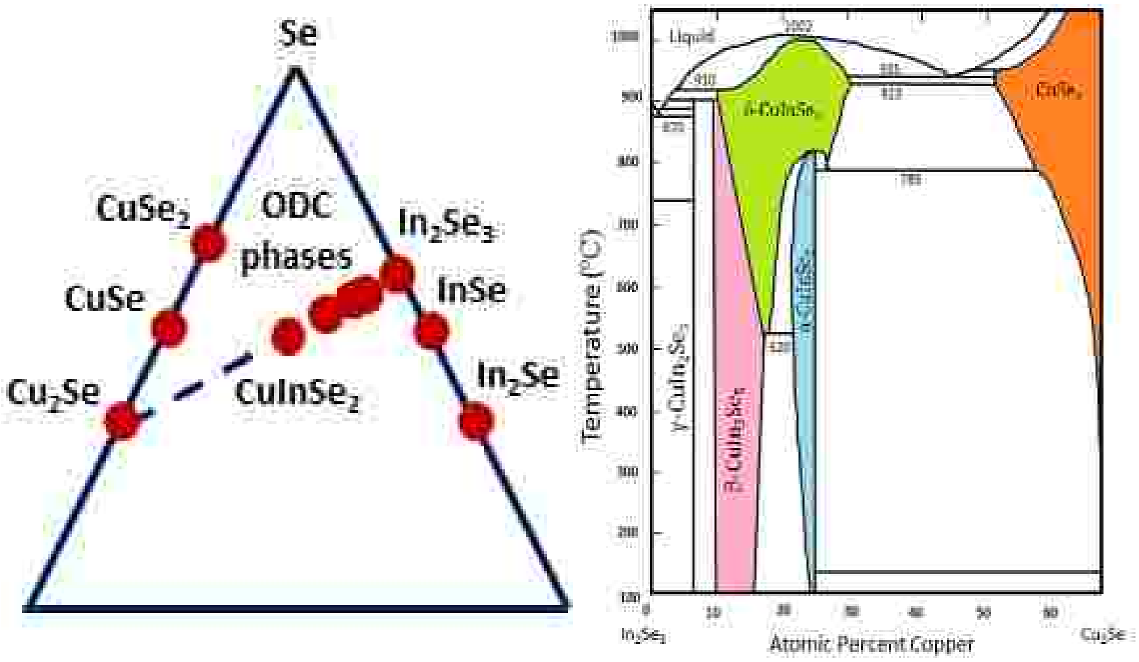

Figure 1.5: (a) Ternary phase diagram of Cu-In-Se system [17] and (b) pseudo-binary phase diagram [21].

1.4.2 Optical Properties and Band Gap Grading

CIGS films have very high absorption coefficient, with values larger than 10^5 cm^{-1} for 1.5 eV and higher energy photons [22]. So, only a few micrometer thick CIGS film is needed to absorb most of the incident light. The absorption coefficient, α, can be calculated from the transmission and reflection coefficients using the following expression [23]:

$$\alpha = \frac{2\ln(1-R)-\ln(T)}{d} \tag{1.1}$$

Where d is the thickness of the thin film, R is the reflection and T is the transmission. Since CIGS is a direct gap semiconductor, the absorption coefficient in the region of strong absorption obeys the following equation

$$\alpha = \frac{A}{h\upsilon}(h\upsilon - E_g)^{1/2} \tag{1.2}$$

Where h is the Planck constant, ν is the radiation frequency, E_g is the band gap energy and A is a constant, which depends on the nature of the radiation. The extrapolation of the linear portion of the $(\alpha h\nu)^2$ versus hν graph at hν = 0 gives therefore the band gap value of the material. Cu(In,Ga)Se_2 has a tunable band gap that varies with x = Ga/(In+Ga). The relation between the E_g and x can be expressed by the following empirical formula [24]:

$$E_g = (1-x)\,E_g(CIS) + xE_g(CGS) - bx(1-x) \tag{1.3}$$

where E_g(CIS) is 1.04 eV, the band gap of CuInSe_2 ; E_g(CGS) is 1.68 eV, the band gap of CuGaSe_2; and b is the bowing parameter that depends on the growth. The most reproducible values of b are around 0.15–0.24 eV [24]. The Ga content in the Cu(In,Ga)Se_2 thin film affects the band-gap primarily in the conduction band, therefore the band gap of Cu(In,Ga)Se_2 increases with increasing Ga content by shifting the conduction band position [24]. So, with an appropriate spatial variation of Ga in the Cu(In,Ga)Se_2, various band gap profiles can be achieved as shown in Figure 1.6. Introducing a higher Ga/(In+Ga) ratio near the front surface (Space charge region) and at the back surface region of Cu(In,Ga)Se_2 film will increase the band gap locally. The increase in the band gap, ΔE_g, creates an additional electric field, which is also called quasi electrical field [25]. The back surface recombination can be reduced significantly due to the back surface grading, which also enhances the voltage by reducing recombination. The SCR grading as an addition to the back surface grading also increases the device voltage since the voltage is also determined by the band gap in the space charge region. In general, a proper band-gap grading in the SCR and back surface are capable of significantly improving the device performance.

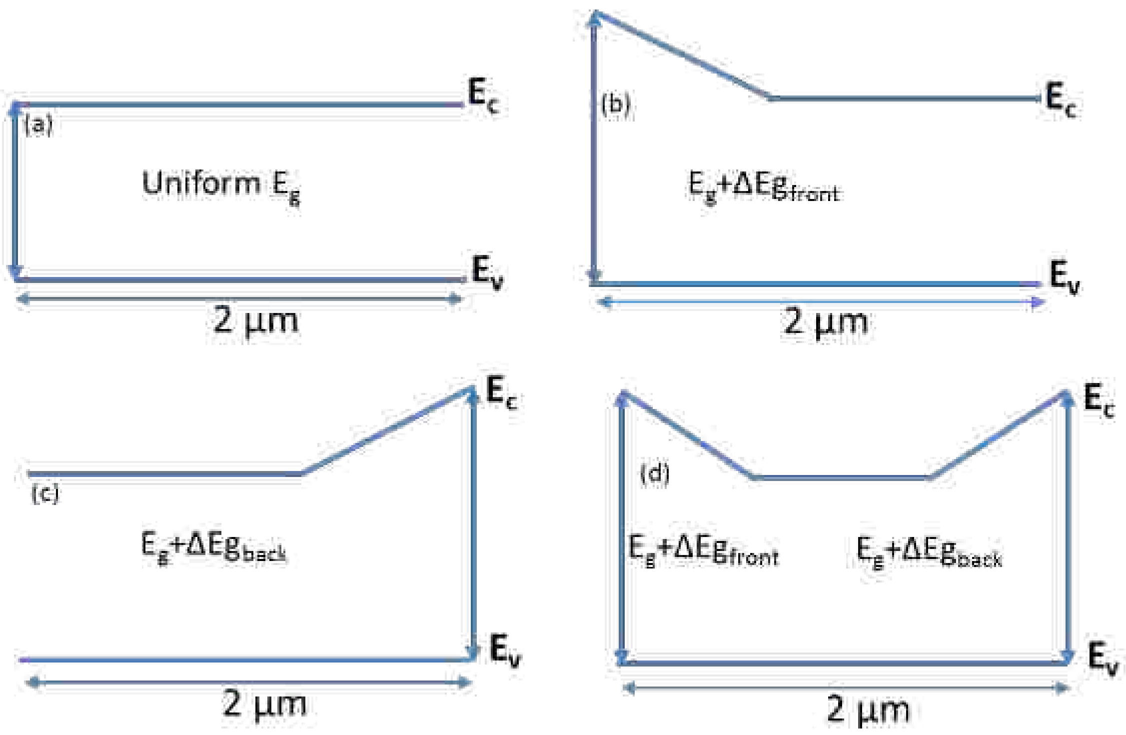

Figure 1.6: Different types of absorber band gap profiles. (a) Uniform band gap (b) Front grading (Space charge region grading) (c) back surface grading (d) Double grading.

1.5. CIGS Solar cells and deposition process

1.5.1 CIGS solar cell structure

CIGS cell structure consists of the following layers (Figure 1.7): n-ZnO:Al as a window layer, i-ZnO, CdS as a buffer layer, p-CIGS as an absorber, Mo as the metal contact and glass as the substrate. A molybdenum layer deposited by magnetron sputtering serves as the back contact and reflects some of the unabsorbed light back into the absorber. Following molybdenum deposition a p-type CIGS absorber layer is done by co-evaporation process. The co-evaporation process is the most successful technique used to fabricate high efficiency CIGS solar cell. This deposition process involves simultaneous evaporation of individual elements from multiple sources in a single or sequential process. A thin cadmium sulfide (CdS) deposited by chemical bath deposition (CBD) is added on top of the absorber. CdS thin films (~ 50 nm) deposited by CBD process yield the most efficient $Cu(In,Ga)Se_2$ thin film based devices since this process is conformal for very thin films. This process also helps in cleaning the CIGS layer and in intermixing the Cd by chemically driven ion-exchange mechanism [26]. However, there is a loss of current in the solar cell due to the absorption in the CdS layer at and below ~520 nm. So CdS thickness optimization is very crucial in CIGS solar cell. A thin, intrinsic zinc oxide layer (i-ZnO) and aluminum-doped zinc oxide (AZO) are deposited on top of the CdS. The i-ZnO layer is used to protect the CdS and the absorber layer from sputtering damage while depositing the ZnO:Al window layer. The AZO serves as a transparent conducting oxide to collect and move electrons out of the cell. It is therefore crucial to optimize each layer of the CIGS solar cell structure to produce the best performance CIGS solar cells. The detail process for each layer is described below.

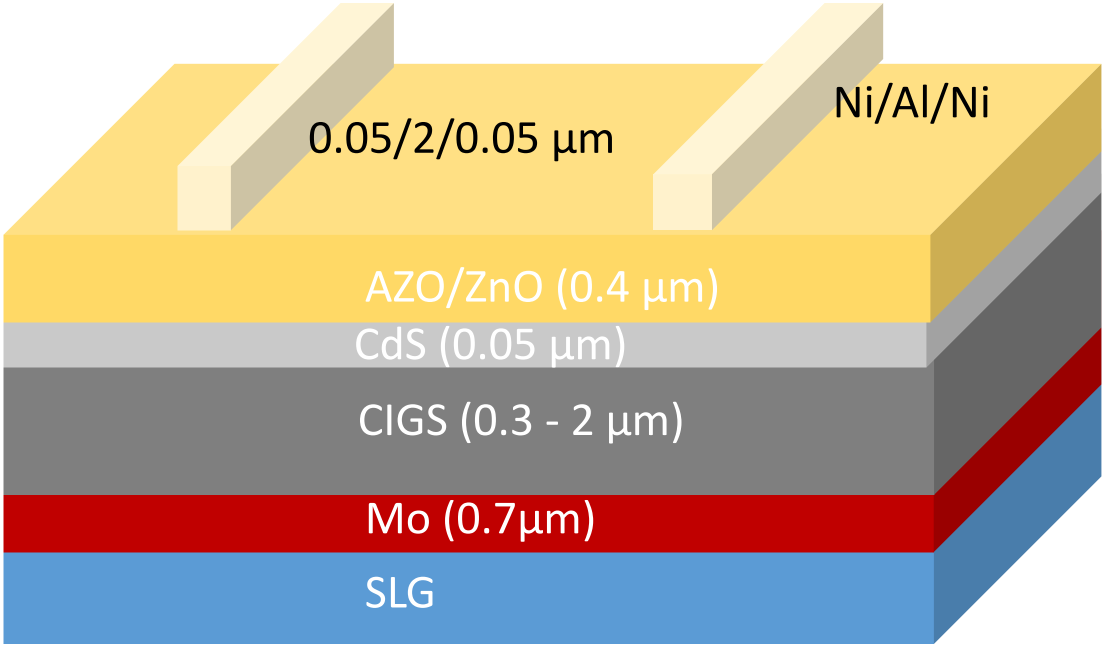

Figure 1.7: CIGS solar cell structure.

1.5.2 Molybdenum Back Contact Deposition

Molybdenum back contacts were deposited on soda lime glass (SLG) by DC magnetron sputtering with base pressure of ~ 2 x 10^{-6} Torr. Molybdenum targets with 2 inches diameter, ¼ inch thickness, and 99.95% purity were used. Uniform film thickness (±5% error) was achieved using a rotatable substrate holder. The argon pressure was varied between 3 and 16 mTorr while keeping a constant sputtering power of 150 W. The resistivity of the films was found to increase with increasing working pressure (Figure 1.8). At higher working pressure in the system, the kinetic energy of Mo ions is decreased due to the increased particle scattering. The deposited film tends then to be less dense with some porous column boundaries, and cannot be crystallized well. As a result, the resistivity of the film increases. The sputtering DC power was also optimized and it was found that the resistivity of Mo film was inversely proportional to the sputtering power. So, the pressure and power during the deposition was kept at optimized value to obtain the better quality back contact Mo layer. However, in order to obtain an optimal Mo film, with a lower resistivity and good adhesion, a new process was needed and the Mo layer film was deposited using a sequentially changing working pressure. We observed, as had been previously reported [krishnathesis], that films deposited at high pressure lead to high resistivity while films deposited at low pressure leadto poor adhesion. In order to ensure optimum properties for the Mo bilayer, the 1st layer was deposited at 10 mTorr (with a thickness ~250 nm), and the 2nd layer was deposited at 3 mTorr (with a thickness ~500 nm), which ensures good adhesion, low resistivity, and high reflectance. The power used was 150 W. The thickness for all depositions was kept constant at ~ 0.75 μm. Adhesive tape test was performed on each film by using scotch tape to determine the adhesion strength of the films.

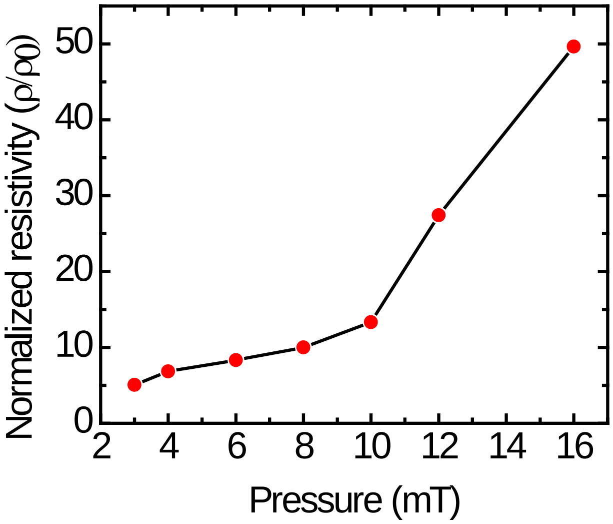

Figure 1.8: Normalized resistivity as a function of pressure for Mo thin film.

1.5.3 CdS Buffer Layer Deposition

Cadmium sulfide (CdS) was deposited by chemical bath deposition (CBD) process as a buffer layer and heterojunction partner for CIGS. The chemical used in the CBD process consists of Cadmium Acetate ($Cd(CH_3COO)_2$) as a Cadmium source, thiourea ($CS(NH_2)_2$) as a Sulphur source, and Ammonium Hydroxide (NH_4OH) as a complexing agent. The deposition process consists of an external bath with a heater attached to it. Different recipes were implemented to optimize the CdS layer to achieve the best performance CIGS solar cells.

In the first recipe, 22 ml of 7.63 g/l aqueous solution of Cadmium Acetate was mixed with 17 ml of NH_4OH (30%); then, 22 ml of 77.85 g/l of aqueous solution of Thiourea was poured into the beaker containing 164 ml of water. The sample, which was first soaked in DI water for 5 minutes, was immerged into the water bath heated at 60^oC. Every minute, the samples were shaken up and down few times which help remove any precipitates on the surface. The pH of the solution was typically around 11. The deposition was continued for 9 minutes. After the deposition, samples were rinsed with DI water and dried in a nitrogen environment.

In the second recipe, 15 ml of 6.74 g/l aqueous solution of Cadmium Acetate and 35 ml of NH_4OH (28%) were first mixed into a beaker containing 185 ml of DI water. The beaker was then placed into the water bath. After 1 minute, 15 ml of 28.48 g/l aqueous solution of Thiourea was poured into the beaker. The deposition was started when the water bath was heated at 70°C. The sample was then dipped into the solution and the deposition was completed in 22 minutes. Every 2 minutes, the samples were shaken up and down few times which helped remove any precipitates on the surface. After the deposition, samples are rinsed with DI water and dried in a nitrogen environment. The thickness of the CdS layer for both process was around 50 nm.

Extra precautions on the chemical purity and process were taken while performing CBD process to reduce the extra contamination in the films. For each CBD process, a fresh solution was prepared for individual chemical sources which enhanced the fabrication process.

1.5.4 Window Layer Deposition

The window layer in the CIGS solar cell structure contains two parts: a 100 nm thick intrinsic ZnO and a 350 nm thick 2% aluminum-doped ZnO. Both films were deposited by RF magnetron sputtering at 13.56 MHz with a base pressure of ~5 x 10^{-6} Torr. The power used for the deposition of i-ZnO and Al:ZnO targets were 60 W and 130 W, respectively. The substrate temperature was kept at room temperature, while the pressure was kept constant at 4 mTorr. Uniformity of the film thickness was achieved by using a rotatable substrate holder moving at a speed of ~20 rpm. Sputtering from the AZO target in low humidity condition (called dry environment) allows the layer transparency to be kept at a high level (85-90%) with a low sheet resistance of 30-35 Ω/sq.

1.5.5 Metal Contact Deposition

After the deposition of the window layers, metal grids were deposited on top of the AZO layer to facilitate the current collection and provide a contact pad for J–V characterization of the cells. The tapered finger grids in a 100/3000/50 nm thick Ni/Al/Ni sandwich were deposited by e-beam evaporation through a shadow mask and covered approximately 4% of the total cell area. The metal evaporation rate and film thickness were monitored with a quartz-crystal microbalance (QCM). The function of the two thin nickel layers is to protect the aluminum to react with oxygen from the front contact layer and from air, respectively. The top nickel layer also facilitates an Ohmic contact between the grid and the I-V measuring probes. Figure 1.9 shows the CIGS complete cells with area 0.5 cm^2 defined by mechanical scribing.

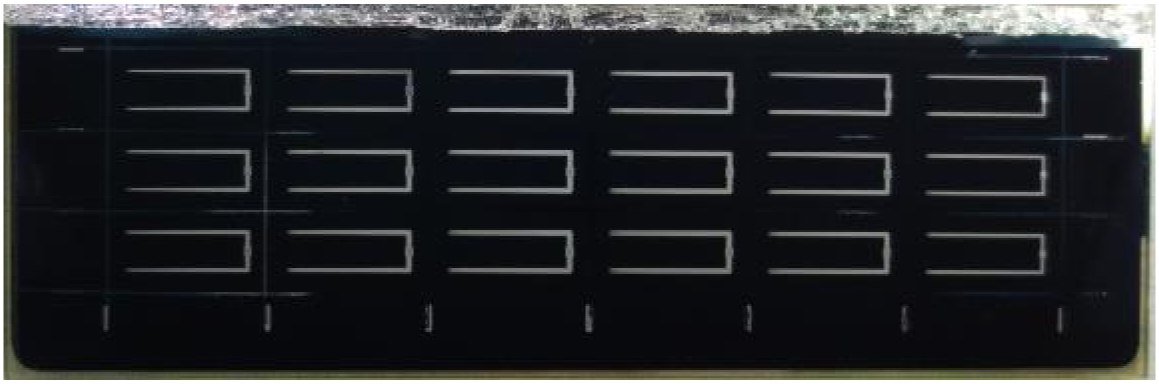

Figure 1.9: CIGS complete cells with area 0.5 cm^2 defined my mechanical scribing.

1.6 Thesis Objectives and Organization

A variety of technology options exist at present to harvest the power of the sun, a sustainable energy source, and generate electricity directly from this source via the photovoltaic effect. Among them, $Cu(In,Ga)Se_2$ has gained significant momentum as a possible high efficiency and low cost thin film solar cell material. With 22.6% efficiency, $Cu(In,Ga)Se_2$ (CIGS) solar cells are the most efficient polycrystalline thin film solar cells today. The capacity to scale up any photovoltaic technology is one of the criteria that will determine its long-term viability. For high efficiency devices, transport of the photogenerated carriers through the entire solar cell stack is just as important as their generation, guaranteed by the device quality $Cu(In,Ga)Se_2$. To achieve this goal, it is essential to optimize the back contact layer properties in the solar cell stack. The best performance so far is obtained when molybdenum is used as a back contact. It satisfies the most requirements for an effective back contact, particularly chemical and mechanical compatibility with the other deposition processes, high conductivity, low contact resistance with the CIGS layer, and matching thermal expansion coefficient. The deposition process and parameters play a vital role in attaining a layer with suitable properties. The main objective of this work is to understand the influence of substrates, substrate heating and deposition process conditions on impurities diffusion, and on the characteristics of the molybdenum films.

In Chapter 2, the materials properties of the molybdenum films and the characterization techniques used to explore the molybdenum films and devices are studied.

In Chapter 3, the study of molybdenum films on different substrates along with *in-situ* and *ex-situ* ellipsometry analysis are discussed.

In Chapter 4, the effect of substrate temperature on sputtered molybdenum films are presented. Chapter 4 also provides an overview of both a theoretical model used for simulating and understanding grain boundary diffusion mechanism for impurities through Mo films as a function of substrate temperature.

In Chapter 5, the effects of annealing on bilayer molybdenum films used as back contact are discussed. CIGS solar cells fabrication processes are also discussed in addition to the analysis of the devices fabricated on different back contacts.

Finally, Chapter 6 provides a summary of the work presented here and the general conclusions drawn from it. In addition, a discussion of the future work of this line of research will be presented.

CHAPTER 2

$Cu(In,Ga)Se_2$ SOLAR CELL: BACK CONTACT MATERIAL PROPERTIES AND CHARACTERIZATION METHODS

2.1 Molybdenum Material Properties

Molybdenum (Mo) is currently the most common material used for $Cu(In,Ga)Se_2$ solar cell back contacts. Several properties are required to fulfill this role, including chemical and mechanical inertness during the other deposition processes, high conductivity, low contact resistance with the $Cu(In,Ga)Se_2$ layer, and a commensurate thermal expansion coefficient with contact layers [17]. A wide variety of materials, such as W, Ta, Nb, Cr, V, Mo, Ti and Mn have been investigated as possible back contacts in the $Cu(In,Ga)Se_2$ solar cell. The results showed that Mo is the best, and the other materials result in lower cell efficiency due notably to their chemical reactivity [17]. Films were deposited by e–beam evaporation onto soda lime glass (SLG) substrates. The authors concluded that devices with Ta and Nb back contacts showed good performance only for the graded band gap of the absorber, whereas Cr, V, Ti and Mn tend to react with selenium during the deposition of the $Cu(In,Ga)Se_2$ layer. In addition, comparable device performances were demonstrated for the W and Mo with or without the band gap grading of the $Cu(In,Ga)Se_2$ layer, while the Ta resulted in delamination with the substrates.

Mo back contact is usually deposited by DC magnetron sputtering. It has been demonstrated that the internal stresses in refractory-metal films prepared by magnetron sputtering deposition are greatly dependent on the working gas pressure [18, 19]. Being a refractory-metal, Mo deposited by DC magnetron sputtering demonstrates a correlation between working gas pressure and residual stress [17, 18, 19]. Macroscopic stresses may be detected by visual evaluation. Films with highly compressive stress tend to buckle up, whereas films under substantial tensile stress display scratch patterns [20, 21]. At lower pressures, the mean free path of the energetic particles is longer, thus the bombarding atoms possess higher kinetic energy. As a result, the deposited film exhibits a densely packed microstructure, which is the reason for the inclination towards the compressive stress state. However, at higher pressures, the mean free path is shorter and particles show higher probability to be scattered, thus less energetic particles are incident on the film. As a consequence, the film tends to show an open porous microstructure. Because of its open structure, interatomic or intergranular attractive forces become high, therefore producing tensile stress. Open structure increases the resistivity of Mo thin films. Hence, resistivity is strongly related to the working gas pressure condition.

It has been demonstrated that the surface roughness of the substrate may impact the device performance for the CIGS solar cell following three mechanisms [27]:

(a) Nucleation: A rough Mo film is supposed to provide more sites to nucleate for CIGS absorber, which results in smaller CIGS grains and more defects.

(b) Impurity diffusion: Different impurities diffuse through the Mo back contact from the soda lime glass substrate into the CIGS layer during the growth process of the CIGS absorber layer at higher temperature. Na is a common element to diffuse fast and is a useful impurity for CIGS solar cells; but the amount of Na incorporation has to be controlled for repetitive reliable CIGS solar cell production. Defects and grain boundaries in Mo layers offer fast diffusion paths for all impurities. Consequently, it is essential to regulate the impurity diffusion by controlling the microstructure of the Mo back contact layers.

(c) Metallurgical shunt: Large surface projections of Mo layer could bulge through the CIGS absorber layer creating shunt paths.

Electrical and mechanical properties of direct current (DC) sputtered Mo thin films on SLG have been investigated at various sputtering pressures [18]. Films prepared below 2.0 mTorr of argon pressure have shown good electrical properties. However, these films showed delamination. In contrast, films prepared at relatively high pressures (above 10.0 mTorr) exhibit poor electrical properties without any delamination. The trade–off between film resistivity and film–substrate delamination as a function of argon pressure was resolved by using a bi–layer deposition process. This process consists of a thin layer deposition of ~200 nm at high argon pressure (e.g.: 10.0 mTorr), followed by thicker film deposition (~800 nm) at low sputtering pressure (e.g.: 3.0 mTorr). The first layer maintains good adhesion to the substrate, while the second layer preserves excellent electrical properties. This bi–layer Mo back contact is widely used for high efficiency Cu(In,Ga)Se_2 solar cells. Thin film Mo back contacts used in Cu(In,Ga)Se_2 solar cells play also a key role in enabling the diffusion of Na atoms from the underlying SLG substrate into the overlying Cu(In,Ga)Se_2 layer, where the Na is considered to improve the electronic properties of the Cu(In,Ga)Se_2 [19, 20] for instance the formation of larger grains [28], preferential orientation of grains [29], increased p-type conductivity [30], and the inhibition of In/Ga interdiffusion [31]. Na can be incorporated via external source using a wide variety of techniques other than relying on Na from the SLG. The use of NaF is more common since it is less hygroscopic and easier in handling than other sodium compounds. An external Na source permits the use of Na-free substrates, for example flexible metal foils. If SLG is used together with an external Na source, an alkali diffusion barrier for instance Al_2O_3 or SiO_2 is often deposited on SLG [32, 33] as very large amounts of Na can be disadvantageous to device performance, as shown in Figure 2.1 [34]. Na compounds can be incorporated before [35], during [36], or after CIGS depositions [37], and all processes exhibited similar increases in efficiency.

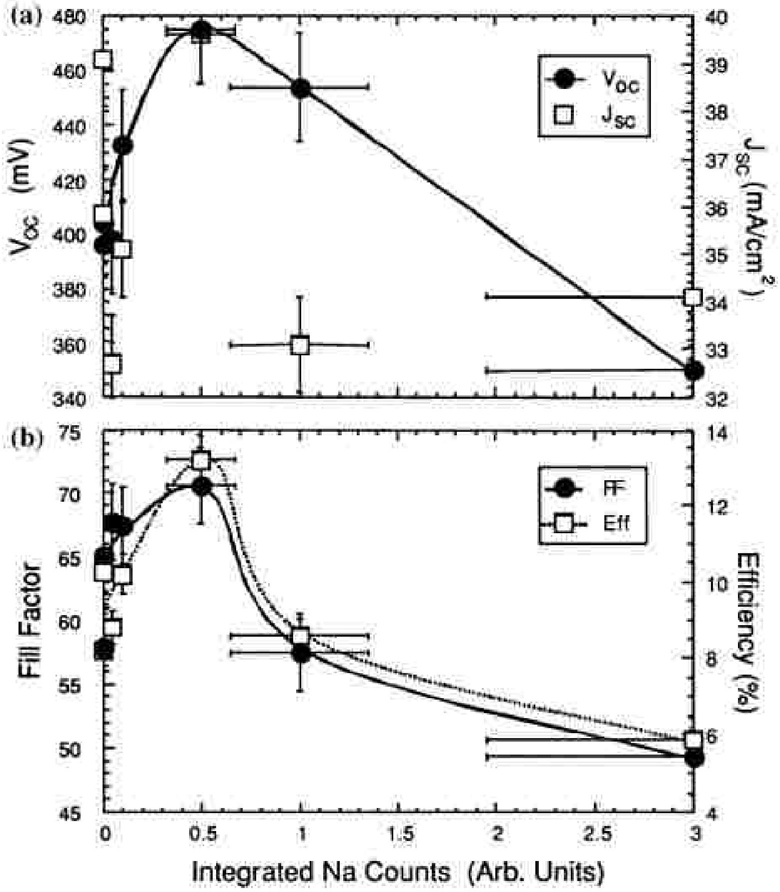

Figure 2.1: Solar cell performance variables as a function of Na content as measured in the device layers by SIMS [34].

The Na out-diffusion from the SLG into the Cu(In,Ga)Se_2 layer has been studied as a function of Mo deposition conditions [21]. These authors have demonstrated that the lower the sputtering pressure, the lower the concentration of Na in the $Cu(In,Ga)Se_2$ layer. Effectively, thin films of Mo prepared at low sputtering pressure formed densely packed grain structures, which prevent the migration of Na to the $Cu(In,Ga)Se_2$ layer, since the Na diffuses along the grain boundaries of the Mo film.

The high temperatures (usually greater than 450°C) during CIGS deposition cause Na diffusion through the Mo and into the CIGS layer. The amount of Na supplied using this method is not well controlled and as a result non-uniform distribution of Na over large areas can be observed [17, 18]. Nevertheless, it remains a suitable option due to its straightforwardness and low price. A better understanding of the Na diffusion mechanism through Mo might potentially direct to solutions for overcoming these controllability issues. Recent studies show that at CIGS deposition temperatures, which range from 450°C to 600°C, Na is highly mobile through Mo grain boundaries [19] but might not diffuse into the grain as the solubility of Na is insignificant up to at least 2623°C [20], which is the melting point of Mo. As a result, it is improbable that any bulk transport might occur through Mo grains. As grains in a usual Mo back contact are columnar in structure and span the entire height of the film [21], the grain boundaries offer a fast diffusion path to the CIGS interface. Na tends to segregate near the Mo/CIGS interface, which has been reported by different groups using secondary ion mass spectroscopy (SIMS) [22, 23]. The amount of Na accumulation at the Mo surface may define the amount of Na incorporation into the remaining CIGS film [20]. Extensive research has been done on the deposition of Mo thin films by DC and RF sputtering [17, 18, 21, 22, 23]. However, as the potential portfolio applications of $Cu(In,Ga)Se_2$ expand, different film properties may be required to adapt to new necessities. Therefore, in this work, we introduced substrate heating during the deposition of molybdenum films on different substrates. To our knowledge, little research has been performed on Mo thin films deposited by this method [24, 25, 26, 27, 28, 29]. To assess the potential of this process, the physical and electrical properties of Mo thin films were studied as a function of substrate temperature and type of substrates.

2.2 Materials and Devices Characterization

Molybdenum thin films were analyzed *in-situ*, in real time or *ex-situ* via different types of characterization techniques. The outcomes from these techniques were then verified to get a complete understanding of the materials and devices properties.

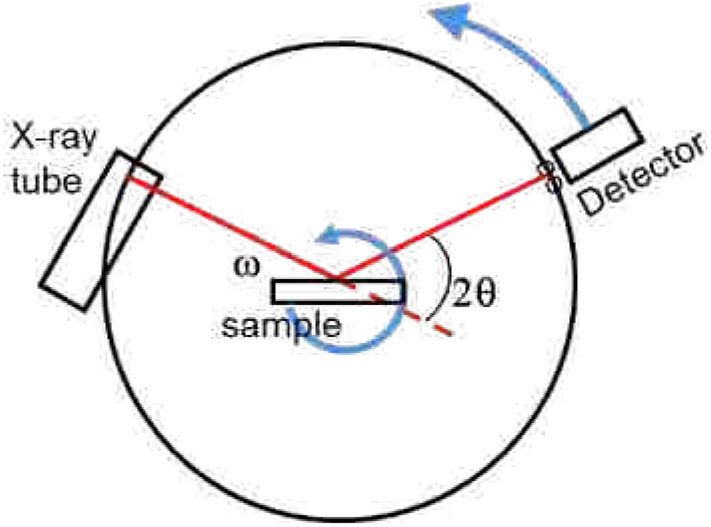

Figure 2.2: Block diagram for X-ray Diffraction.

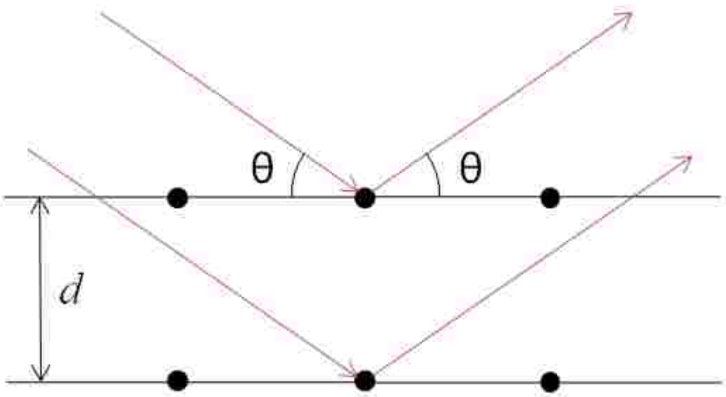

Figure 2.3: Demonstration of Bragg's law.

2.2.1 X-ray Diffraction (XRD)

X-ray diffraction is a fast analytical technique used to probe if crystalline phases exist in materials and to extract the structural properties such as grain size, preferred orientation and defect structure of the phases. When a collimated beam of X-rays is impinging on the sample surface, X-rays are diffracted at different angles based on the crystal structure of the sample (Figure 2.2). The diffraction spectrum of the samples is plotted as a function of 2θ. Diffraction peaks appear, when Bragg's law (2d sinθ = nλ) is fulfilled (Figure 2.3). The diffraction angle, the number of peaks and their intensity depend on the crystal structure, symmetry, and lattice constant. After comparing the peaks with XRD database, the phase, crystal orientation, lattice constants, and other information are extracted. The inter-planar spacing, d_{hkl}, which correspond to each diffraction line, is calculated using the following equation:

$$d_{hlk} = \frac{\lambda}{2Sin\theta} \tag{2.1}$$

where θ is Bragg's angle of diffraction and λ is the wavelength of the X-rays radiation. XRD data can also be used to calculate the crystallites size using Scherrer formula [17].

$$L = \frac{K_s \lambda}{\beta \cos \theta} \tag{2.2}$$

where L is the grain size, K_s is Scherrer constant (typically set at 0.9 for spherical particles), β is the full width at half maximum of the peak in radians, λ is the wavelength of the X-ray beam and 2θ is defined as the peak position.

The X-ray's penetration depth can be varied by changing the angle of incidence of the x-ray's beam. With a larger angle it is possible to observe the material composition deeper into the sample. At times, it is not preferred to probe deeply into the film or not possible to obtain a strong signal if the film is too thin. In such cases, grazing incident XRD (GIXRD) can be used. This is fundamentally a low angle XRD, which varies the penetration depth of the X-ray by setting the incident angle from 1 to 10 degrees while moving the detecting arm.

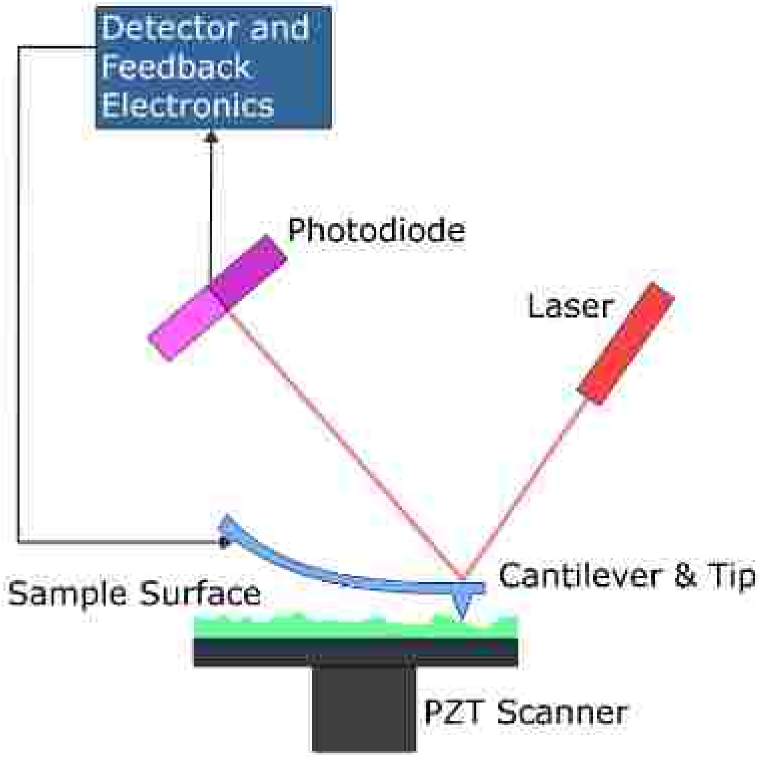

Figure 2.4: Block diagram for an Atomic Force Microscope.

2.2.2 Atomic Force Microscopy (AFM)

AFM is a type of scanning probe microscope, which is used to get surface structure images (in nm or even sub-nm scale) and other information. In AFM, a probe is kept in close proximity with the sample surface using a feedback mechanism as it scans across the surface, and the movement of the probe to stay at the same probe-sample distance is converted into the sample topography (Figure 2.4). In general, a cantilever made of Si or SiN is used to examine the surface of the sample by adjusting the position via control mechanism. The tip of the cantilever is maintained in continuous or intermittent contact with the sample surface and the cantilever is moved over the sample using a piezo-controller. A laser is reflected on the back surface of the cantilever as a scan progresses.

Whenever the laser changes its positions because of the force on the cantilever, a voltage is applied to the piezoelectric, which makes the laser to go back to its origin. This voltage relates to the height of surface topologies, since the force on the cantilever is created by the features on the specimen. An accurate calibration between the height and the voltage is achieved using a sample with known structure. AFM can be performed primarily in three different modes of imaging based on the surface to tip interaction. In contact mode, the tip of the AFM probe is continuously maintained in contact with the surface while in non-contact mode of measurement, the tip never touches the sample. During contact with the sample, the probe primarily experiences repulsive Van der Waals forces. For non-contact mode of operation, attractive Van der Waals forces are dominant as the tip moves further away from the surface. Contact mode AFM is reasonable for rough samples however it damages soft surfaces whereas the non-contact mode has poor resolution and generally requires ultra-high vacuum (UHV) to produce high quality images. In tapping mode, the imaging process is similar to that of the contact mode however in this mode, the cantilever is oscillated at its resonant frequency via the piezoelectric crystal, which is attached to the tip holder. During the oscillation, the probe tip keeps translating towards the surface until it taps on the surface lightly. As soon as there is a contact between the tip and the surface, a loss in the oscillation amplitude occurs, which is used to obtain the structural changes. This technique permits high resolution and is better for soft surfaces.

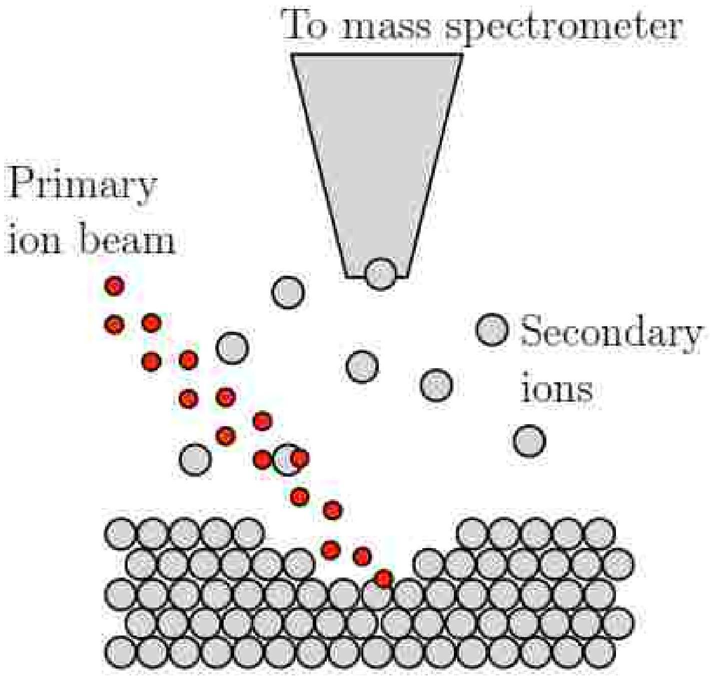

Figure 2.5: Illustration of the SIMS process.

2.2.3 Secondary Ion Mass Spectrometry (SIMS)

Secondary ion mass spectrometry (SIMS) is a highly sensitive surface analysis method used to obtain surface composition, elemental impurities and depth profile on the uppermost surface layers of a sample. SIMS employs a primary ion beam, for example an Ar or Cs ion, and directs it on the surface of the sample. Ions emitted from the material of the sample are defined as secondary ions (Figure 2.5). These secondary ions are then characterized by a mass/charge analyzer using their atomic mass values. Depending upon the polarity of the sample, positive or negative secondary ions will be extracted. SIMS analysis is sensitive enough to measure atoms in the ppm or ppb range and capable of monolayer analysis as well. The type of mass spectrometer employed in SIMS analysis relies on the mode of operation. Static and dynamic SIMS are used in the field of surface analysis. Static SIMS is capable of analyzing the surface in monolayer scale using a pulsed ion beam and a time of flight mass spectrometer, while the dynamic mode sputters the material off of the sample using a DC primary ion beam and measuring with a quadruple or magnetic sector mass spectrometer. In this study, a dynamic SIMS analysis was used to find the impurities in the molybdenum layer.

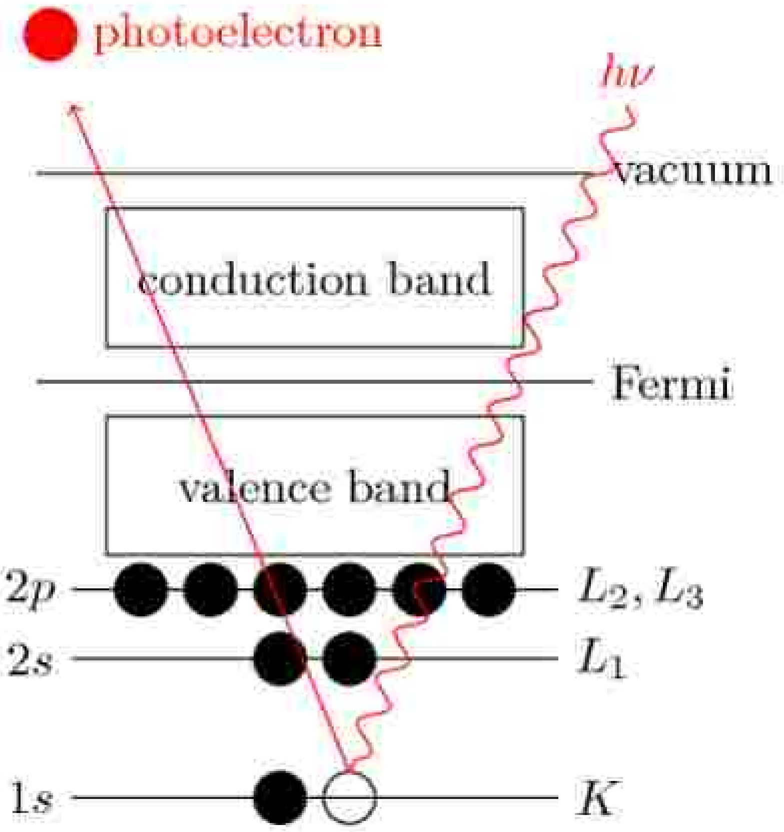

Figure 2.6: Illustration of photoelectron process in XPS analysis.

2.2.4 X-ray Photoelectron Spectroscopy (XPS)

X-ray photoelectron spectroscopy (XPS) is a quantitative spectroscopic technique for surface analysis that obtains the elemental composition at the parts per thousand range, and the chemical and electronic state of the elements present in a material. In XPS, incident

X-rays on the sample causes core-level electrons to eject as photoelectrons (Figure 2.6). The kinetic energy of the emitted photoelectrons is measured by the analyzer and the core-level binding energies is calculated according to the following equation:

$$BE = h\upsilon - KE - \varphi \tag{2.3}$$

where BE is the electron binding energy, $h\upsilon$ is the X-ray source energy, KE is the photoelectron kinetic energy, and φ is the spectrometer work function. The inelastic mean free path of a photoelectron is mostly determined by its kinetic energy and is usually 1nm to 2nm, which make XPS a very surface sensitive technique. The binding energies of the different core-level orbitals are distinctive for each element permitting easy identification and relative quantification of surface elements. In general, XPS requires high vacuum (~ 10^{-6} mTorr) or ultra-high vacuum (< 10^{-8} mTorr) conditions. XPS can be used to analyze the surface chemistry of a material in its as-received state, or after some treatment, for example: ion beam etching to clean off some or all of the surface contamination (with mild ion etching) or to intentionally expose deeper layers of the sample (with more extensive ion etching) in depth-profiling XPS, exposure to heat to study the changes due to heating. In this study, Al x-ray was used as the monochromatic source, and the detection system included small area extraction optics, spherical capacitor electron energy analyzer and dual channel plate position sensitive detector.

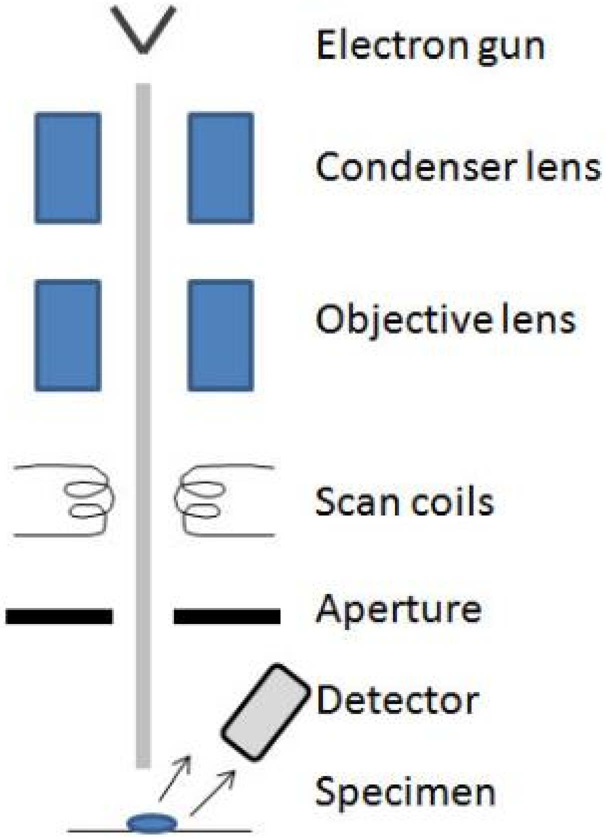

Figure 2.7: Illustration of Scanning Electron Microscopy.

2.2.5 Scanning Electron Microscopy (SEM)

Scanning electron microscopy uses a high-energy electron beam in a raster-scan pattern to create images with high magnification or gather other signals from the three-dimensional surface of a sample. An SEM comprises an electron gun, an electron lens condenser system, scanning coils, an aperture control, and electron detectors (Figure 2.7). In SEM, higher magnifications are possible compared to optical microscopes as electron wavelengths are much smaller than photon wavelengths and a large field of view is possible as the electron beam is small, which permits three-dimensional study of a specimen's surface. The focused electrons interact with the atoms in the specimen creating a number of different types of signals, which holds data about the specimen's surface morphology, composition, and other physical and chemical properties. The induced signals by an SEM comprise secondary electrons, back-scattered electrons (BSE), characteristic X-rays, photons as well as specimen current and transmitted electrons. Electrons with energies 0-30 eV are detected and utilized to produce the image in secondary electron mode. These electrons are ejected from within a few nanometers of the surface of the specimen. Backscattered electrons are electrons that are elastically scattered back from the sample and deliver the information about the bulk properties of the materials as this type of scattering occurs in a volume extending down to 0.5 µm below the surface of the specimen.

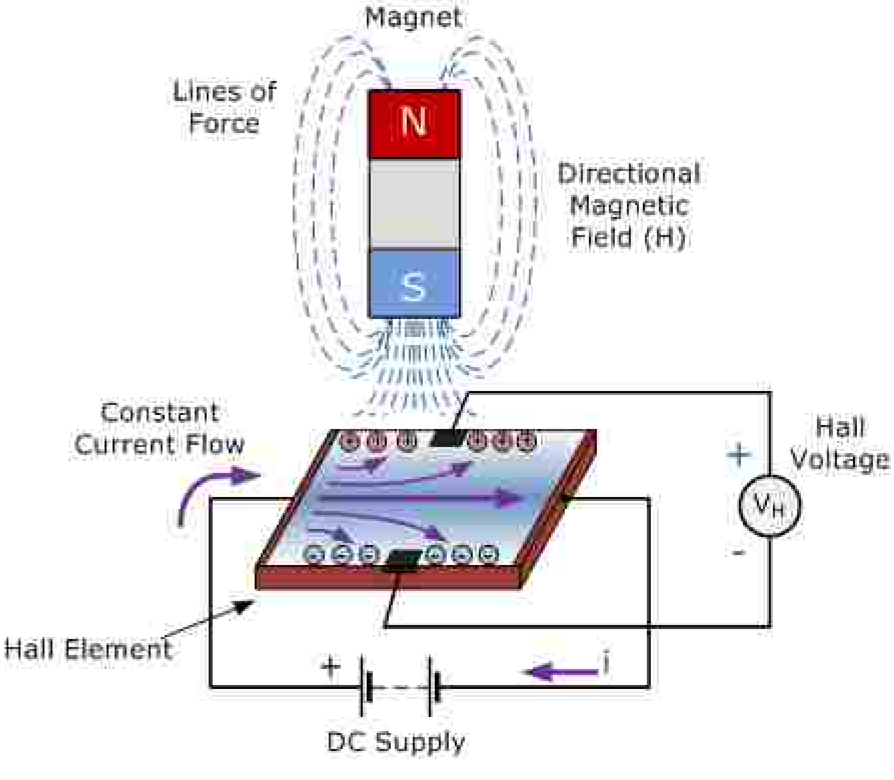

Figure 2.8: Illustration of Hall Effect measurement technique.

2.2.6 Hall Effect Measurement

A Hall Effect measurement system (Figure 2.8) is used to obtain electrical properties such as carrier concentration (n), carrier mobility (μ), resistivity (ρ), conductivity type (n or p), Hall voltage (V_H), Hall coefficient (R_H). When a current carrying conductor or semiconductor is placed in a magnetic field, a force perpendicular to both current and magnetic fields, known as the Lorentz force, is experienced by the charge carrier. This force is used to determine the magnitude and sign (n-type or p-type) of this force. When a magnetic field with a perpendicular component is applied, the paths of the charge carriers are bent so that moving charges accumulate on one side of the material. Equal and opposite charges stay on the opposite side of the material and a voltage can be acquired from the difference in charge density at equilibrium. During the measurement, a sample is mounted in the van der Pauw configuration where electrodes are connected (which are usually soldered for a good ohmic contact) at four opposite corners. In this configuration the sheet resistance can be obtained, and with an applied magnetic field, the charge carrier density and sign can be found as well.

2.2.7 Spectroscopic Ellipsometry Measurement

Spectroscopic Ellipsometry is an optical tool that utilizes polarized light for the study of the dielectric properties of specimens, from which more indirect parameters such as growth or structural parameters can be extracted. It measures a variation in polarization as light reflects from or transmits through the sample. Since it uses the polarization state for examination rather than only the intensity of the photon itself, it is a very sensitive measurement technique. It regularly generates information about layers that are thinner than the wavelength of the probing light itself and in theory down to a single atomic layer. The theory of the Ellipsometry is described in detail in Chapter 3.

2.2.8 Current Density vs. Voltage

The standard J-V measurement is carried out under a standardized “1-sun” (AM 1.5) illumination condition at room temperature. The solar cell is positioned under the light source, minimizing the distance to the center of the light. Two electrical probes are connected with the p-type and n-type sides. Dark measurement is executed without a light source while the illuminated measurement is done with the light source on. The measured data are collected using a sensitive and accurate multimeter and transferred to a computer, where all the data is kept as current (I) and voltage (V) pairs. The current density (J) is calculated after knowing the area of illumination for the sample so that J-V data can be obtained. This J-V measurement data are used to find efficiency, fill factor (FF), short circuit current density (J_{sc}), open circuit voltage (V_{oc}) as well as shunt resistance, series resistance, and the voltage dependent current collection. The current density in a real solar cell is expressed with [27].

$$J = J_0 \exp\left[\frac{q}{AKT}(V - R_s J)\right] - J_0 + \frac{V - R_s J}{R_{sh}} - J_L \tag{2.4}$$

where A is the ideality factor, R_s is the series resistance and R_{sh} is the shunt resistance of the solar cell. An equivalent circuit of a solar cell with these parasitic resistances is depicted in Figure 2.9 below.

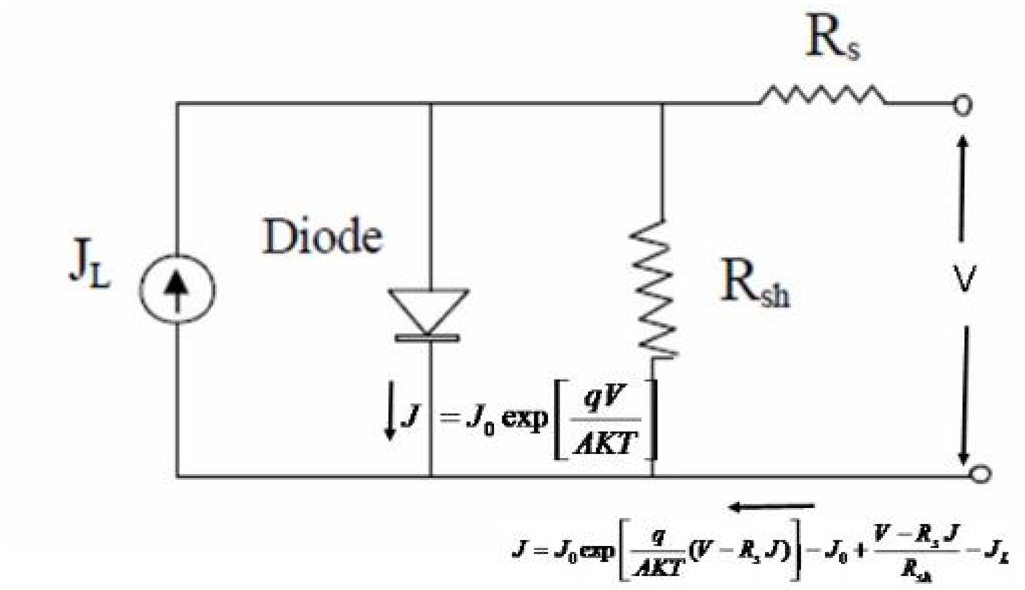

Figure 2.9: An equivalent circuit of a solar cell.

The series resistance R_s of a solar cell is due to both bulk resistance of the individual thin film of the cell stack, the resistance of the semiconductor-metal contacts, and the bulk resistance of the metal contact. The series resistance can be obtained from equation 2.4 by plotting $\frac{dV}{dJ} = R_s + \frac{AkT}{q}(J + J_L)^{-1}$ versus $(J + J_L)^{-1}$ under the condition where R_{sh} is infinitely high. This plot intercepts the y axis at a value of R_s and the slope of the linear region permits to identify A. The effect of increase in the R_s is revealed by the decrease in the steepness of the I-V curve as shown in Figure 2.11. I_{sc} and V_{oc} remain almost the same but FF decreases for a small increment in Rs. Nevertheless, large increase in Rs affects the I_{sc} first and then V_{oc}. The shunt resistance R_{sh} is infinitely high in an ideal case but this is untrue for the real solar cells. A solar cell in a non-ideal case always has a finite value of shunt resistance R_{sh} and this value may decrease additionally because of the leakage path near the junction as well as the existence of defects like pinhole in the absorber layer. The decrease in the R_{sh} has unfavorable effects on the fill factor. A plot of dJ/dV gives the shunt conductance, G = 1/R_{sh}.

Charged carriers can recombine before being swept across the junction by the build-in electric field, because of a short minority carrier lifetimes. Application of a reverse biased voltage across the terminal can increase the magnitude of the electric field, which permits the electrons with small diffusion length to be collected. Such an increment in the current because of bias voltage is defined as voltage-dependent current collection J_L (V). The presence of voltage-dependent currents can be seen as an increase in the slope in the reversed bias region of the J-V curve under illumination conditions. Such observation of the light J-V curve can be unclear since a decrease in R_{sh} can also affect the J-V curve in the same pattern. But the decrease in R_{sh} influences the dark J-V curve similar to the light J-V curve. So if there is a slope in the light J-V curve only, the voltage-dependent current collection can also be calculated from the J-V measurement.

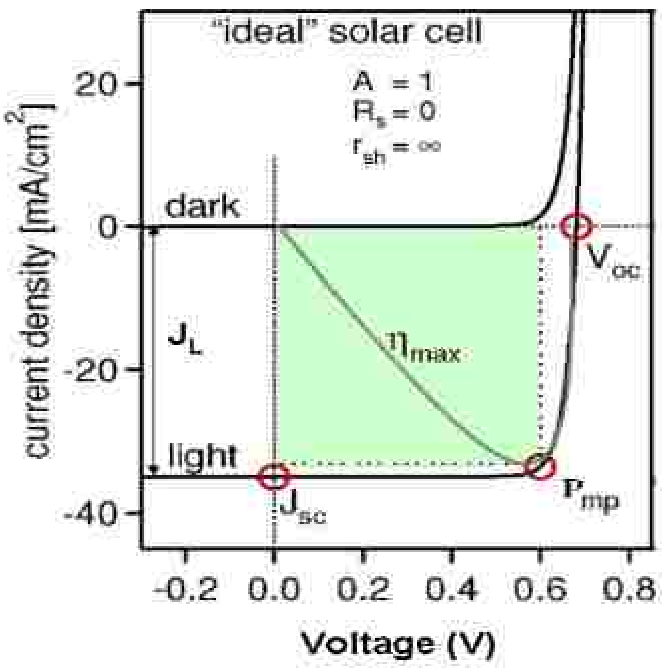

Figure 2.10: Light and dark J-V curves for an ideal and solar cell [28].

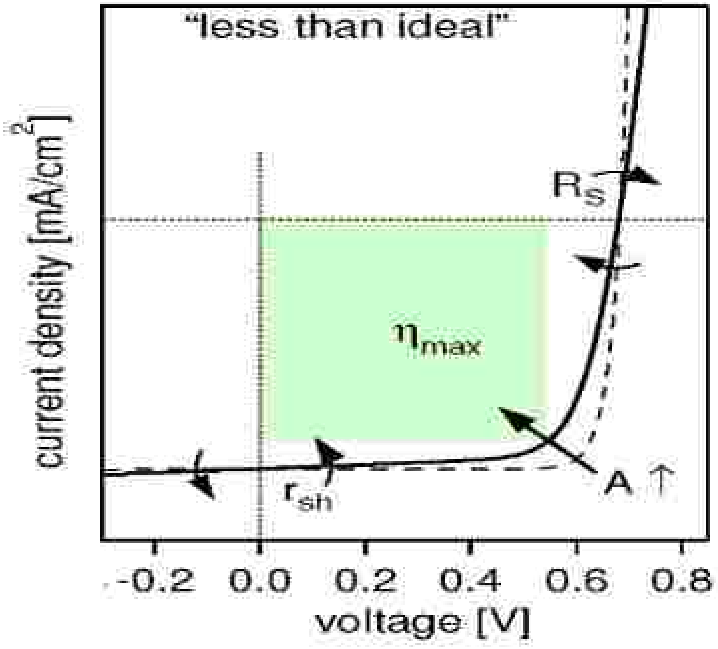

Figure 2.11: Light and dark J-V curves for a non-ideal and solar cell [28].

2.2.9 External Quantum Efficiency

External quantum efficiency (EQE) is described as the number of charge carriers generated by the solar cells per absorbed photon of a particular energy and is a way of measuring the fraction of incident photons that have been converted into electrons. When a photon reaches the surface of a solar cell, it can be absorbed by any of the layers in the solar cell stack. But photons with high energy tend to be absorbed near the surface of the cell facing the light source, while photons with lower energy tend to be absorbed in the bulk of a solar cell. In a solar cell structure, various layers are designed to absorb different energies of light, with the layers of the highest band gap near the surface of the cell exposed to the light. Therefore, each layer between the top and the bottom of the cell behaves as a window. A solar cell does not provide 100% QE, and the region of the QE spectrum with the lower current can offer insight to the layer in the solar cell responsible for a problem within the cell. As a result, QE of a real solar cell may have a value of less than a unity if either: i) the light is not absorbed or is reflected; ii) recombination takes place within the cell; or iii) there is a decrease in probability of collection due to the mechanism used for collection at a specific energy [29].

The total current density can be determined by integrating the product of the EQE and the photon flux density. For the standard AM1.5 G solar spectrum, short-circuit current density is calculated with the following equation [30]:

$$J_{SC} = q \int_0^{\infty} EQE(\lambda) \frac{\lambda}{hc} E_{\lambda}^{AM1.5G}(\lambda) d\lambda \tag{2.5}$$

where $E_\lambda^{AM1.5G}$ is the spectral irradiance of the AM1.5 G spectrum, λ is the wavelength, h is Planck's constant, and c is the speed of light.

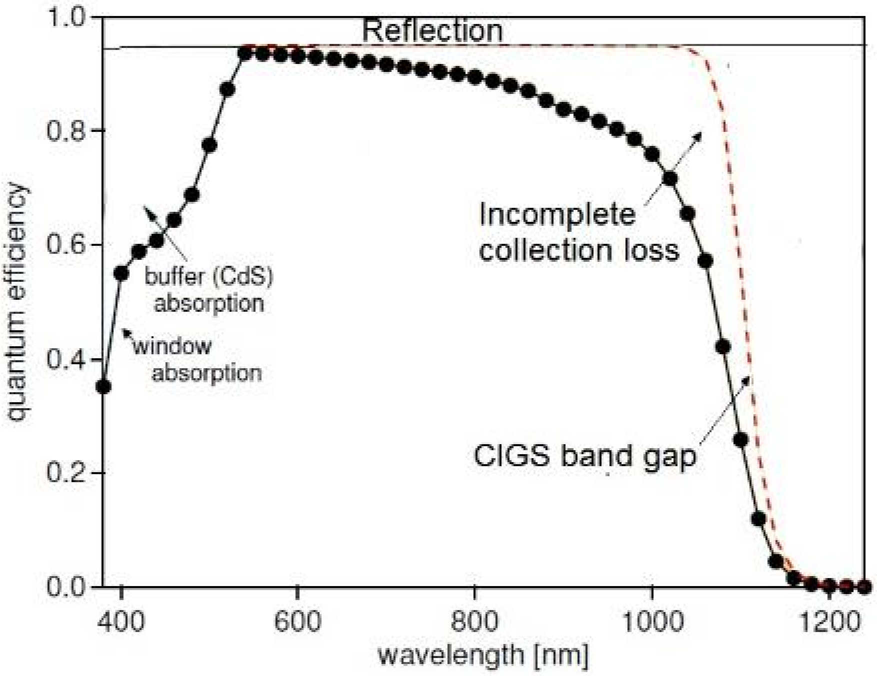

Figure 2.12: Typical CIGS quantum-efficiency curve and involved loss mechanisms.

The losses in the current are observed because of the optical properties of different layers in the cell also due to the defects in the absorber layer. Different losses in the QE are presented in Figure 2.12. The following are the losses seen in the solar cell:

(a) "Reflection" losses are seen because of the partial coverage of the front surface by the metal contact fingers or by reflection from the material interface. Such losses can be lowered down by depositing a thin anti-reflecting coating.

(b) "Window" absorption in the short-wavelength region is not substantial due to the high band-gap energy of ZnO/AZO. Free carrier absorption in the AZO layer can reduce the quantum efficiency in the high wavelength region. Such losses can be lowered by reducing the layer thickness. If the thicknesses of the window layers are lowered prominently there are chances of poor junction between CdS and CIGS, creating shunting path through i-ZnO layer and resulting in reduction of current collection due to an increase in sheet resistance in the Al:ZnO layer. Therefore, there must be a balance required to be maintained between the optical losses and the electrical losses.

(c) “Buffer” absorption is one of the main losses in thin-film solar cells (CIGS). Reducing the thickness of the CdS or substituting it with a higher band-gap material such as ZnS would be the potential options.

(d) “Recombination” losses occur because of the presence of traps or due to the low diffusion length in the absorber layer. The longer the wavelength, the deeper the generation of carriers and the higher the probability of the occurrence of recombination in the cell. This kind of loss can be observed by measuring the QE under negative biased condition.

(e) “Deep penetration” of carrier losses can take place for long wavelength photons as a result of incomplete absorption near the band gap of the absorber layer. These losses are inherent to most of the semiconductor because incident light with photon energy of $h\upsilon<E_g$ is not absorbed. This loss can be overcome by increasing the thickness of the absorber layer or making high quality absorbing materials.

2.2.10 Transmission and Reflection Measurements

The most common technique to determine the band gap of a semiconductor is by transmission and reflection measurement. The transmission and reflection coefficients of the semiconductors are usually measured in the wavelength range from 200-2500 nm. Then the absorption coefficient can be calculated from transmission and reflection coefficients using the following relation [aj]:

$$\alpha = \frac{2\ln(1-R) - \ln(T)}{d} \tag{2.6}$$

where α is the absorption coefficient, d is thickness of the thin film, R is the reflection and T is the transmission. Once α is calculated, then the band gap of any direct band gap semiconductors can be extracted by plotting $(\alpha h\upsilon)^2$ vs. hυ and by extrapolating the linear portion of the curve to the hυ axis. The intersection of this linear extrapolation with the hυ axis gives the band gap.

CHAPTER 3

STUDY OF MOLYBDENUM FILMS ON DIFFERENT SUBSTRATES

3.1 Introduction and Motivation

In this chapter, the use of in–situ real time spectroscopic ellipsometry (RTSE) for molybdenum (Mo) thin films deposited by DC magnetron sputtering on Si wafer has been investigated. Characterizations of the films deposited on different substrates are also presented. This chapter begins with an overview of the theoretical formalism, the parameters of interest, and the measurable quantities in RTSE. Furthermore, an experimental set–up for data acquisition and RTSE data analysis methodologies are presented as well. Specifically, our interest is to monitor and control film growth during the deposition process and enhance the existing knowledge base of relationships between film preparation and properties for $Cu(In,Ga)Se_2$ photovoltaic applications.

Use of different substrates can open up new possibilities for various applications with several advantages for their manufacturing. The choice of substrate is crucial as it defines various processing steps. The substrate should be compatible with vacuum processing i.e. not degas or degrade during the different deposition processes. It should be chemically non-reactive especially with Se or S when the absorber layer is deposited. It should not introduce impurities to the absorber material, which can cause defects and thus degrade the absorber material quality. In addition, it should have thermal stability as the subsequent deposition process requires to be operated in the temperature range of 400-650°C to produce higher efficiency device. In this chapter, various properties of molybdenum films deposited on five different substrates with their different characteristics (namely silicon wafer with native oxide, soda lime glass, borosilicate glass, 3.22 mm Pilkington TEC glasses with and without barrier for sodium diffusion (which will be referred to later as Si, SLG, BSG, TEC-WB and TEC-NB as the discussion proceeds)) have been analyzed. Si wafer is the sought out substrate to start any film analysis especially for Ellipsometry measurements for its numerous benefits and compatibilities in terms of optical and electrical properties. Soda lime glass is the main glass substrate in CIGS solar cell applications due to its chemical and physical properties. Detail about the usage of SLG substrate will be discussed in chapter 4. The use of borosilicate glass allows to vary the sodium content from near-zero to higher than that of the amount available from SLG substrates. It also permits to explore the various technique of sodium inclusion in the CIGS layer to enhance the deposition process, reproducibility and improvement of cell efficiency. Pilkington TEC glasses are manufactured with different conductivity levels and opaqueness to be compatible with a variety of thin film solar cell applications. In this study, TEC glasses with and without the barrier to block sodium from the substrates have been used. These substrates have a much higher softening point than those of SLG and BSG glasses in addition to the matching thermal coefficient of expansion to the molybdenum films. In substrates like SLG and BSG, CIGS deposition temperatures of 550˚C or less are normally used to circumvent deformation and/or adhesion issues. SIMS analysis was performed on the Mo/CIGS films deposited on SLG and BSG glasses to study the depth profile and compare the sodium content coming from the glasses. Device results on these two substrates are presented as well.

3.2 Deposition Process of Molybdenum Films and Substrates Used

Molybdenum thin films were fabricated using direct current (dc) magnetron sputtering. Five types of substrates were used in this study which are: Si wafer, soda lime glass (SLG), borosilicate glass (BSG), thick glasses from Pilkington with no barrier (TEC-NB) and with barrier (TEC-WB). The depositions were carried out in high purity (99.999%) argon ambient using a 2 inches diameter Mo sputtering target. The required argon pressure for sputtering was maintained at 10 mTorr. The duration of deposition was kept constant. The substrate temperature was kept constant during deposition. The dc power was kept constant at 150 W. The films and solar cells fabricated for SIMS and device analysis were produced following the processes mentioned in detail in the previous chapter.

3.3 Fundamental of Spectroscopic Ellipsometry

Photovoltaic cells are emerging as an important source of electrical energy in the world. Many materials and designs are employed for the manufacturing of these cells and major research is going on in these areas that promise low production cost and ease of manufacturing. Various characterization techniques are employed to understand the performance of these thin film cells. Spectroscopic Ellipsometry has emerged as a non-destructive, non-invasive optical technique that provides a natural fit to understand and monitor the performance of thin films [30]. Ellipsometry measures the change in polarization of light as it interacts with the sample. The technique derives its name by measuring the resulting elliptically polarized light from the sample, when a beam of light with known polarization is incidentally on it. Ellipsometers are very sensitive to the changes in the sub-monolayers in the materials during a real time dynamic process over a wide spectral range. Regardless of the material used, this characterization technique is ideal for the measurement of the film thickness and optical constants as well as other parameters that define the quality of the film.

Paul Drude derived the equations of ellipsometry in 1887 and performed the first experimental studies on both absorbing and transparent solids with and without any over-layers using the extreme sensitivity of the instrument. In 1945, Rothen introduced the word 'ellipsometry' to differentiate such measurements from that of polarimetry where the change of the state of polarization of light upon reflection is also used. In 1971, Palik and Bockris identified the normal incidence reflectance, R, as an additional experimental parameter to analyze ellipsometry data [42].

3.3.1 Principle of Operation

Light can be considered as an electromagnetic wave composed of both electric field and magnetic field waves. The electric field vector and the magnetic field vector are mutually perpendicular to the propagation direction of the wave. In order to understand the characterization technique using Ellipsometry, only the wave's electric field behavior in space and time is considered. A light wave can be represented mathematically [43] as

$$E(z,t) = E_0 \sin\left(-\frac{2\pi}{\lambda}(z - vt) + \xi\right) \tag{3.1}$$

where E is the electric field strength of the wave at any given time or place, E_0 is the maximum field strength or the amplitude, z is the distance along the direction of travel, t is time, v is the velocity of the light, λ is the wavelength, and ξ is the arbitrary phase angle which gives an offset when two waves are being combined.

Polarization is a property of light that describes the orientation of the oscillation of the waves. The electric field of a wave is always orthogonal to the direction of propagation. If a light source emits light that has components with electric fields oriented in all the directions perpendicular to the direction of travel, the light is considered to be an unpolarized light. When all the photons of the beam have its electric field oriented in one direction, the light is polarized. The electric field of the wave follows a specific path and traces out a distinct shape at any point. When the two orthogonal light waves are in phase, the resulting waves are called linearly polarized. When the waves are equal in amplitude and 90° out of phase, the resultant wave is circularly polarized. But if the orthogonal waves are of arbitrary amplitude and phase, the waves are elliptically polarized [44]. Figure 3.1 represents the combination of the orthogonal waves to represent different types of polarization. The key property of polarized light for ellipsometry is the change of plane polarized light into elliptically polarized light or elliptically polarized light into plane polarized light upon reflection [45].

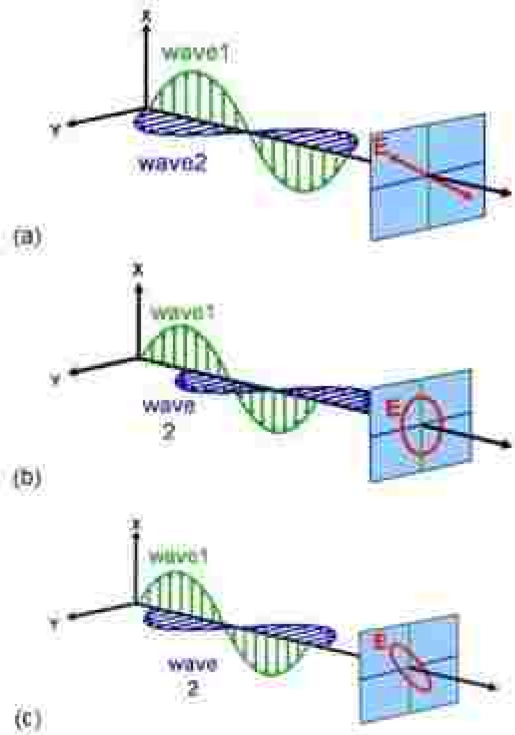

Figure 3.1: Combination of the orthogonal waves to represent different types of polarization, (a) Linear Polarization, (b) Circular Polarization and (c) Elliptical polarization [44].

When the light interacts with a material, Maxwell's equations should be satisfied at all times. In isotropic, homogenous, and non-magnetic media, the solution for Maxwell's equations for the electric field can be given as [34]:

$$\vec{E}(\vec{r},t) = \vec{E}_0 \exp\left[i\left(\frac{\vec{q}.\vec{r}}{c} - \omega t\right)\right] \tag{3.2}$$

where ω is the angular frequency of the wave, $\vec{q}$ is the complex wave vector along the direction of propagation, and $\vec{E}_0$ is the complex electric field vector perpendicular to $\vec{q}$ defining the amplitude and polarization state of the wave. The complex wave vector $\vec{q}$ is defined as:

$$q^2 = \left(\frac{\omega}{c}\right)^2 \left[\varepsilon_r + i\left(\frac{4\pi\sigma}{\omega}\right)\right] \tag{3.3}$$

A part of the complex wave vector equation can be equated to the complex index of refraction $\tilde{n}$,

$$\tilde{n}^{\,2} = \left[\varepsilon_r + i\left(\frac{4\pi\sigma}{\omega}\right)\right] \tag{3.4}$$

The complex parameter $\tilde{n}$ describes the interaction of light with the material and it consists of two values used to describe the optical properties of the material and is defined as

$$\tilde{n} = n + ik \tag{3.5}$$

where ‘n’ is called the index of refraction and ‘k’ is the extinction coefficient. The optical properties can also be represented as a complex dielectric function given as:

$$\tilde{\varepsilon} = \varepsilon_1 + i\varepsilon_2 \tag{3.6}$$

the real part of the dielectric function ε_1 describes the electrical polarization response of the material, whereas the imaginary part ε_2 signifies the material losses [46]. The complex dielectric function can be related with the index of refraction with the following convention:

$$\tilde{\varepsilon} = \widetilde{n^2} \tag{3.7}$$

Thus the solution to the Maxwell’s equation can be re-written as

$$\vec{E}(\vec{r},t) = \vec{E}_0 \exp\left[-\omega\frac{\vec{k}.\vec{r}}{c}\right] \exp i\left[\omega\frac{\vec{n}.\vec{r}}{c} - \omega t\right] \tag{3.8}$$

The exponential factor containing k, called the extinction coefficient, describes the loss of wave energy to the material and is related to the absorption coefficient α by [47]:

$$\alpha = \frac{4\pi \, \mathrm{k}}{\lambda} \tag{3.9}$$

When a light wave is incident on a plane, some of the light is reflected and some gets transmitted. The plane polarized waves in the plane of incidence are known as parallel waves (‘p’ waves) and the plane polarized waves perpendicular to the plane of incidence are known as perpendicular waves (‘s’ waves, ‘s’ is taken from the German word “senkrecht”, which means perpendicular). Ellipsometry deals with the change of ‘p’ and ‘s’ components on reflection or transmission in relation to each other [48].

Fresnel’s equations describe the amount of light reflected and transmitted at an interface between the materials. The Fresnel reflection coefficient r is the ratio of the amplitude of the reflected wave to the amplitude of the incident wave for the single interface and the coefficients are given by [49]:

$$r_s = \left(\frac{E_{0r}}{E_{0i}}\right)_s = \frac{n_i \cos(\Phi_i) - n_t \cos(\Phi_t)}{n_i \cos(\Phi_i) + n_t \cos(\Phi_t)} \tag{3.10}$$

$$r_p = \left(\frac{E_{0r}}{E_{0i}}\right)_p = \frac{n_t \cos(\Phi_i) - n_i \cos(\Phi_t)}{n_i \cos(\Phi_t) + n_t \cos(\Phi_i)} \tag{3.11}$$

Reflectance is defined as the ratio of the reflected intensity to the incident intensity. For a single interface, the reflectance for parallel and perpendicular incident waves are given by [50]:

$$R^P = |r^P|^2 \tag{3.12}$$

$$R^S = |r^S|^2 \tag{3.13}$$

A known polarization is reflected or transmitted from the sample and the output polarization is measured. The ellipsometer measures the change in polarization expressed as a complex ratio [33]:

$$\rho = \tan(\psi)\, e^{i\Delta} \tag{3.14}$$

where Ψ is the amplitude ratio and Δ represents the change in phase difference between the p- and s-polarization respectively. Figure 3.4 explains the principle of measurement of ellipsometry. The phase difference between the parallel component and the perpendicular component of the incident wave is δ_1. The phase difference between the parallel component and the perpendicular component of the reflected wave is δ_2. Thus the change in phase difference is expressed as $\Delta = \delta_1 - \delta_2$ and its value can change from 0° to 360° [51].

Regarding the amplitude, the perpendicular and parallel components may change upon reflection. The ratio of the amplitude of the reflected wave to the amplitude of the incident wave for the parallel and perpendicular components are given by $|R^P|$ and $|R^S|$. Thus the amplitude is defined as $\tan \Psi = \frac{|R^P|}{|R^S|}$. The value of Ψ can vary from 0° to 90° [52].

The main tools used for collecting ellipsometry data include a light source, a polarization generator, a sample, a polarization analyzer, and a detector. Figure 3.2 displays the block diagram for instrumentation. The monochromatic light source is obtained using either a laser, an arc lamp or a polychromatic source and filtering. The polarization generator and analyzer are optical components used to manipulate the polarization. A polarization generator is used to convert the unpolarized light to linearly polarized light whereas a polarization analyzer converts the elliptically polarized light to linearly polarized light. The detector is used to measure the light intensity.

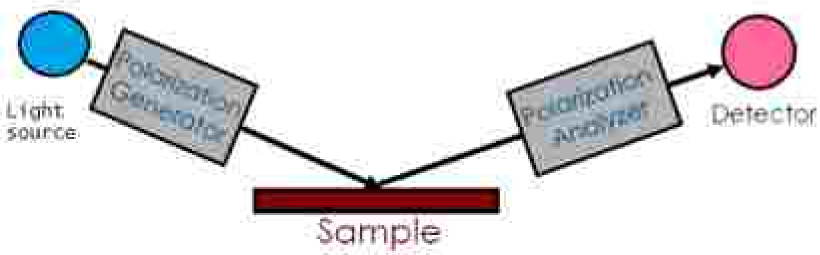

Figure 3.2: The instrumentation for Ellipsometry [48].

The different ellipsometer configurations include rotating analyzer (RAE), rotating polarizer (RPE), rotating compensator (RCE), and phase modulation (PME) as are represented in Figure 3.3. The Rotating analyzer ellipsometer configuration uses a polarizer to define the incoming polarization and then a rotating analyzer is used to analyze the outgoing light from the sample. The polarizer allows the passage of light of a preferred electric field orientation. The axis of the polarizer is oriented between the parallel and perpendicular plane such that the light falls directly on the sample. The linearly polarized light gets reflected from the sample surface as elliptically polarized light and it is passed through a rotating analyzer. In some configurations, a rotating compensator is used to shift the relative phase of orthogonal vector components resolved along the fast and slow axes of the compensator. The phase shift between the p and s components of the electric field vector depends on the angle of the fast axis of the compensator with respect to the field of incidence. The beam of light reflects from the sample surface thus inducing a change in the nature of the polarization state modulation. Upon specular reflection, the beams pass through a polarization analyzer and are collected by the spectrograph [45]. The beam splitter within the spectrograph directs the low energy photons to an InGaAs photodiode array and the high energy photons to a CCD detector [46]. The detector converts the light to voltage, to determine the reflected polarization. The data thus obtained is compared to the input polarization to determine the change in polarization as reflected from the sample. This accounts to the Psi and delta measurement.

(a) Rotating-analyzer ellipsometry (PSA$_R$)

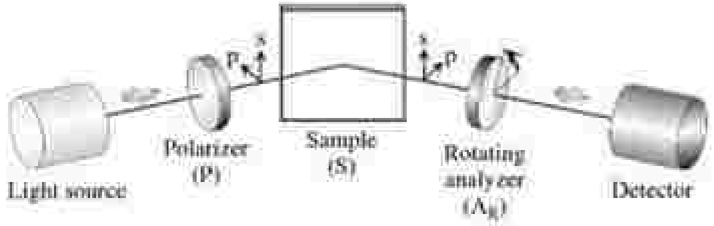

(b) Rotating-analyzer ellipsometry with compensator (PSCA$_R$)

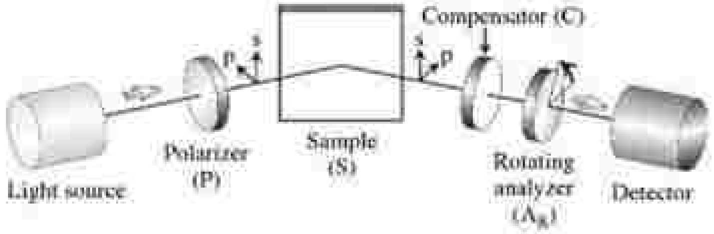

(c) Rotating-compensator ellipsometry (PSC$_R$A)

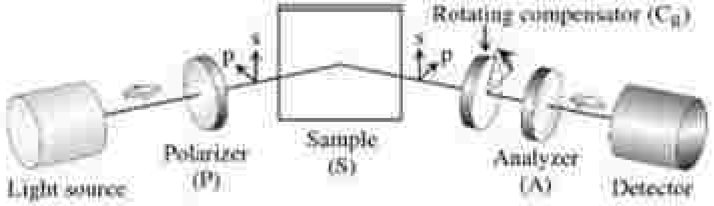

(d) Phase-modulation ellipsometry (PSMA)

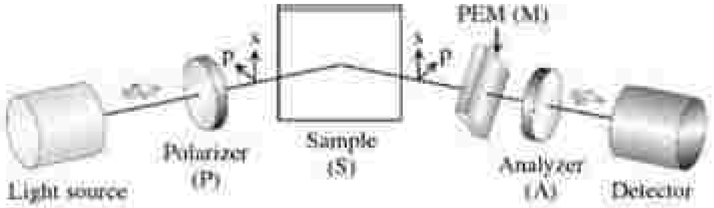

Figure 3.3: Optical configurations of ellipsometry instruments: (a) Rotating analyzer ellipsometry (RAE), (b) Rotating analyzer ellipsometry with compensator, (c) Rotating compensator ellipsometry (RCE), and (d) Phase modulation ellipsometry (PME) [46].

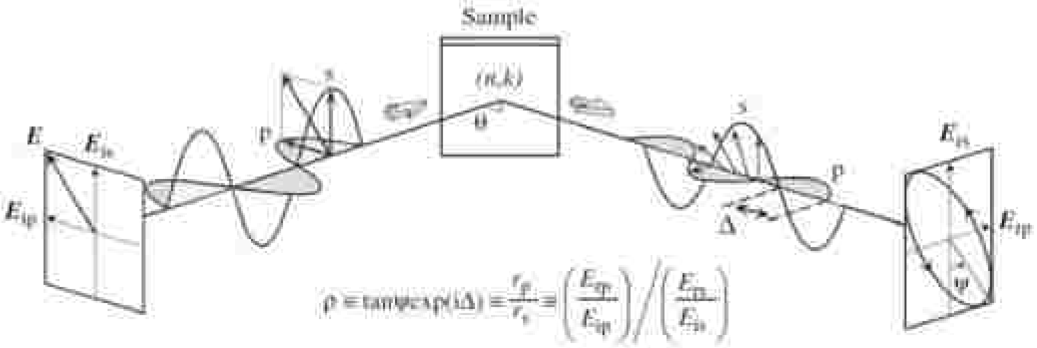

Figure 3.4: Measurement principle of Ellipsometry [46].

Ellipsometry measures the change in light polarization and determines the sample's material properties such as film thickness and optical constants (Figure 3.4). Pseudo optical constants can be derived from the ellipsometry measurement for the bulk materials [14]. Figure 3.5 shows the data analysis procedure in spectroscopic ellipsometry.

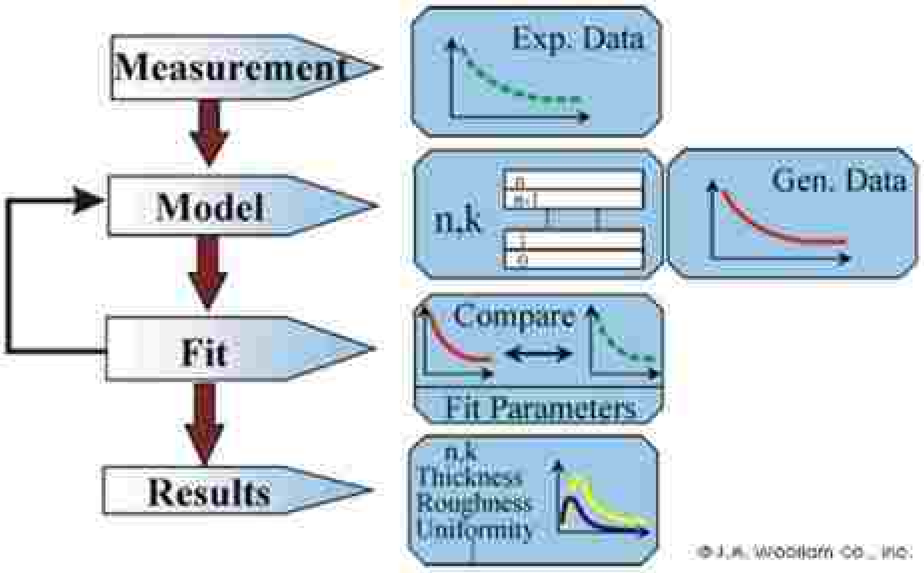

Figure 3.5: Flowchart for Ellipsometry analysis [46].

After measurement of the data, an optical model is constructed corresponding to the sample. For a sample structure with known component materials and dielectric functions, an optical model is constructed by placing the layers in the right sequence including the thickness and optical properties of each layer. If the dielectric functions of the material are not available, different dielectric function models are used to mathematically analyze the layers. For dielectric function modeling in a transparent region, Sellmeier or Cauchy models are used. A Drude model is used to analyze free carrier absorption. Various models such as Lorentz model, Tauc-Lorentz model, harmonic oscillator approximation (HOA), critical point parabolic band (CPPB) model, and model dielectric function (MDF) are used to express the electric polarization in the visible/UV region. Intermix layers and void fractions can be analyzed to improve the correlation with the theoretical and experimental techniques. The predicted response is calculated from the Fresnel's equations using the optical model and the response describes the material's thickness and optical constants. The calculated values are compared with the experimental data. Regression is used to find the best match between the model and the experimental data. A least square regression algorithm is used to minimize the differences between the generated spectra and the experimental data by adjusting the variable parameters in the model. Mean Squared Error (MSE) is taken as an estimator to represent the quality of the match between the generated data and experimental data. MSE is written as:

$$MSE = \sqrt{\frac{1}{2N-M}\sum_{i=1}^{N}\left[\left(\frac{\psi_i^{\mathrm{mod}}-\psi_i^{\mathrm{exp}}}{\sigma_{\psi,i}^{\mathrm{exp}}}\right)^2+\left(\frac{\Delta_i^{\mathrm{mod}}-\Delta_i^{\mathrm{exp}}}{\sigma_{\Delta,i}^{\mathrm{exp}}}\right)^2\right]} \qquad (3.15)$$

where N is the number of (ψ, Δ) pairs, M is the variable parameters in the model and σ is the standard deviation of the experimental data. The unknown parameters are varied until a minimum MSE is obtained.

The thickness of the film and the optical constants are the main data that are extracted using the Ellipsometry process. The complex dielectric constant ε and the absorption constant α can also be obtained from the optical constants. Also, the reflectance (R) and the transmittance (T) at different angles of incidence can be calculated from the thickness [47]. The film thickness is determined by the interference between the light travelling through the film and the light reflected from the surface. The optical constants n and k should also be determined along with the thickness to obtain accurate results. The thickness of the film will indicate the length of the path travelled by the light through the film. The index determines the velocity of the light wave through the sample and the refracted angle. But the optical constants will vary for different wavelengths. Thus it is important to obtain the constants at all wavelengths. A dispersion relationship is used to explain the optical constants versus wavelength [47]. The parameters of the relationship allow the overall constants to match the experimental results. The model can be optimized to the measured data by varying the wavelength independent parameters such as angle of incidence, adjusting the layer thickness, adding Lorentz parameters, EMA fractions, amorphous semiconductor parameters [48].

3.4 Spectroscopic Ellipsometry Measurements of Molybdenum Films

Figure 3.6 shows the schematic of the experimental setup used in this study to monitor by Real Time Spectroscopic Ellipsometry (RTSE) the growth of molybdenum thin films. RTSE measurements were carried out in-situ during the film growth using a rotating compensator, multichannel instrument with an energy range of 0.75 – 6.5 eV at an angle of incidence of 65° (model M2000-DI, J. A. Woollam Company, Lincoln, NE) with the capability of collecting 706 wavelengths. Light of broad wavelength is created with

Deuterium (D_2) and Quartz–Tungsten–Halogen (QTH) lamps, which is collimated and linearly polarized after passing through the stationary polarizer with its transmission axis (TA) set at 45º with respect to the plane of incidence. The linearly polarized light is transmitted through a rotating compensator, which is an anisotropic optical element with two axes, fast and slow, for the transmitted light. The p– and s–components of the electric field (E), which were in phase (linearly polarized light), emerge out of phase from the compensator. This phase shift depends on the angle of the fast axis with respect to the plane of incidence. The net result is the time– dependent or modulated polarization state of the photons leaving the compensator, which varies between elliptical and linear polarization states. The polarized light is then reflected from the sample surface, thus inducing the change in nature of the polarization state modulation. Upon specular reflection, photons pass through a polarizer, which functions as an analyzer. Finally, photons are collected by a spectrograph. Within the spectrograph, a beam splitter directs the low energy (0.75–1.25 eV) photons to an InGaAs photodiode array and the high energy photons (1.25–6.5 eV) to a CCD detector, where the irradiance associated with the incoming photons is accurately determined versus pixel number. The light collected by the InGaAs photodiode array and Si CCD detectors is split into 706 wavelength channels and can be collected in a time as short as 50 ms. Multiple data sets are usually averaged to improve the signal to noise ratio. Pairs of (ψ, Δ) spectra were collected with a 3-s acquisition time. The ellipsometric parameters (ψ) of the Mo films are plotted in Figure 3.7 as a function of time for different energies at room temperature for a silicon substrate. A simple model as shown in Figure 3.8 was used to study the Mo films and Figure 3.9 explains the RTSE data analysis algorithm. The thickness of the growing film can be estimated from the growth rate at any particular time of deposition by a mathematical inversion trial. Using these trial dielectric functions as a reference for the growing film, a least square regression analysis can now provide a good estimation of the thickness. Therefore, this method enables one to determine the dielectric functions and the structure of the sample simultaneously [30]. A Bruggeman effective medium approximation (EMA) layer with 50% Mo and 50% voids was used to model the surface roughness.

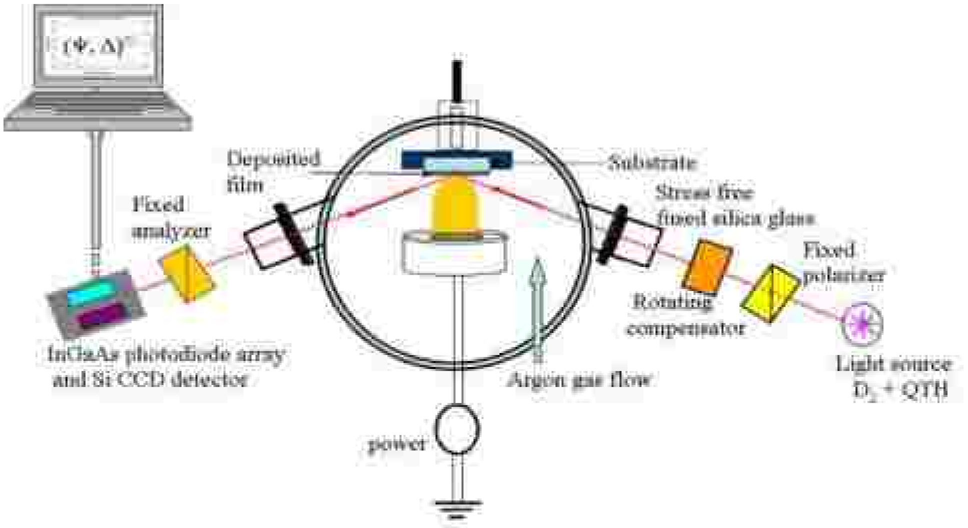

Figure 3.6: Schematic diagram of experimental setup for the deposition of Molybdenum thin-film with optical monitoring by RTSE.

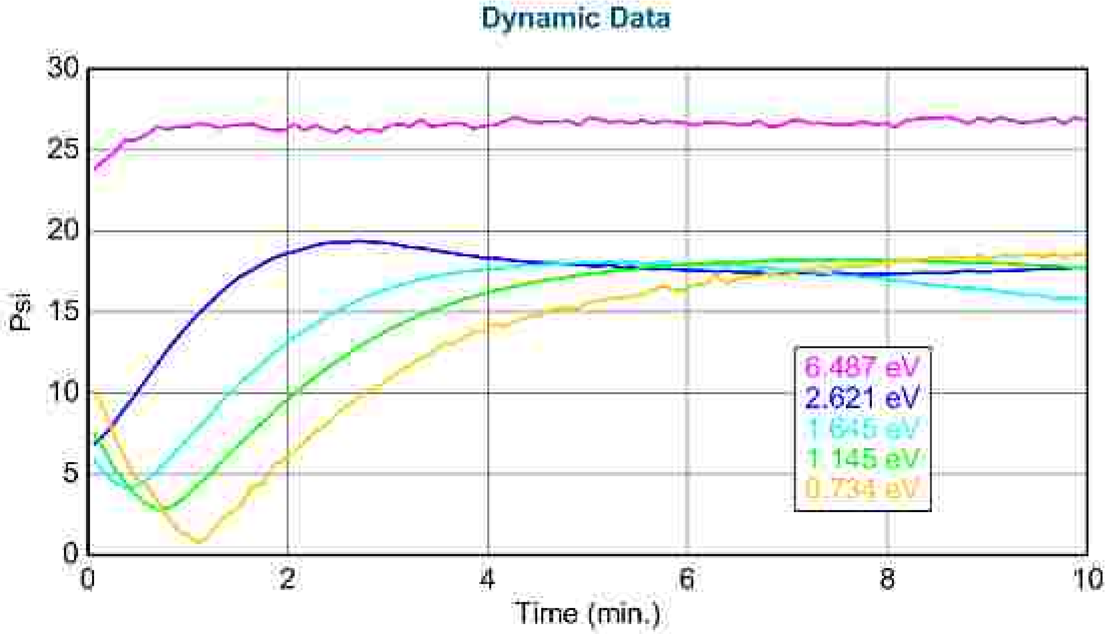

Figure 3.7: (ψ) spectra of a Mo film on Si as a function of time using RTSE at room temperature.

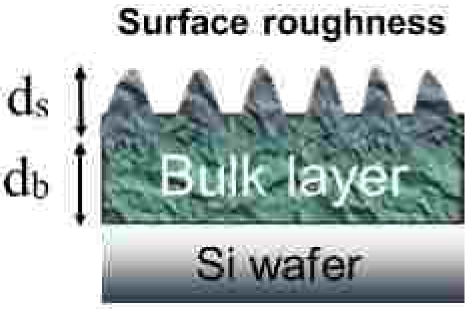

Figure 3.8: Optical model used to analyze our Mo thin films.

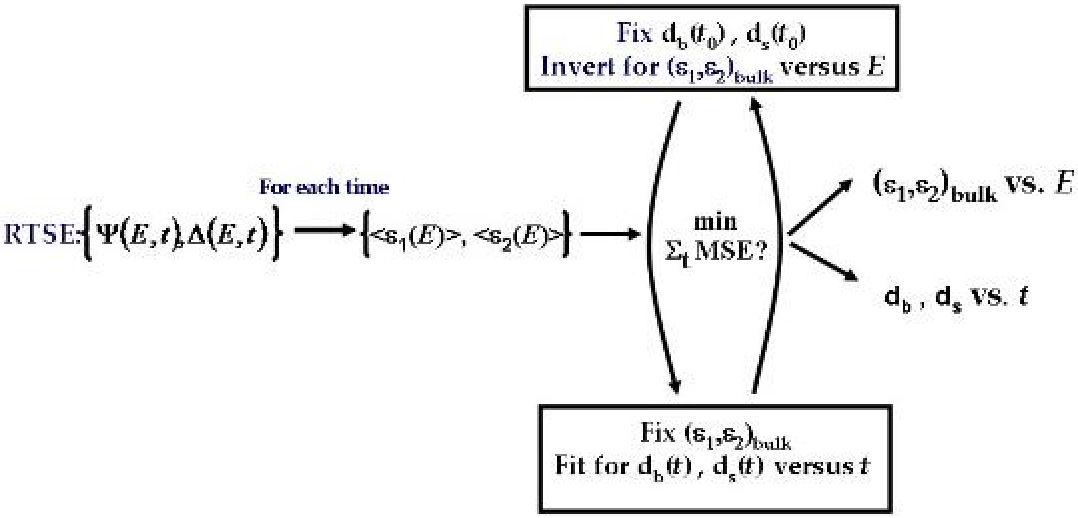

Figure 3.9: RTSE data analysis algorithm [45].

Figure 3.10 shows the evolution of the surface roughness and the bulk layer thicknesses as a function of deposition time extracted from RTSE as the film is deposited at room temperature. During the initial stage of growth, the incident Mo atoms nucleate forming separate islands which is evidenced by a sharp increase in the surface roughness thickness, in this study around 8 nm. Island coalescence is characterized by a subsequent decrease in surface roughness simultaneously with the onset of bulk layer growth [38]. After complete coalescence of the islands, the surface roughness thickness increases slightly to a value of 4.3 nm. The bulk layer becomes fully opaque at large thickness values, and as a result, the thickness cannot be determined.

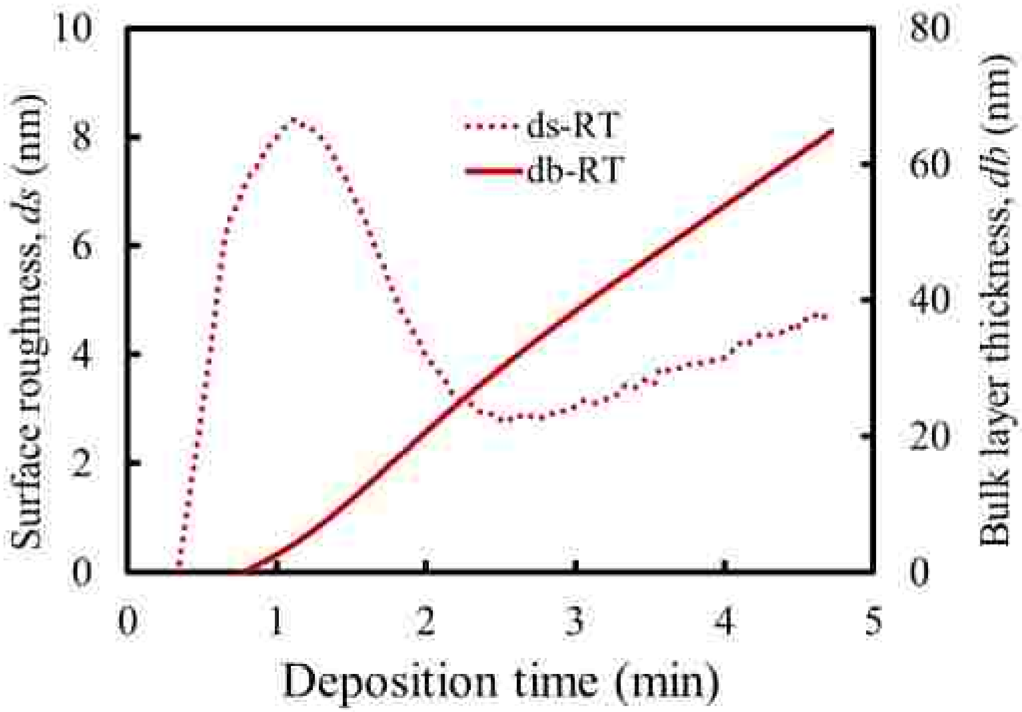

Figure 3.10: Evolution of surface roughness (dashed line) and bulk layer thickness (solid line) at room temperature (RT) obtained by RTSE for a Mo film on Si substrate.

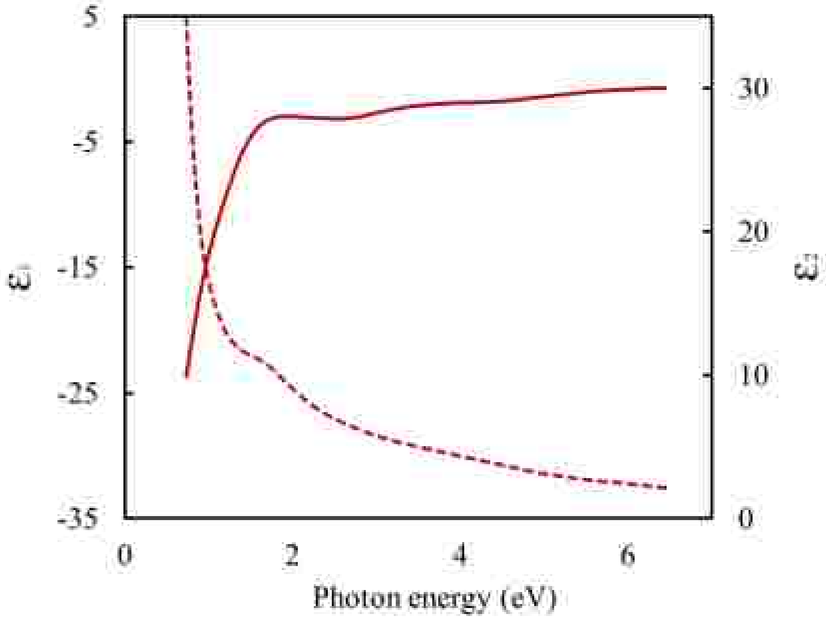

Figure 3.11: Real and imaginary parts of the dielectric functions for a Mo film deposited on a Si substrate at room temperature determined by ex-situ spectroscopic ellipsometry.

Ex-situ spectroscopic ellipsometry data were also acquired after the film growth at angles of incidence of 55°, 65° and 75°. Figure 3.11 depicts the real (ε_1) and imaginary (ε_2) components of the complex dielectric functions at room temperature. One can see typical behavior for metal films, which can be fitted with a Drude oscillator at low energy and a Lorentz oscillator at higher energy.

The Drude oscillator follows the following equation [52]:

$$\varepsilon(E) = \varepsilon_\infty - \frac{E_p^2}{E(E + i\Gamma)} \tag{3.16}$$

where Ep is the free-electron plasma energy and ε_∞ is the contribution to the dielectric function due to higher energy oscillators, that is, the contribution from the interband transitions and Γ is the broadening parameter. Drude model allows for a determination of the broadening parameter, which is inversely proportional to the relaxation time that is $\tau=h/\Gamma$, where h is the Planck's constant.

Only one sample of the real and imaginary parts of the dielectric functions determined by ex-situ spectroscopic ellipsometry analysis for the Mo films deposited at room temperature are shown in Figure 3.11 for clear representation since the other substrates produce similar dielectric functions. The main difference between the substrates was a higher surface roughness for the SLG, BSG, TEC-NB compared to the Si and TEC-WB substrates, changing from 5 nm down to 3 nm. Also, the resistivity of the films, extracted from the Drude oscillator, was higher for the Si and TEC-WB compared to the other substrates. These two sets of data will be compared in the next section with other measurements.

3.5 Effect of Different Substrates

Tables 3.1 and 3.2 show the chemical compositions of glass with low sodium (borosilicate glass) and glass with higher sodium (soda lime glass) types. The main constituent, SiO_2 is around 80% for BSG and 73% for SLG. Both glasses have around 2% Al_2O_3. It can be noted that 4% sodium is present in BSG in the form of Na_2O which is lower than the required amount to provide passivation in CIGS to get better cell performance. Table 3.3 lists the comparison between the valuable physical parameters between these above mentioned glasses. Coefficient of thermal expansion (CTE) is significantly different between these two glass substrates. Table 3.4 shows the density and CTE of different layers of a complete CIGS solar cell.

Table 3.1 Chemical composition of borosilicate glass [53].

Composition	**(Percent approx.)**
SiO_2	80.6%
B_2O_3	13.0%
Na_2O	4.0%
Al_2O_3	2.3%
Miscellaneous Traces	0.1%

Table 3.2 Chemical composition of soda lime glass [53].

Composition	**(Percent approx.)**
SiO_2	73.0%
Na_2O	14.0%
CaO	7.0%
MgO	4.0%
Al_2O_3	2.0%

Table 3.3 Physical properties of soda lime and borosilicate glass substrates [54, 55].

Substrate	**Density (g/cm^3)**	**CTE ($10^{-6}K^{-1}$)**	**Strain point (°C)**	**Anneal point (°C)**	**Soften point (°C)**
SLG	2.5	9	511	545	724
BSG	2.23	3.2	510	560	821

Table 3.4 Physical properties of CIGS solar cell materials [54, 55].

Material	**Density (g/cm^3)**	**CTE ($10^{-6}K^{-1}$)**
Mo	10.2	4.8
CIGS	5.9	8-11
CdS	4.8	4.5
ZnO	5.6	4.75/2.9

Figures 3.12 shows the bulk concentration, mobility and resistivity comparisons of the Mo films deposited on five different substrates by Hall Effect measurements. It can be seen that the values of these parameters show a dependency on the presence of sodium in the films, although the values varies within a very short range. The resistivity values from the Hall Effect measurement were compared with both 4-point probe measurements and values extracted from the ellipsometry analysis and showed good correlation.

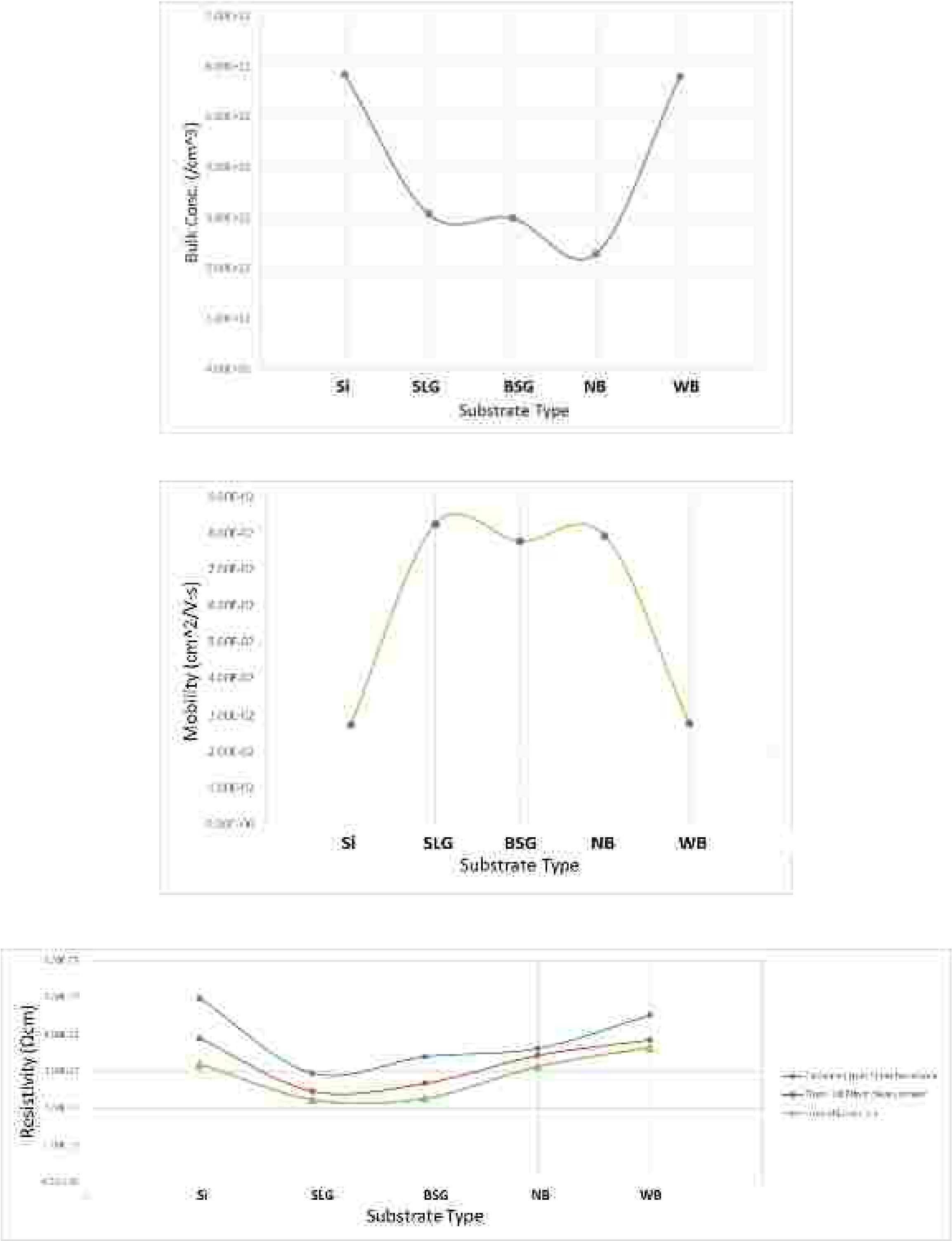

Figure 3.12: Hall Effect measurements of Mo films on five different substrates (bulk concentration, mobility and resistivity). Resistivity extracted from Ellipsometry analysis and 4-point probe is also shown for comparison.

Figures 3.13 and 3.14 show the AFM images of the bare substrates and the Mo films on five different substrates. Figure 3.15 show the correlation between the RMS roughness values for substrates and the films and it can be seen easily that the film roughness depends on the roughness of the substrates, lowest for Si and highest for TEC-NB. The film roughness varies from 2.5 nm to 4.8 nm. There is an expected inverse correlation which can be seen between the film roughness and resistivity values.

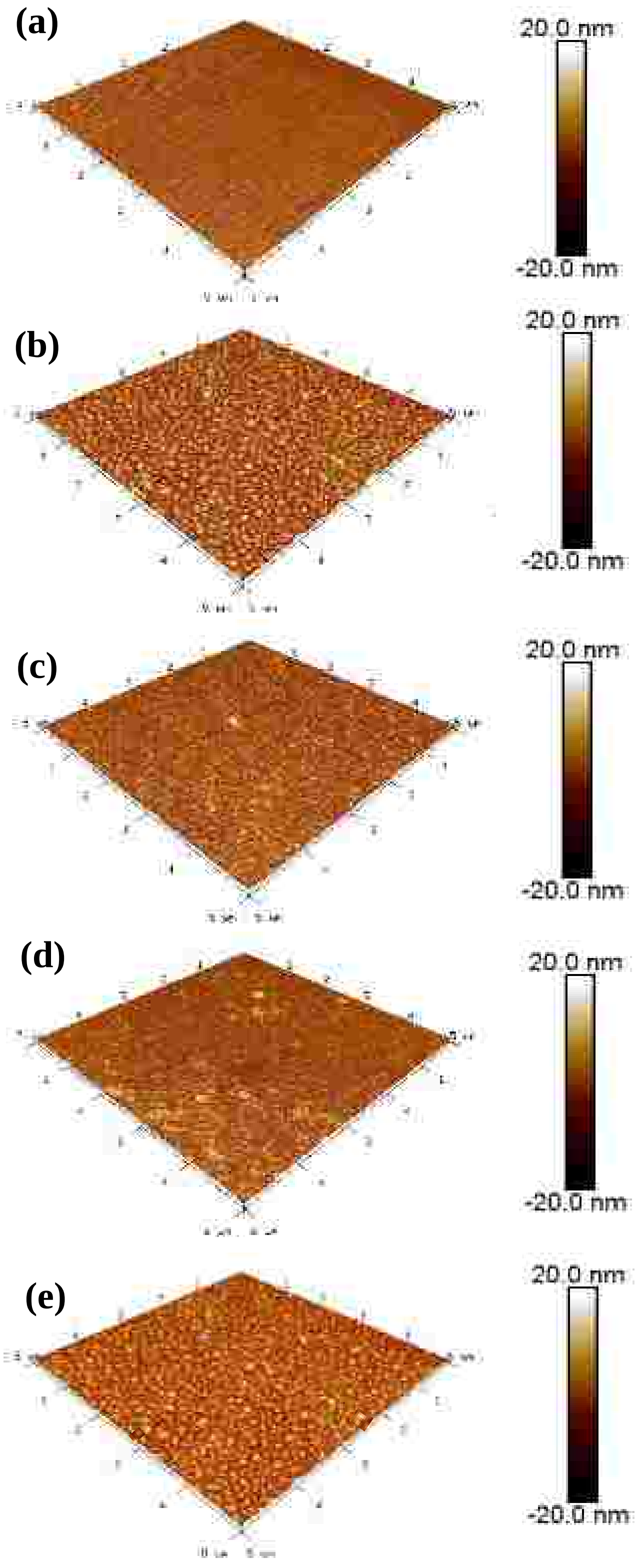

Figure 3.13: AFM images on bare substrates (a) Si wafer, (b) soda lime glass, (c) borosilicate glass, (d) Pilkington glass with no barrier and (e) Pilkington glass with barrier.

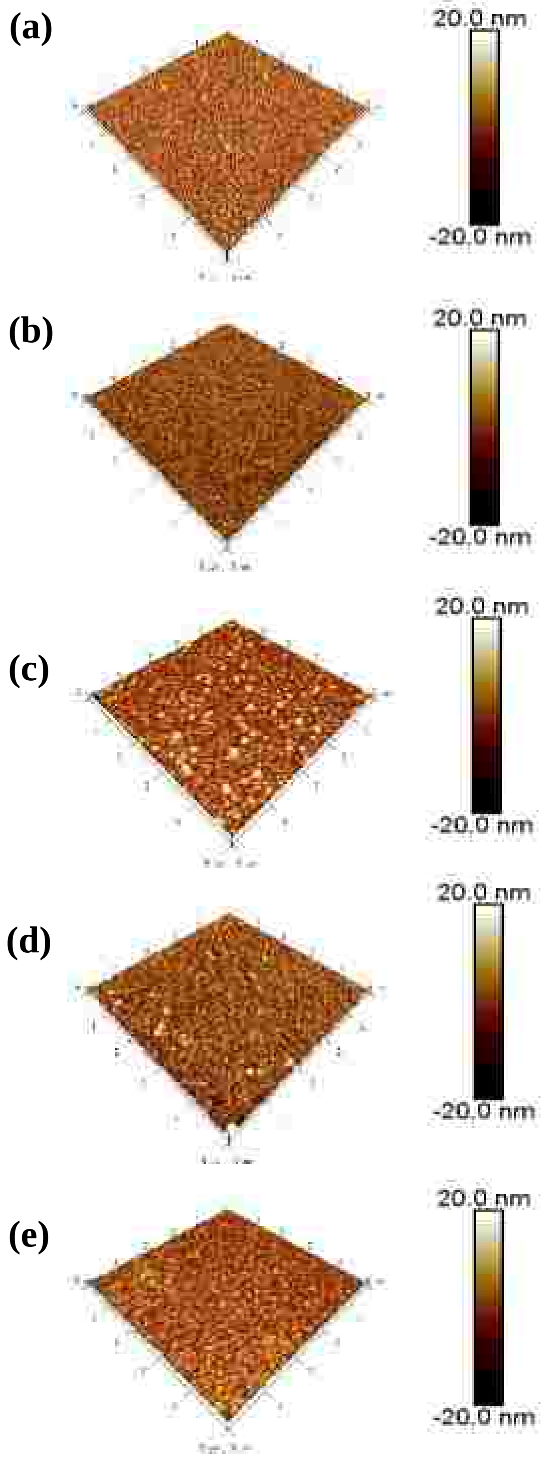

Figure 3.14: AFM images of Mo films on (a) Si wafer, (b) soda lime glass, (c) borosilicate glass, (d) Pilkington glass with no barrier and (e) Pilkington glass with barrier.

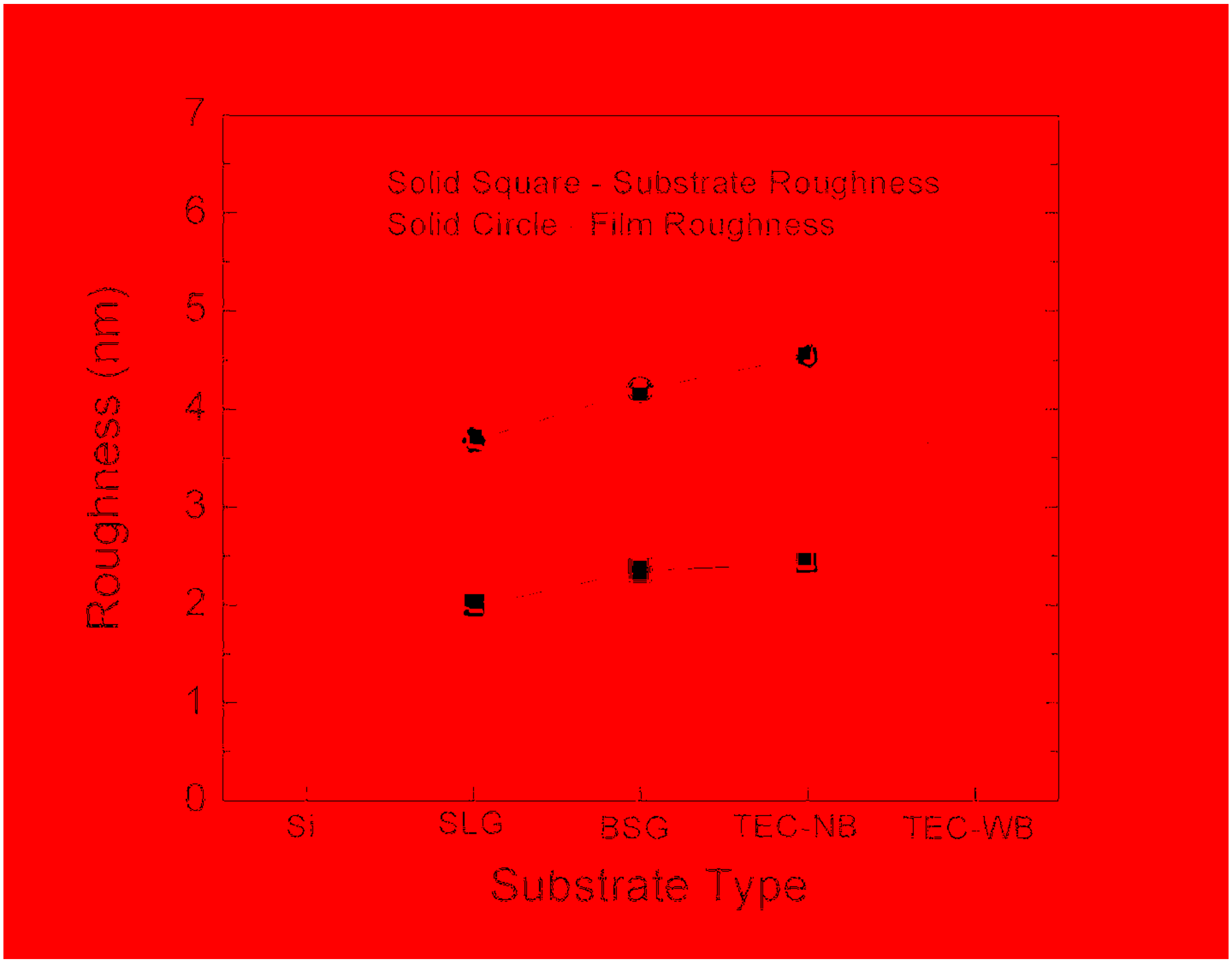

Figure 3.15: AFM images of Mo films on (a) Si wafer, (b) soda lime glass, (c) borosilicate glass, (d) Pilkington glass with no barrier and (e) Pilkington glass with barrier.

Figure 3.16 shows the X-ray diffraction (XRD) plot for Mo thin films deposited at room temperature on all five substrates. It was observed that the films are preferentially (110) oriented, whatever the substrate used was. A small change in d-spacing was observed for the (110) peak as a function of the substrate (Table 3.5), which indicates a small change in strain in the films depending on the substrates. The average crystallite size of the films was determined using Scherrer's equation (Equation 2.2 described in Chapter 2) and is plotted along with the FWHM in Figure 3.17.

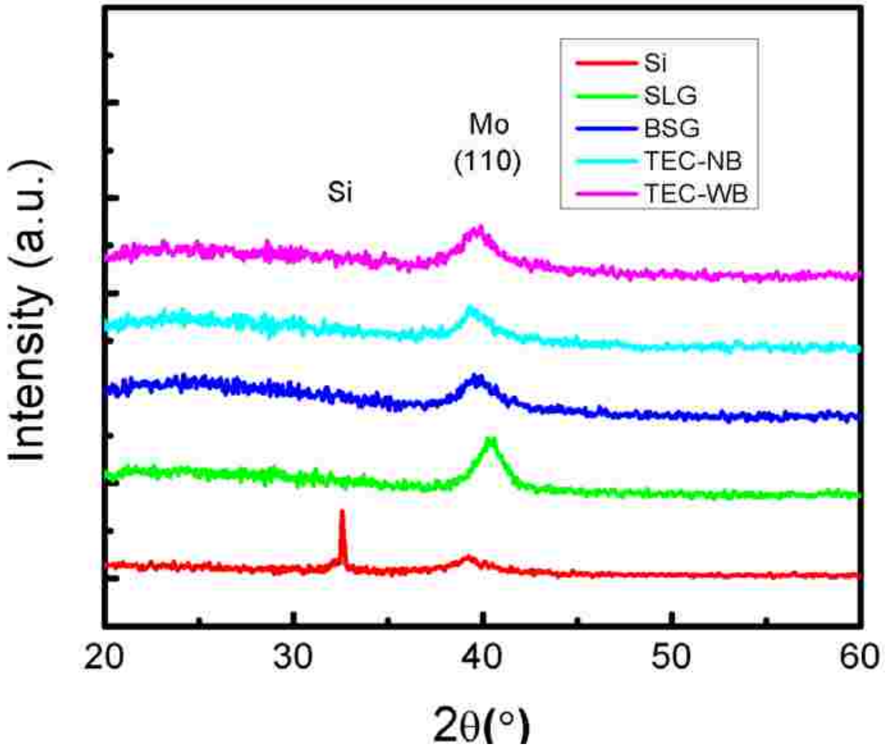

Figure 3.16: XRD patterns of the (110) reflection of Mo films on various substrates deposited at room temperature.

Table 3.5 *d*-spacing of Mo films at (110) peak deposited on different substrates.

Substrate	**2θ(°)**	**d(Å)**
Si wafer	40.32	2.235
SLG	40.49	2.226
BSG	39.75	2.266
TEC-no barrier	39.33	2.289
TEC-with barrier	39.69	2.269

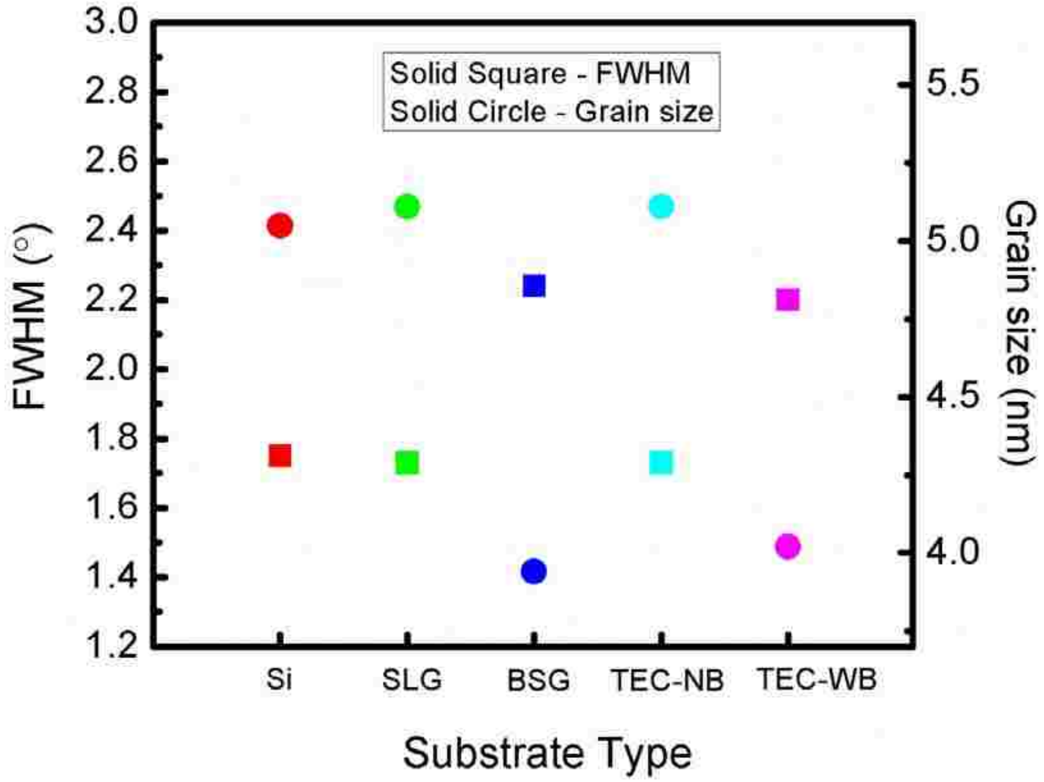

Figure 3.17: FWHM and corresponding grain size of Mo films on various substrates deposited at room temperature.

For all substrates, there is not much change in average grain size, with values ranging from 4 nm to 5 nm for all films. Figure 3.18 shows the plan-view SEM image revealing small-grain microstructure of the film grown on all different substrates in this study, correlating well with the XRD results.

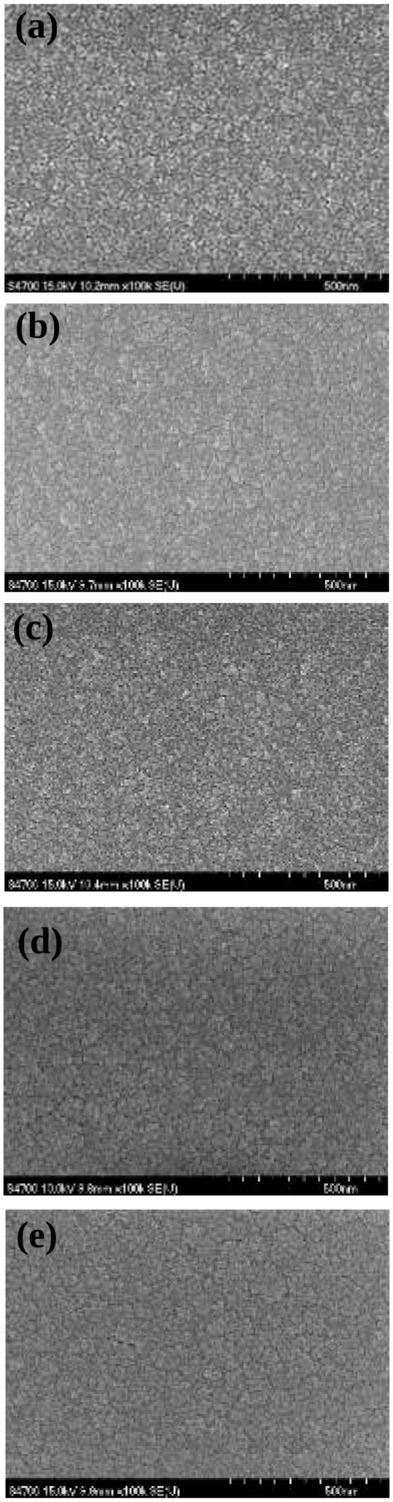

Figure 3.18: SEM plan-view images of various Mo films on (a) Si wafer, (b) soda lime glass, (c) borosilicate glass, (d) Pilkington glass with no barrier and (e) Pilkington glass with barrier.

SIMS analysis are shown in Figures 3.19 and 3.20 for BSG and SLG substrates to compare the amount of Na supplied from the substrates which is going through the Mo and CIGS films. Here, the CIGS layer was deposited on bilayer Mo films for both substrates. The different sputter time in these plots are due to the difference in the scanning rate while obtaining depth profile by SIMS measurements. It can be seen that the Na intensity for the BSG/Mo substrate is around 100 counts, while the SLG/Mo interface has an intensity count of 100000. This in turn is responsible for very low Na level in CIGS when using BSG glass.

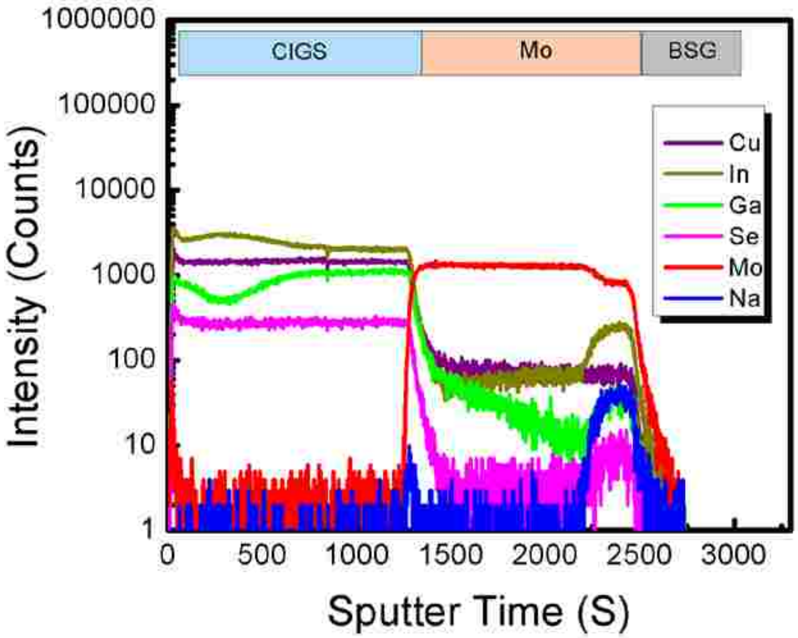

Figure 3.19: SIMS depth profile through Mo/CIGS deposited on BSG substrate. CIGS layer was deposited on a bilayer Mo film.

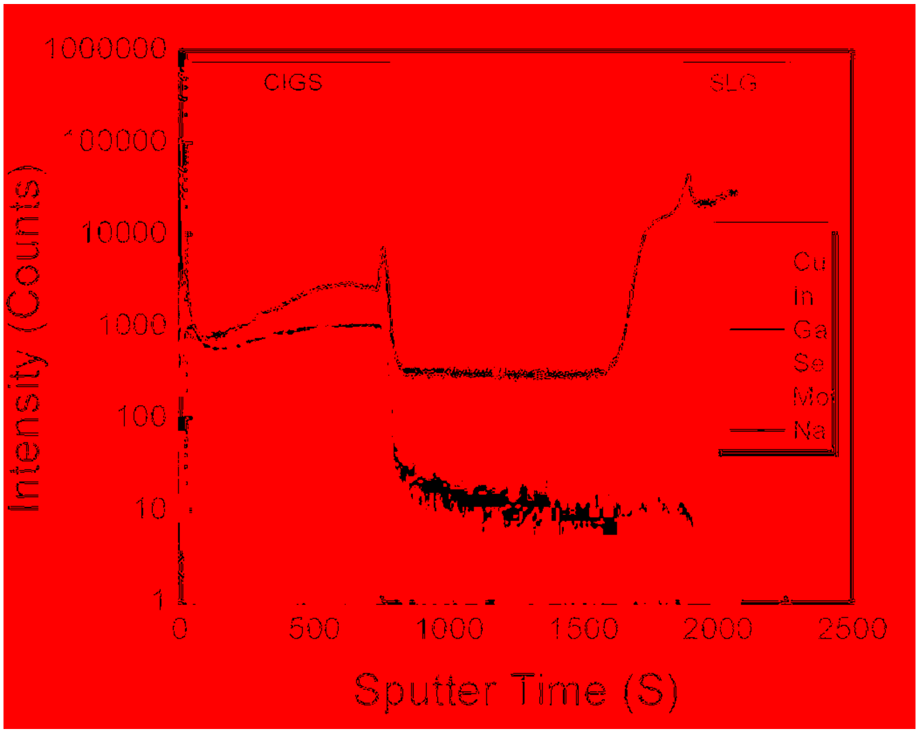

Figure 3.20: SIMS depth profile through Mo/CIGS deposited on SLG substrate. CIGS layer was deposited on a bilayer Mo film.

To confirm the effect of sodium (and of the substrate) on solar cell efficiency, full devices were fabricated with the following structure: Substrate/Mo/CIGS/CdS/ZnO/AZO/grids. The two substrates that were analyzed by SIMS were used to fabricate these cells, which are SLG and BSG. The devices were then analyzed using current density-voltage (J-V) and Quantum efficiency (QE) measurements. The results are reported in Figure 3.21 and Table 3.6. As one can see, there is a drastic difference in efficiency between the two substrates. This difference in due to lower V_{OC} and FF for the BSG substrate, while the current is similar in both cases as can be seen by the QE measurements. The lower voltage and fill factor are associated with the lack of sodium in the BSG (as seen by SIMS), since sodium tends to passivate traps in the CIGS.

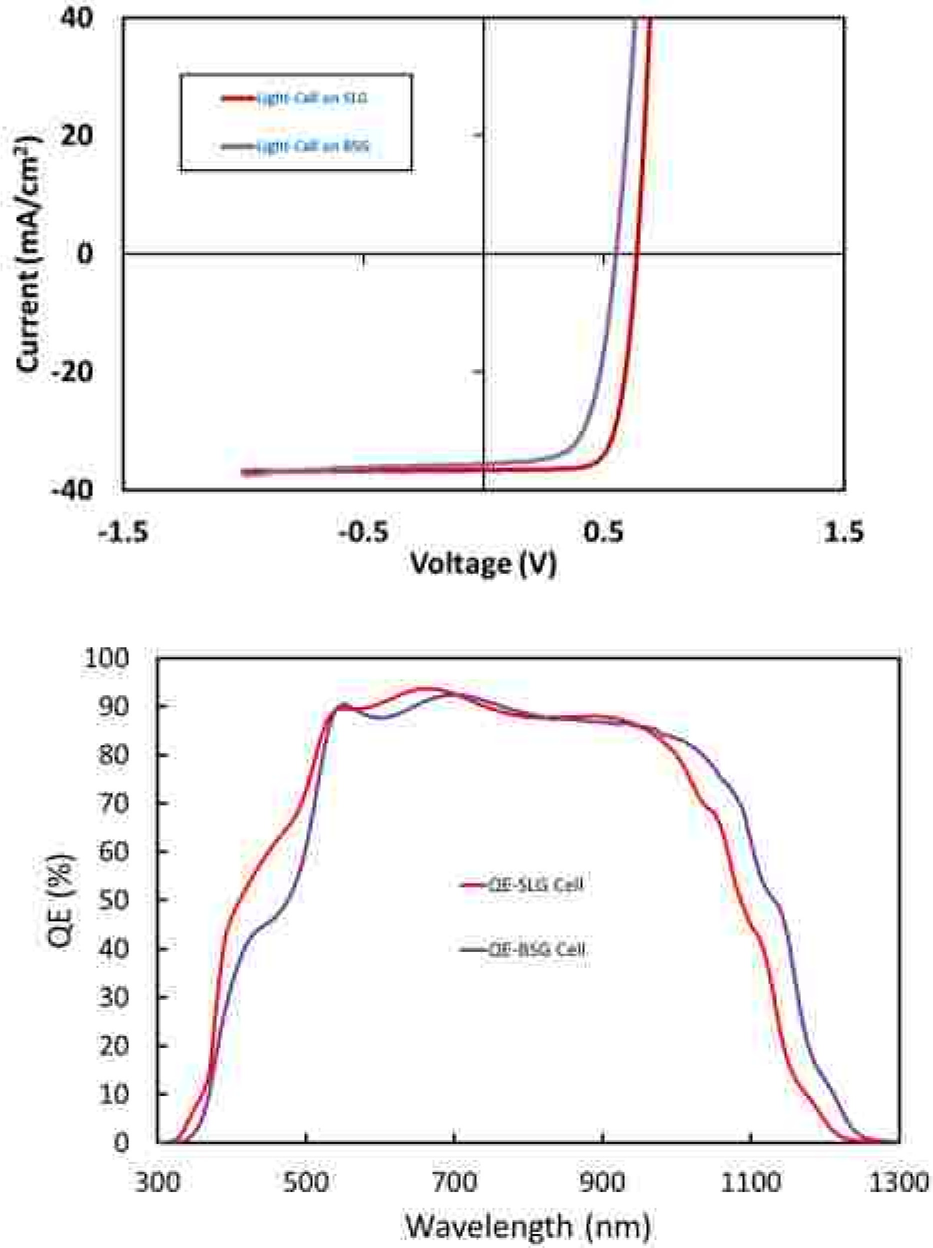

Figure 3.21 JV and QE plots of the devices fabricated on SLG and BSG substrates.

Table 3.6 Comparison of device parameters for solar cells fabricated on SLG and BSG substrates.

Sample ID	**η (%)**	**J_{SC} (mA/cm^2)**	**V_{OC} (V)**	**FF (%)**
CIGS on SLG	17.60	36.60	0.64	73.10
CIGS on BSG	12.44	35.60	0.55	63.60

3.6 Conclusions

Both in-situ and ex-situ Ellipsometry analysis were performed on molybdenum thin films deposited on five different substrates. RTSE analysis exhibits a Volmer-Weber type growth mechanism for all the films. Dielectric functions extracted from the ex-situ analysis show a Drude oscillator, typical of metals. Resistivity values were extracted from this oscillator and correlated with Hall Effect and 4-point probe measurements. It was found that substrates with sodium led to slightly less resistive films. At the same time, AFM images showed that the films were deposited conformally on the substrates, and that the roughness of the films was inversely related to the resistivity values. XRD analysis showed that all the Mo films deposited were preferentially oriented along the (110) direction with grains ranging from 4-5 nm, regardless of the substrates. This was correlated with SEM surface images. Na depth profiles, obtained by SIMS analysis, were then compared for Mo/CIGS structures deposited on SLG and BSG. A clear difference between the two was observed, with a much higher intensity of Na for the SLG substrates. Devices were then fabricated on both substrates and analyzed by J-V and QE measurements. Even though no change occurred for the current, a clear decrease in V_{OC} and FF was observed for the BSG substrate compared to the SLG substrate. Since the other analyses performed on both samples in terms of electrical and structural properties showed little difference, it is clear that the presence, or absence, of sodium is the determining factor for the device efficiency.

CHAPTER 4

EFFECT OF SUBSTRATE TEMPERATURE ON SPUTTERED MOLYBDENUM FILMS

4.1 Introduction and Motivation

Extensive research has been carried out by other researchers on the deposition of molybdenum thin films by direct current (dc) sputtering and the features of physical and optical properties of Mo films as a function of deposition pressure [56]. Several groups also reported the change in microstructure, defect analysis, electrical and optical properties as a function of substrate temperature; however, the chemical analysis of the films was not much studied [lin, rafaja, puja]. The high temperatures during deposition (usually greater than 450°C) cause Na to diffuse through the Mo and into the CIGS when soda lime glass substrates are used. Various diffusion models have been developed to study the effect of annealing temperature on the sodium diffusion process. However, the influence of substrate heating on sodium and other impurity diffusions, along with the characteristics of molybdenum films, have yet to be explored in depth. A well-defined diffusion model could be employed to determine the sufficient amount of sodium incorporation to obtain high efficiency CIGS solar cells. In addition, the effect of the presence of other alkali elements could be taken into consideration.

In this chapter, the study involves investigating the microstructural, electrical and chemical properties of Mo films deposited on SLG for different substrate temperatures (T_{SS}) while keeping the deposition pressure and power at fixed values. The Mo films' structure was examined by X-Ray Diffraction (XRD). Mo films were subsequently characterized using cross-sectional and plan-view scanning electron microscopy (SEM). Secondary ion mass spectroscopy (SIMS) analysis was also performed to obtain the Na depth profile in the Mo films. X-ray Photoelectron Spectroscopy (XPS) analyses on these films were also carried out. Both theoretical and numerical models were used for simulating the grain boundary diffusion.

4.2 Deposition Process for Molybdenum Films

Molybdenum thin films were fabricated onto soda-lime glass (SLG) substrates using direct current (dc) magnetron sputtering. The depositions were carried out in high purity (99.999%) argon ambient using a 2 inch diameter Mo sputtering target. The required argon pressure for sputtering was maintained at 10 mTorr. The duration of deposition was kept constant. The substrate temperature was kept constant during deposition, and was either room temperature (RT), 50°C, 100°C, 150°C, 200°C or 250°C. The dc power was kept constant at 150 W.

4.3 Characterization of Molybdenum Films as a Function of Substrate Temperature

4.3.1. Structural Characterizations

Figure 4.1 displays the X-ray diffraction (XRD) spectra for Mo thin films deposited at different substrate temperatures T_{SS} (°C). One can see that only the (110) and the (220) peaks of the molybdenum phase appear, indicating the films have a preferred orientation along the (110) direction. One can also observe that the full width at half maximum (FWHM) of the peak decreases with an increase in temperature (Figure 4.2). Grain size follows an increment in values as shown in the plot when calculated using the Scherrer's equation described in Chapter 2. The increase in peak intensity with T_{SS} indicates an increase in crystalline phase, as all the films have similar thickness. Another feature of these films is a slight shift of the peak for each film, which might indicate the variation in the average lattice spacing [57] when substrate temperature varies or a relaxation in the film stress as illustrated in Figure 4.3.

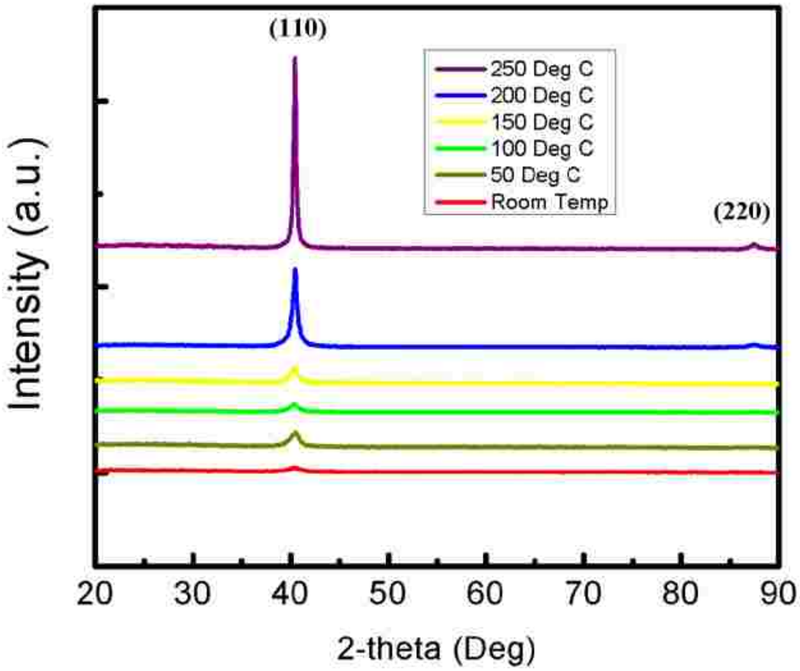

Figure 4.1: XRD spectra of the various Mo films on SLG as a function of substrate temperature.

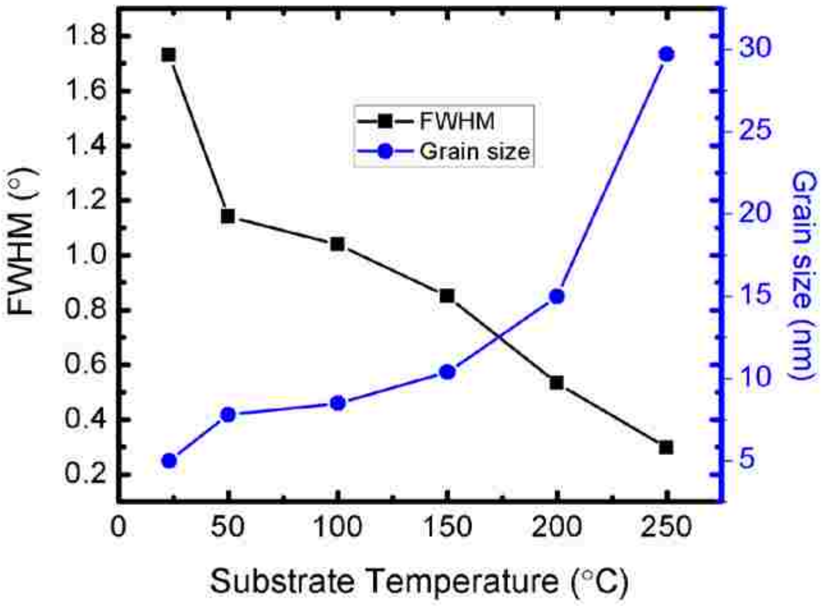

Figure 4.2: Relationship between FWHM and grain size of the various Mo films on SLG as a function of substrate temperature.

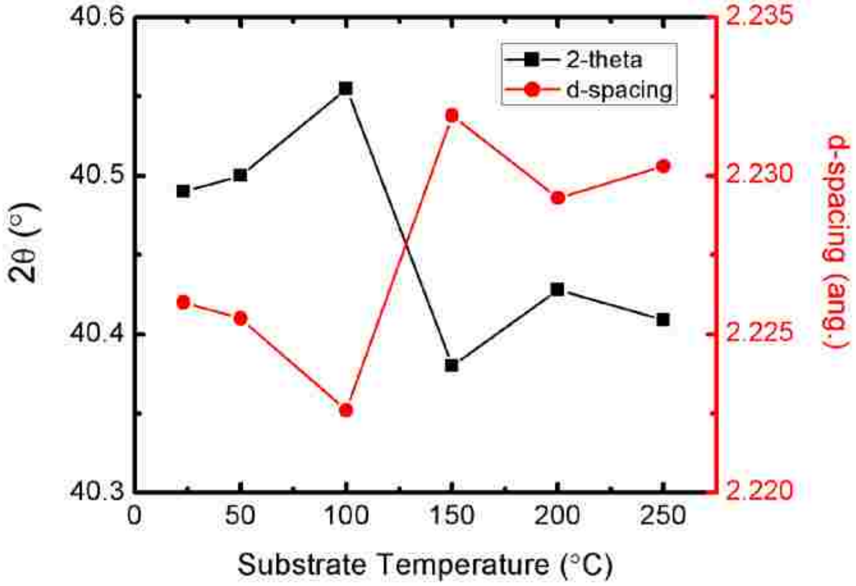

Figure 4.3: Effect of substrate temperature on 2-theta and d-spacing values for the Mo films deposited on SLG.

The plan-view and cross-sectional SEM images of all as-deposited Mo films are presented in Figure 4.4. All films show a columnar grain structure.

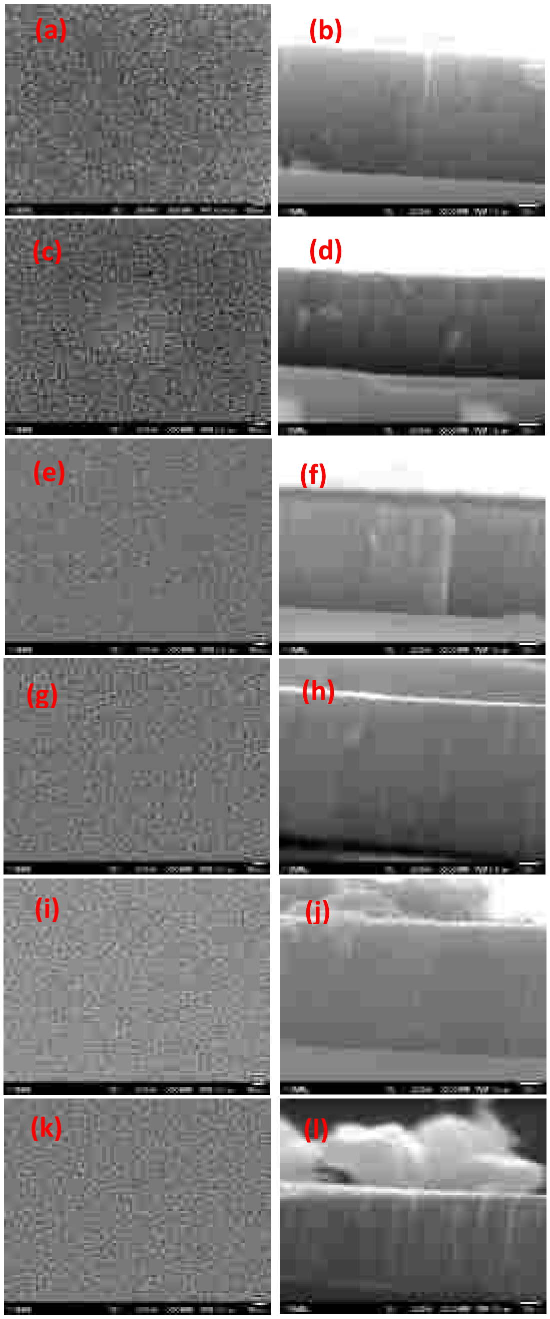

Figure 4.4: Plan-view (left) and cross-sectional (right) SEM images of the various Mo films on SLG as a function of T_{SS}: (a) and (b): RT; (c) and (d): 50 °C; (e) and (f): 100 °C; (g) and (h): 150 °C; (i) and (j): 200 °C; (k) and (l): 250 °C.

No specific change in grain structure can be observed as T_{SS} increases based on cross-section SEM, which is expected from the XRD results as the grain structure is below the resolution of the SEM. A TEM imaging would have been better for obtaining grain structure and also to differentiate from sample to sample with extremely high resolution. However, there is a clear change in surface morphology as T_{SS} increases, specifically above 150 °C, with larger grain features observed for higher T_{SS}.

To correlate the changes in surface features, AFM images of molybdenum films deposited at various T_{SS} were taken (Figure 4.5). The RMS roughness values obtained reveal that the films roughness decreases slightly from RT to 100°C, then increases afterwards, with the highest roughness at 200°C (Figure 4.6). This is in good correlation with the surface SEM images observed previously.

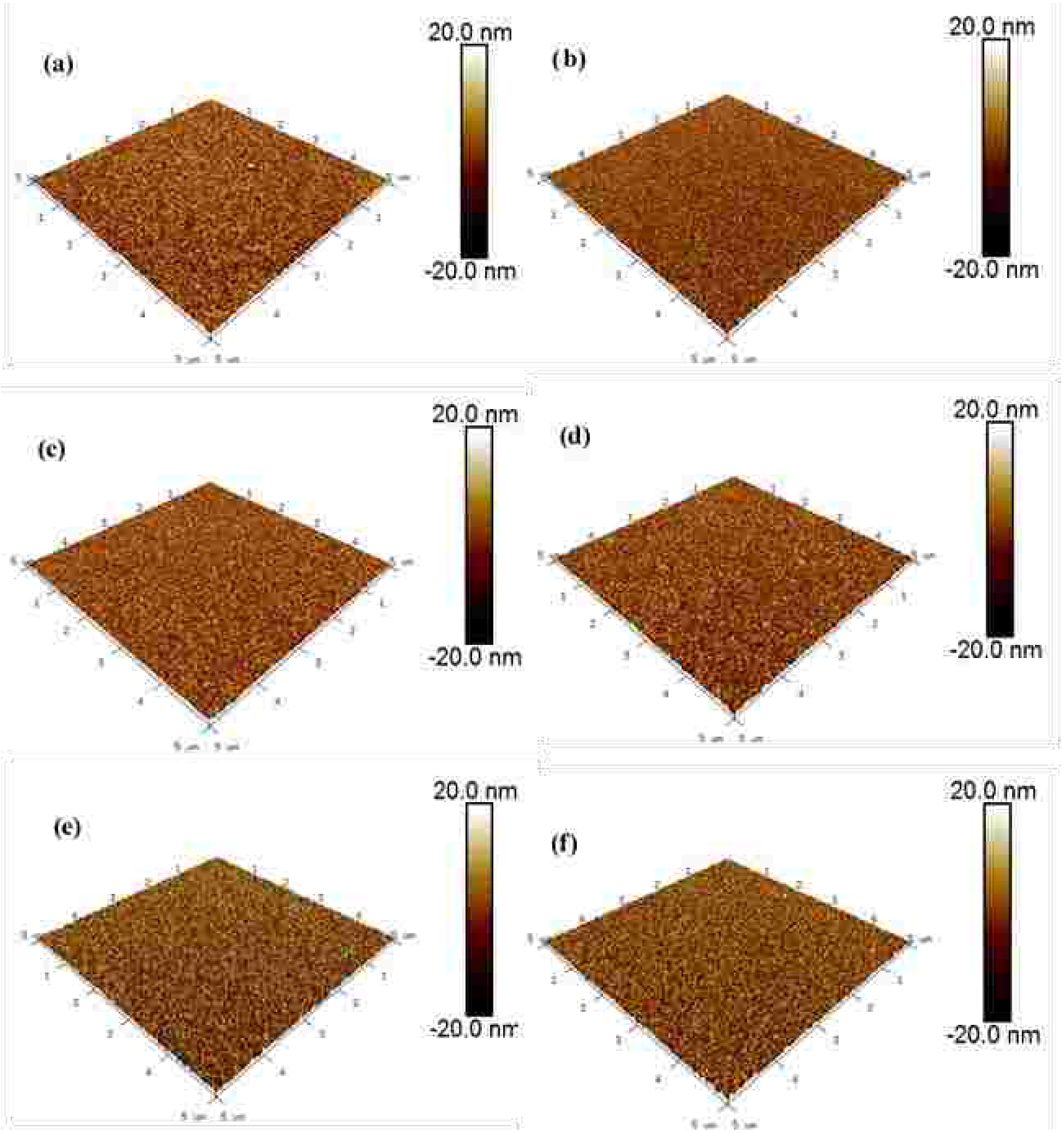

Figure 4.5: AFM images of the various Mo films on SLG as a function of T_{SS}: (a) RT; (b) 50°C; (c) 100°C; (d) 150°C; (e) 200°C; and (f) 250°C.

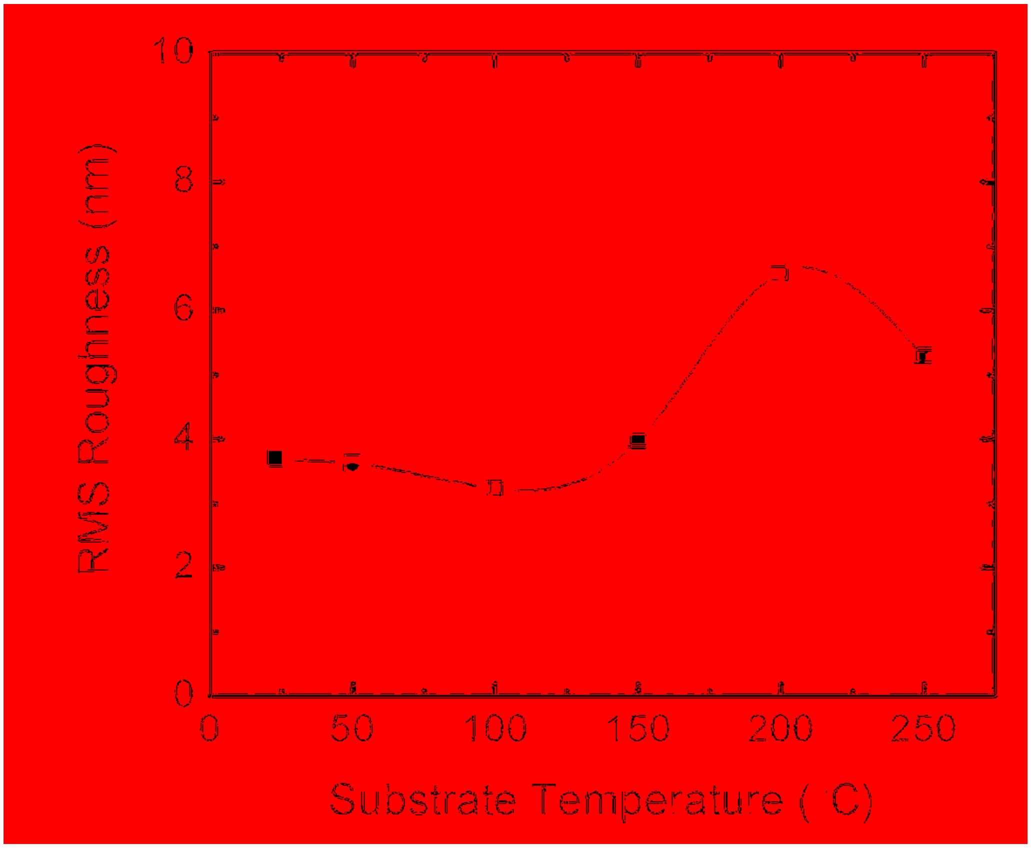

Figure 4.6: RMS roughness of various Mo films on SLG as a function of T_{SS}.

4.3.2. Electrical Characterizations

Hall Effect measurements were performed on the Mo films deposited at various T_{SS}. Both mobility and bulk concentration are presented in Figure 4.7 and 4.8 respectively with box plots. Different values for each T_{SS} were obtained by changing the measurement parameters to collect more data points and assure the measurement accuracy. If we look at the mean values of the measurements, the samples at 100°C have the lowest mobility but highest bulk concentration, and the samples at 50°C have the highest mobility but lowest bulk concentration, with the other samples having almost similar values. Resistivity values are presented in Figure 4.9. Calculated resistivity values from sheet resistance were compared with the measured resistivity values obtained from Hall Effect measurements. To calculate the resistivity, thicknesses obtained from cross-sectional SEM were used. Both type of resistivity and the sheet resistance values are in agreement and have the highest values for the room temperature sample. These values decrease as the T_{SS} increases and varies within a small range of values.

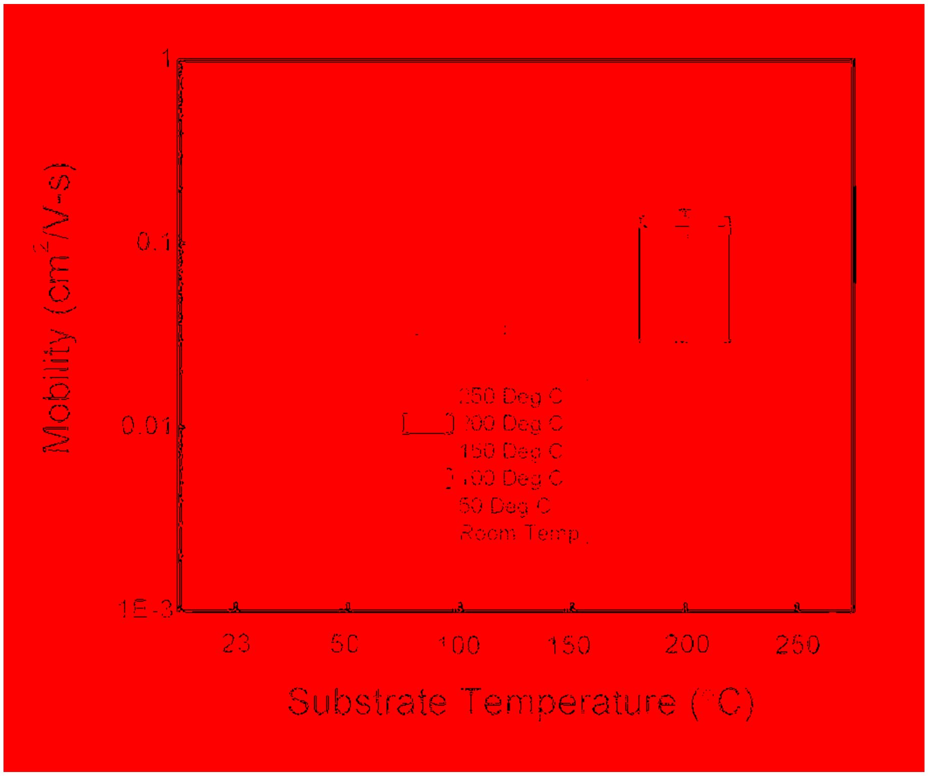

Figure 4.7: Mobility values obtained with Hall Effect measurement for various Mo films on SLG as a function of T_{SS}.

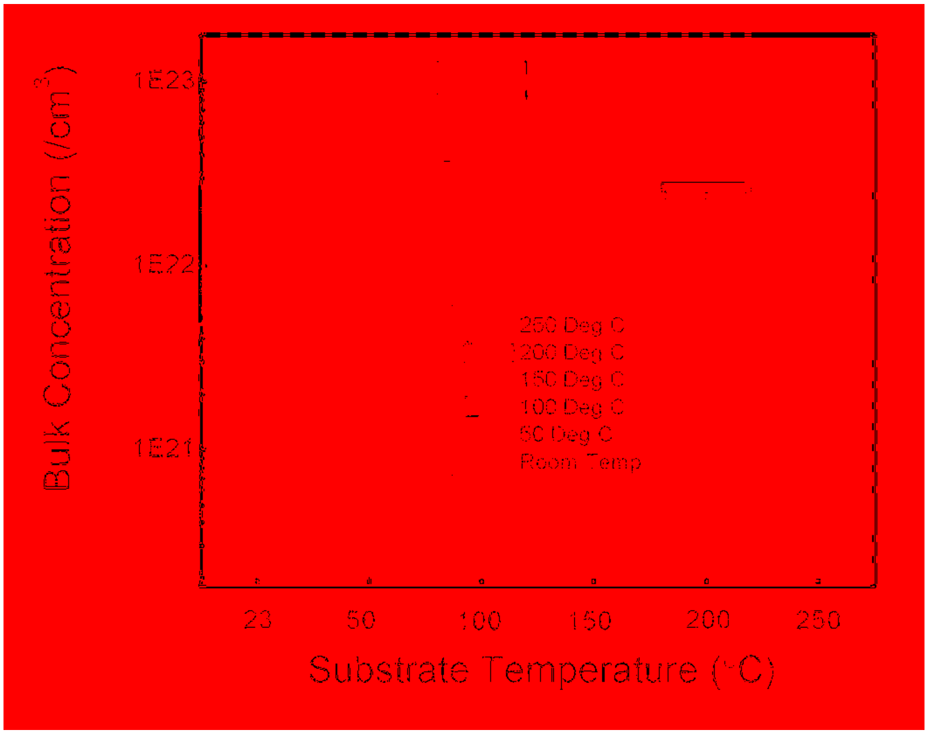

Figure 4.8: Bulk concentration values obtained with Hall Effect measurement for various Mo films on SLG as a function of T_{SS}.

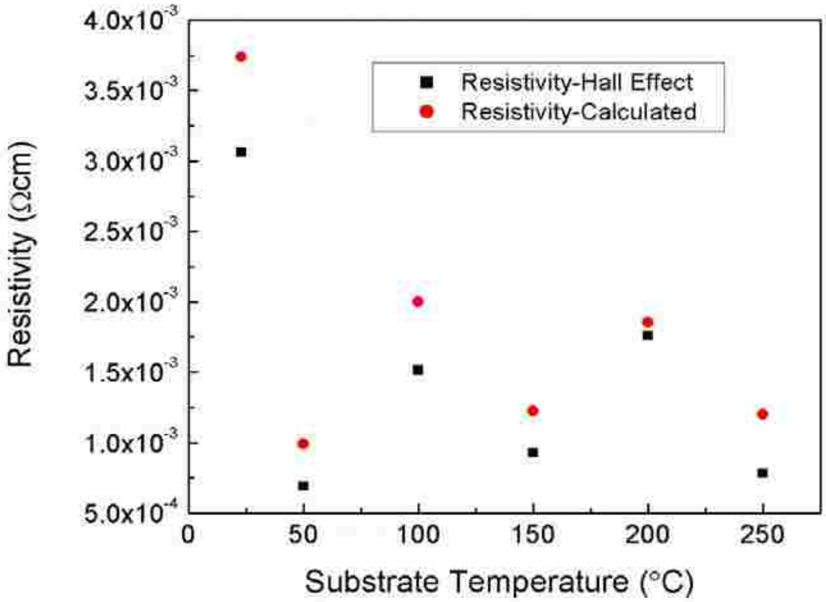

Figure 4.9: Resistivity values obtained with Hall Effect measurement and calculated from sheet resistance values for various Mo films on SLG as a function of T_{SS}.

4.3.3. Chemical Characterizations

Before starting the chemical analysis of the films, Residual Gas Analyzer (RGA) data are represented in Figures 4.10 and 4.11. RGA plots show the presence of the species H_2, N, N_2, O, O_2, C, CO_2^{++}, CO_2 H, HO^+, H_2O, Ar^{++}, Ar and C_2H_5 in terms of partial pressure in the sputtering chamber without and with 1 SCCM Ar flow. It is important to note that no deposition was performed while collecting the RGA data. There is an increase in the Ar peaks as expected when Ar gas was injected inside the chamber. All these species were present in the chamber even after the chamber was baked at 100°C, as shown in Figure 4.11, with a slight decrease in partial pressure for all of them after baking.

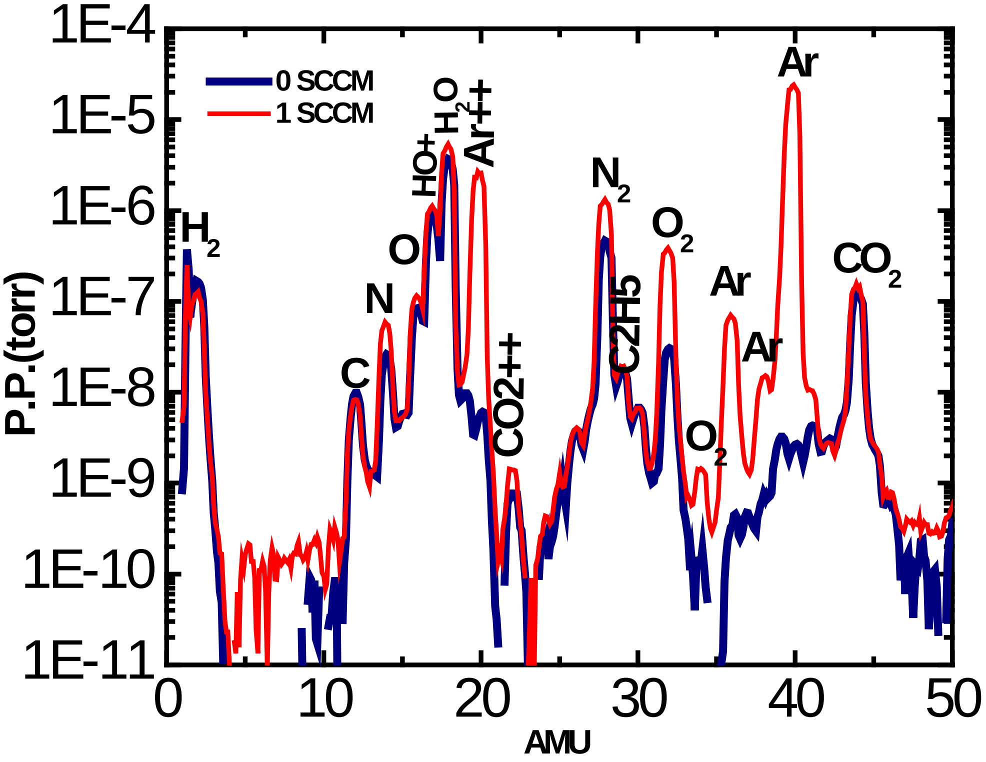

Figure 4.10: RGA data with and without Ar flow in the sputtering chamber with no Molybdenum deposition.

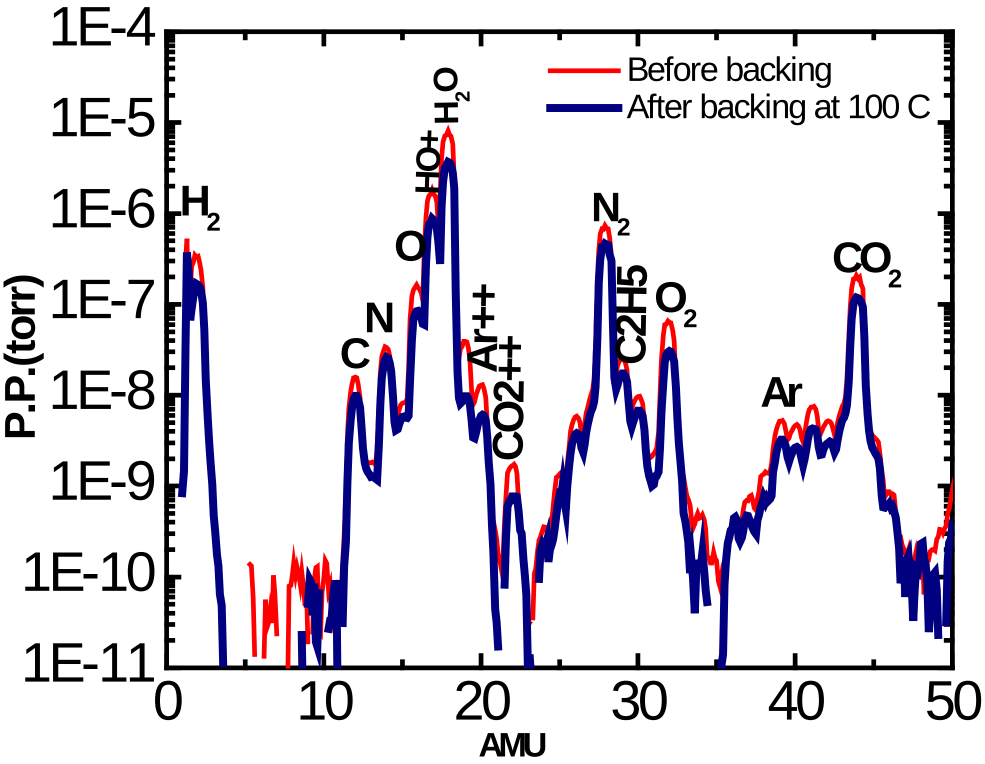

Figure 4.11: RGA data without Ar flow in the sputtering chamber before and after baking the chamber at 100°C with no Molybdenum deposition.

SIMS depth profiles were used to characterize all the elements concentration as a function of substrate temperature. Sputter time for all the SIMS depth profile discussed here has been normalized. One can observe that the sodium level increases when T_{SS} is higher than room temperature, reaches a maximum at T_{SS} = 100°C and then starts to decrease as the T_{SS} is increased further (Figure 4.12). One can also observe a sharp edge at both the surface and the glass interface. However, the accumulation of sodium at the surface of the molybdenum does not seem to be that different for all temperatures.

An association between sodium and oxygen depth profile (Figure 4.13) was observed, in the sense that the oxygen concentration evolves the same way as the sodium one. The potassium (K) depth profile shows (Figure 4.14) similar features except for the film deposited at 250°C, which is similar to the run at 200°C instead of being lower. The influence of T_{SS} on the other alkali elements such as Mg and Ca follows different features (Figures 4.15 and 4.16 respectively), with a decrease in concentration as T_{SS} increases. Figure 4.17 shows the variation in the intensity level for all five elements at the glass Mo interface. It should be noted that SIMS analysis is poor at absolute quantification and relative sensitivity factor plays an important role when analyzing the data.

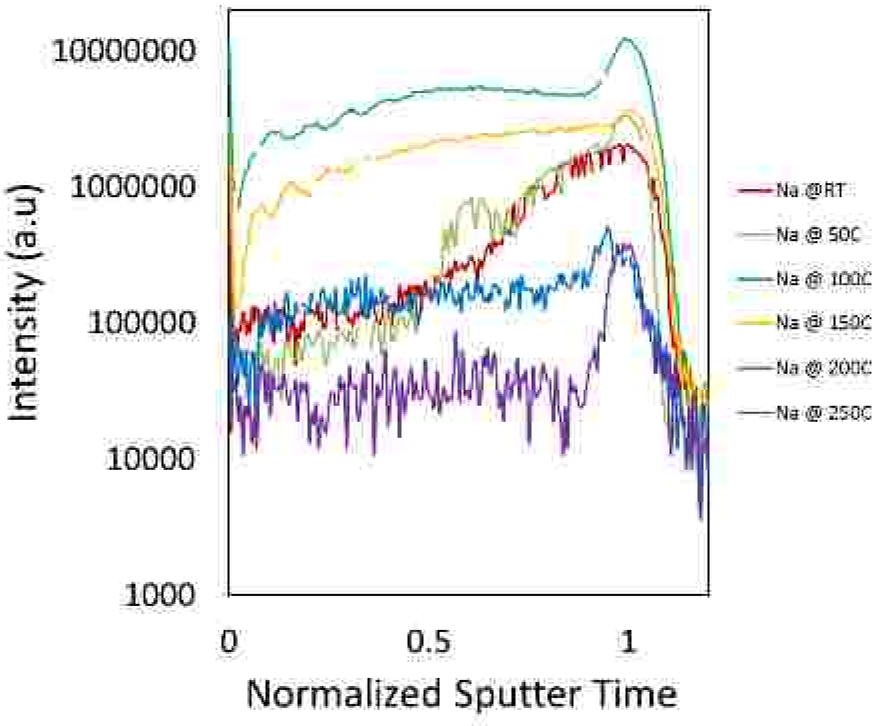

Figure 4.12: SIMS depth profile of Na as a function of substrate temperature.

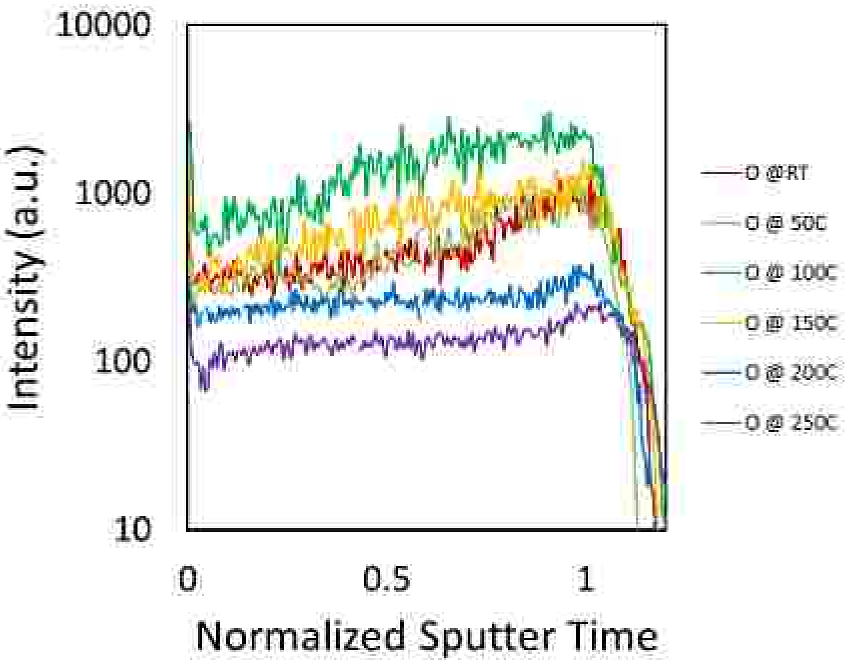

Figure 4.13: SIMS depth profile of O as a function of substrate temperature.

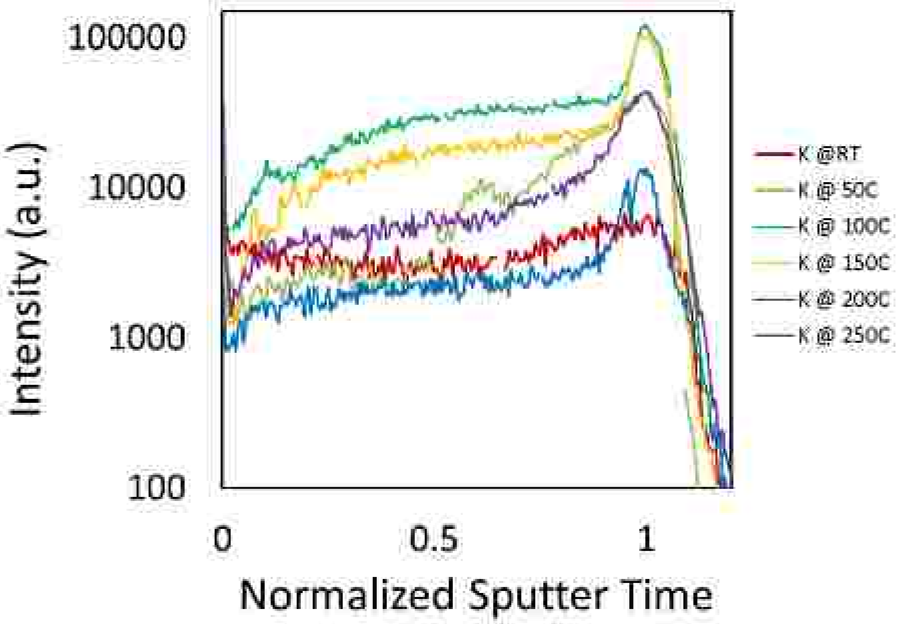

Figure 4.14: SIMS depth profile of K as a function of substrate temperature.

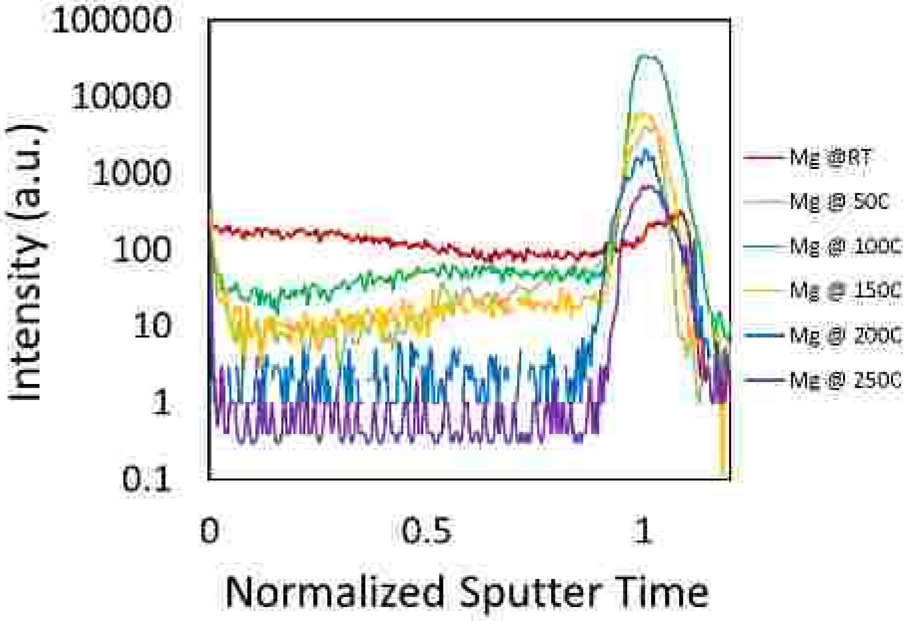

Figure 4.15: SIMS depth profile of Mg as a function of substrate temperature.

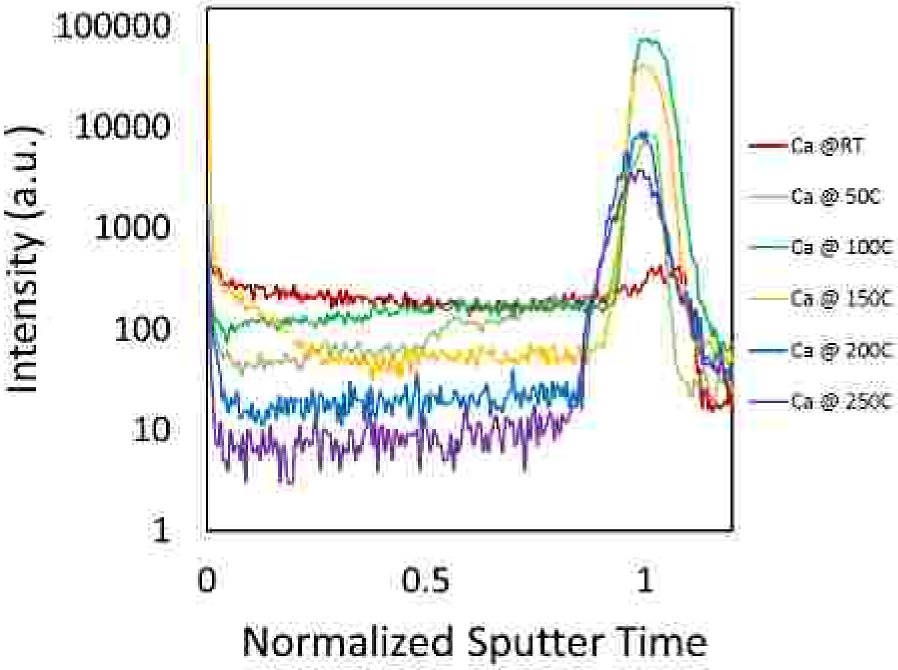

Figure 4.16: SIMS depth profile of Ca as a function of substrate temperature.

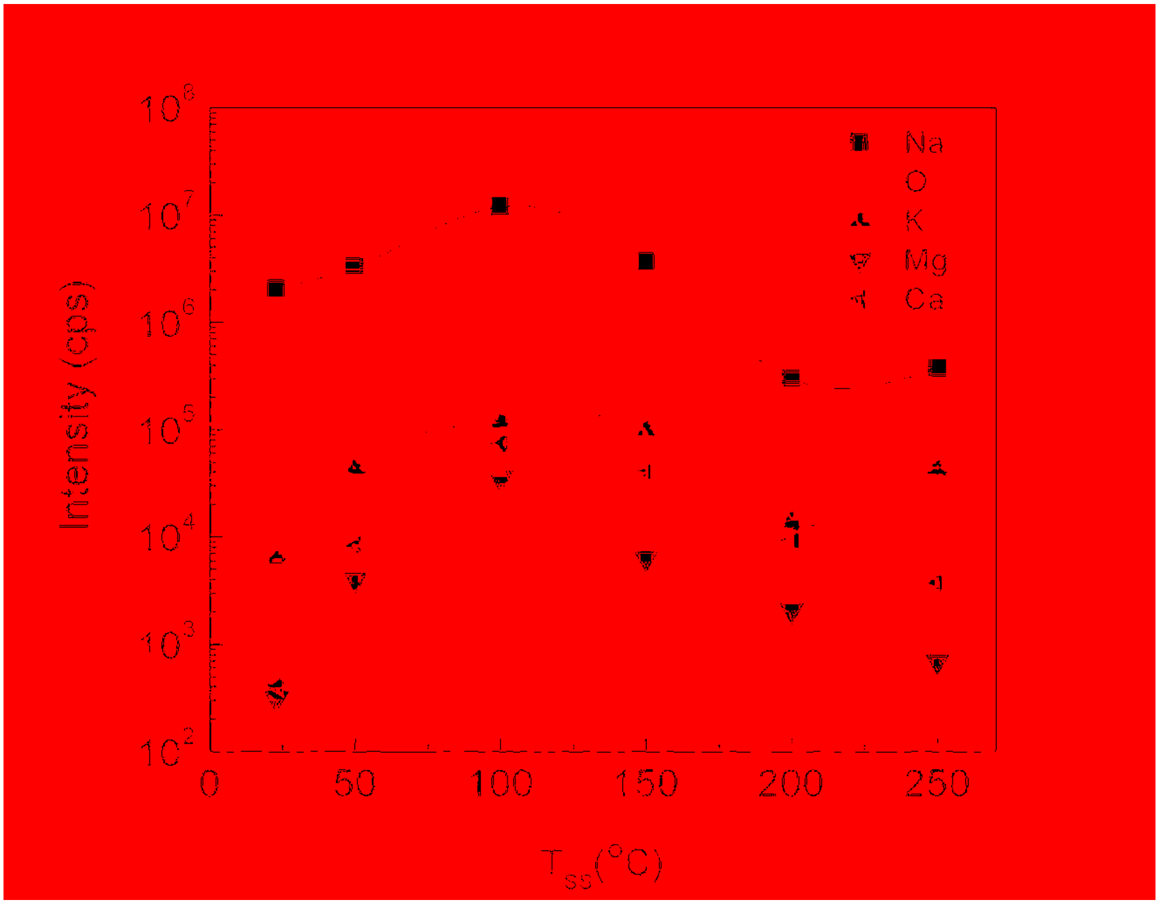

Figure 4.17: Intensity of five impurity elements at the SLG/Mo interface as a function of substrate temperature.

One can see from Figure 4.17 that all the elements follow roughly a similar trend, with an increase in concentration up to 100°C, followed by a decrease. To further understand the chemical states of the samples, XPS analyses were performed on these films to understand the oxidation states. XPS is usually considered as a surface characterization technique; however, with the aid of Ar ion etching, the structure and compositions below the surface layers or bulk can be studied. XPS high resolution scans were performed on the surface (Figure 4.18) and after sputtering the surface of the molybdenum films (Figure 4.19) on the six samples with different substrate temperatures T_{SS}. The surface before sputtering was heavily oxidized, showing a mix of oxide and metallic peaks. A carbon peak was also observed, but not enough sodium or potassium was present to be seen in any spectra (contrarily to SIMS, which can detect elements down to ppb, XPS can only detect atomic percentage of any element). Once sputtering was done, the oxygen signal decreased significantly (from around 70-80 at% to 15-30 at%) as seen from Figure 4.20.

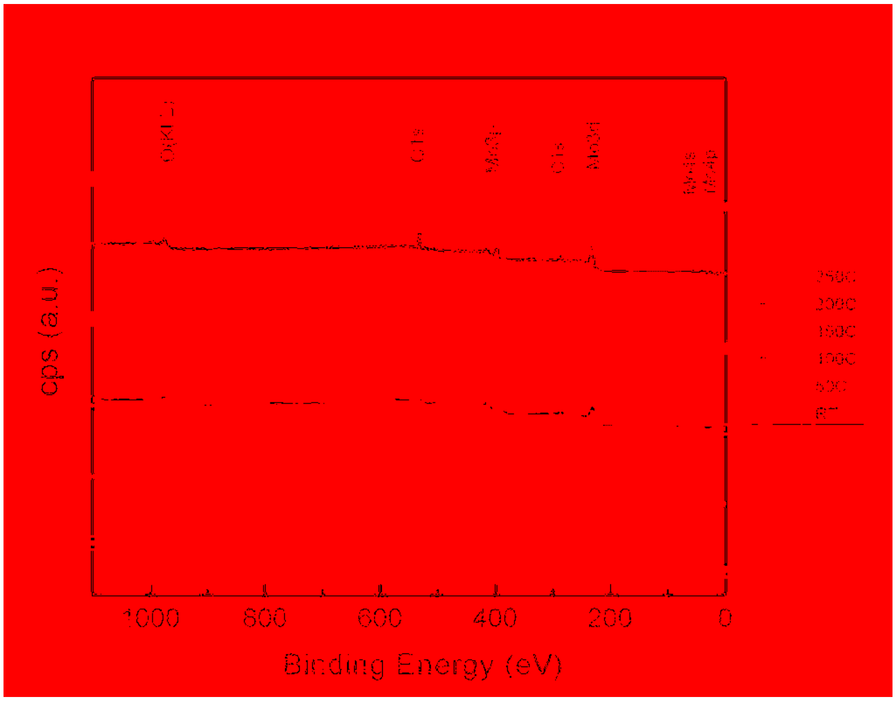

Figure 4.18: High-resolution XPS surface survey scans of the Mo films deposited by DC magnetron sputtering at different substrate temperature.

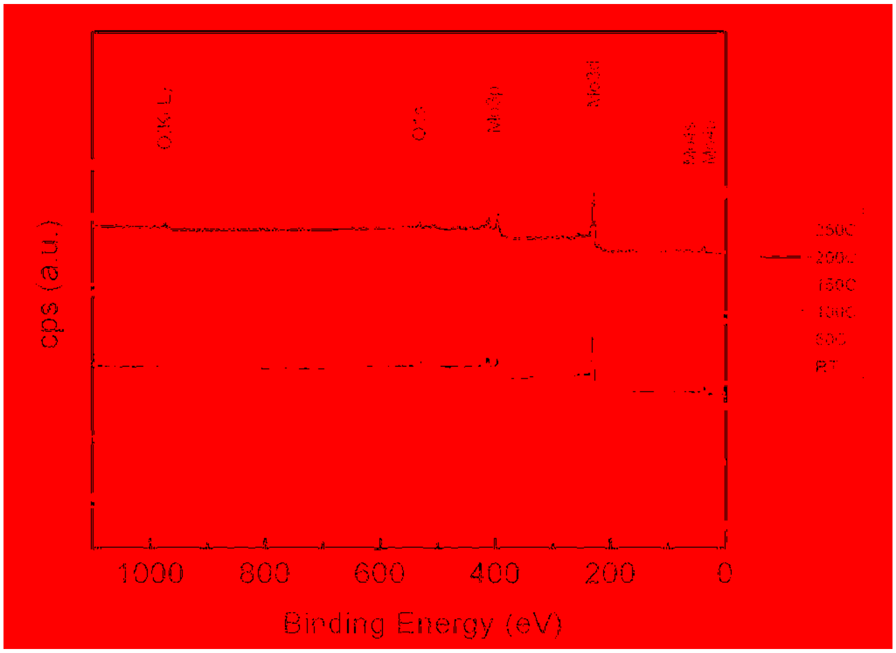

Figure 4.19: High-resolution XPS survey scans after sputtering the surface of the Mo films deposited by DC magnetron sputtering at different substrate temperatures.

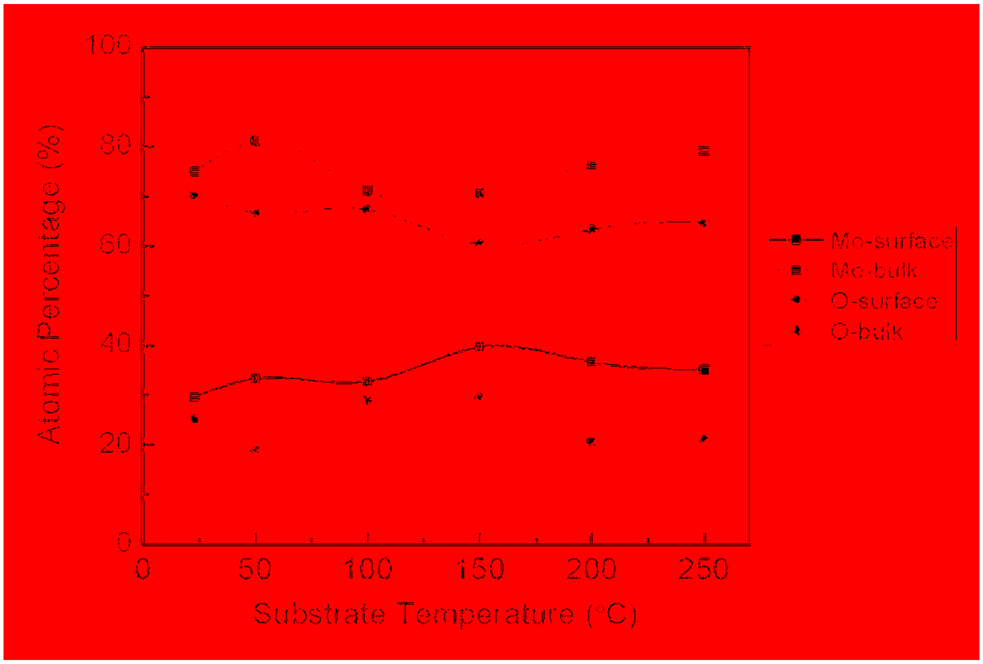

Figure 4.20: Atomic percentages of molybdenum and oxygen in the surface and bulk at different substrate temperatures.

As shown in Figure 4.20, the highest surface oxidation is for room temperature deposition. There is a decrease in surface oxygen level for T_{SS}=50°C followed by an increase for T_{SS}=100°C. The lowest oxidization occurs for the T_{SS} of 150°C. The Mo atomic percentages show an opposite trend compared to oxygen within the given range for T_{SS}.

Figure 4.21 shows high resolution XPS spectra of the O 1*s* peak for all $T_{SS.}$ Deconvoluted plots for the O 1*s* region are shown in Figure 4.22 for the room temperature deposition. No substantial difference could be distinguished due to the change in substrate temperature. The deconvolution process highlighted the presence of O and O-Mo^{4+}species.

After sputtering, the samples consist mostly of clean Mo with a small amount of O signal left (Figure 4.20). The binding energies of Mo $3d_{5/2}$ and Mo $3d_{3/2}$ are 229.3 and 232.5 eV, respectively, which can be assigned to Mo^{4+} extracted after the deconvolution process (Figure 4.24).

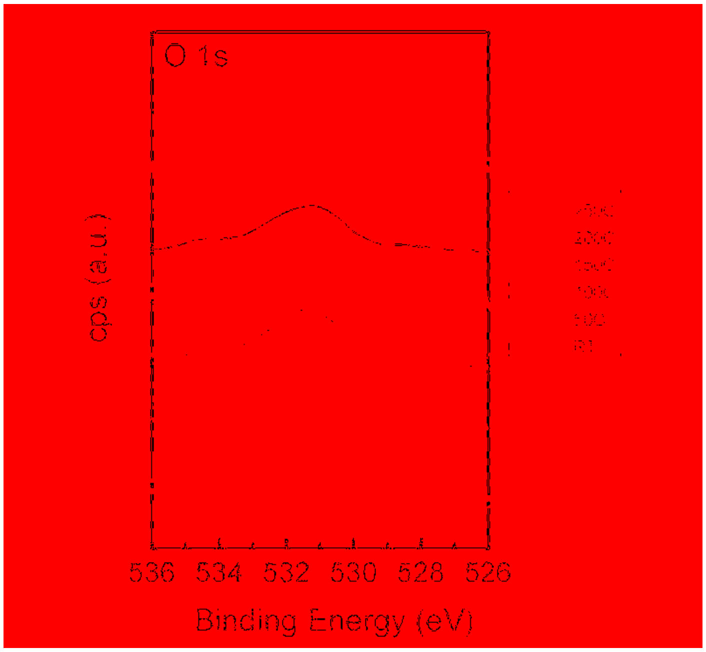

Figure 4.21: High resolution XPS spectra of O 1*s* region for the Mo films in the bulk.

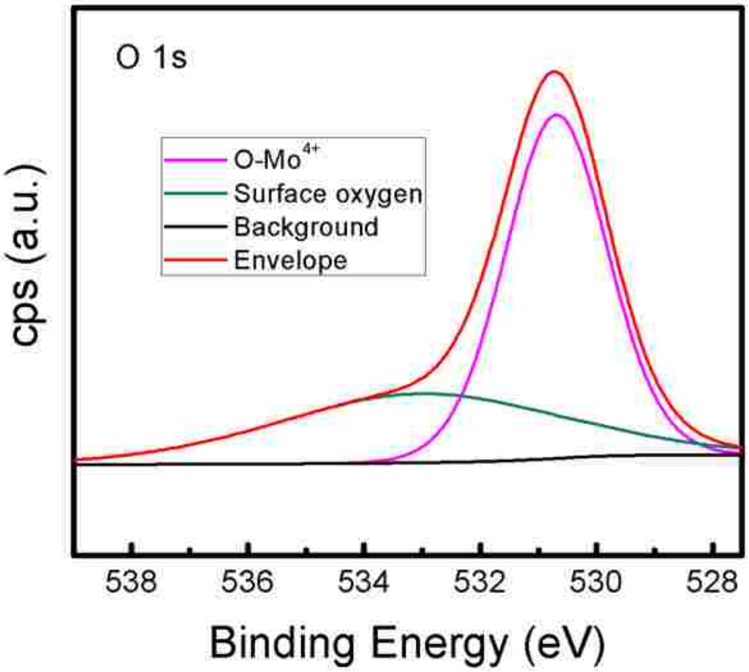

Figure 4.22: Deconvoluted XPS spectra of O 1*s* region for the Mo films in the bulk (T_{SS} =RT).

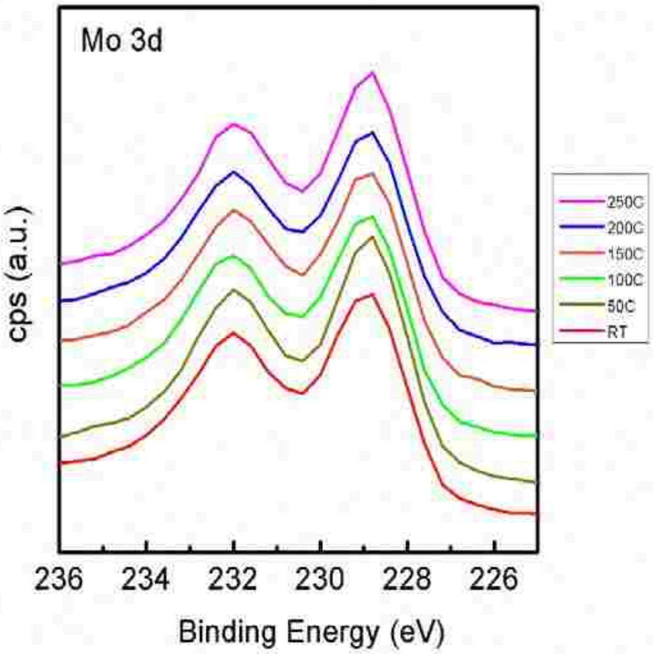

Figure 4.23: High resolution XPS spectra of the Mo 3*d* region for the Mo films in the bulk. The binding energies of Mo $3d_{5/2}$ and Mo $3d_{3/2}$ are 229.3 and 232.5 eV, respectively, which can be assigned to Mo^{4+}.

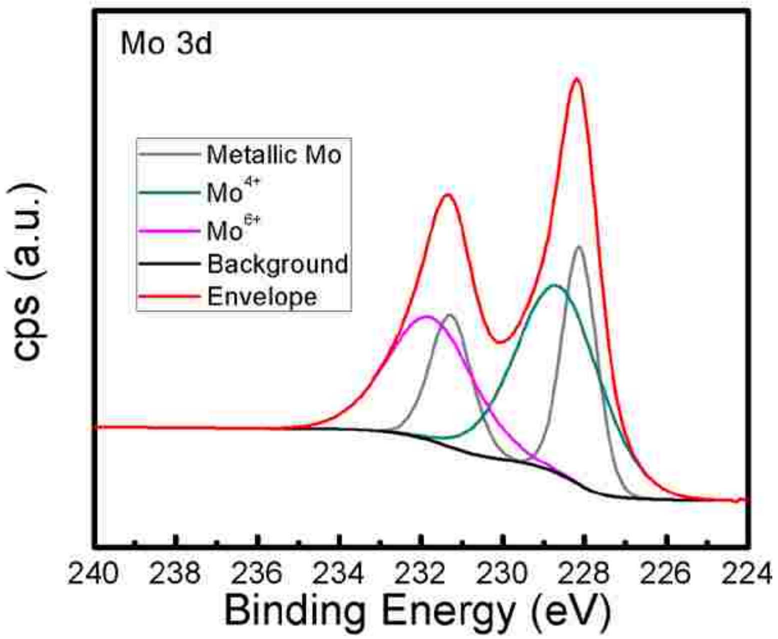

Figure 4.24: Deconvoluted XPS spectra of Mo 3*d* region for the Mo films in the bulk (T_{SS} =RT).

Table 4.1 summarizes the peak area and FWHM values for the Mo $3d_{5/2}$ and Mo $3d_{3/2}$ peaks for different T_{SS}. For the Mo $3d_{3/2}$ peak, the binding energy is within the range of 228.1 ± 0.03 eV and for the Mo $3d_{5/2}$ peak it is 231.25 ± 0.03 eV. The peak area and FWHM values did not show a specific trend as a function of T_{SS}.

Table 4.1 Results of peak fitting for the Mo 3$d_{5/2}$ (228.1 ± 0.03 eV) and 3$d_{3/2}$ (231.25 ± 0.03 eV) peaks after argon ion etching.

T_{SS} (°C)	Position (eV)	Peak Area (a.u.)	FWHM (eV)	Position (eV)	Peak Area (a.u.)	FWHM (eV)
23	228.12	1659	0.989	231.27	1107	1.18
50	228.07	1957	0.929	231.22	1304	1.41
100	228.13	1893	0.960	231.28	1262	1.13
150	228.10	1673	0.899	231.25	1115	1.09
200	228.09	1454	0.933	231.24	969	1.11
250	228.07	1843	0.919	231.22	1229	1.12

Table 4.2 summarizes the peak area and FWHM values for the O 1S peaks for different T_{SS}. The binding energy is within the range of 530.64 ± 0.7 eV. The peak area and FWHM values for the range of T_{SS} studied did not show a specific trend, similarly to the Mo 3*d* peak analysis.

Table 4.2 Results of peak fitting for the O 1*s* peak after argon ion etching.

T_{SS} (°C)	Position (eV)	Peak Area (a.u.)	FWHM (eV)
23	530.69	619	2.073
50	530.57	372	1.855
100	530.62	528	1.901
150	530.71	429	1.817
200	530.69	544	2.229
250	530.62	329	1.798

Figures 4.25 and 4.26 show high-resolution spectra for the Mo 3*p* and Mo 4*p* peaks. As expected, very little influence in their characteristics was observed as T_{SS} changes.

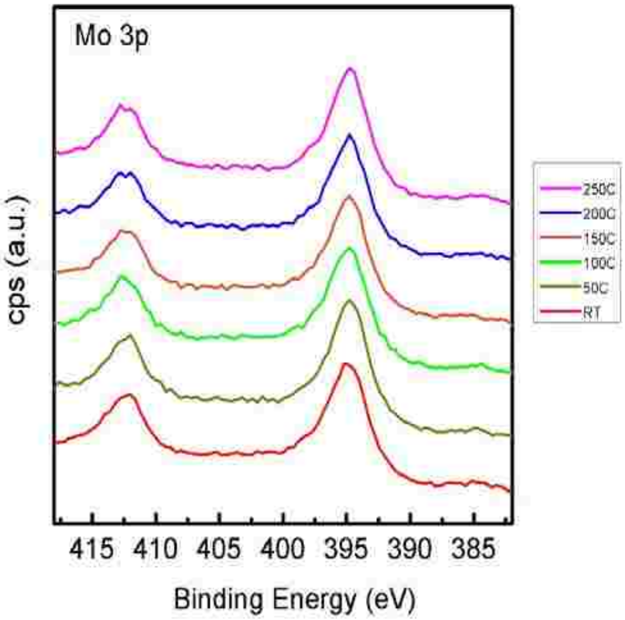

Figure 4.25: High resolution XPS spectra of the Mo 3*p* peak for the Mo films in the bulk.

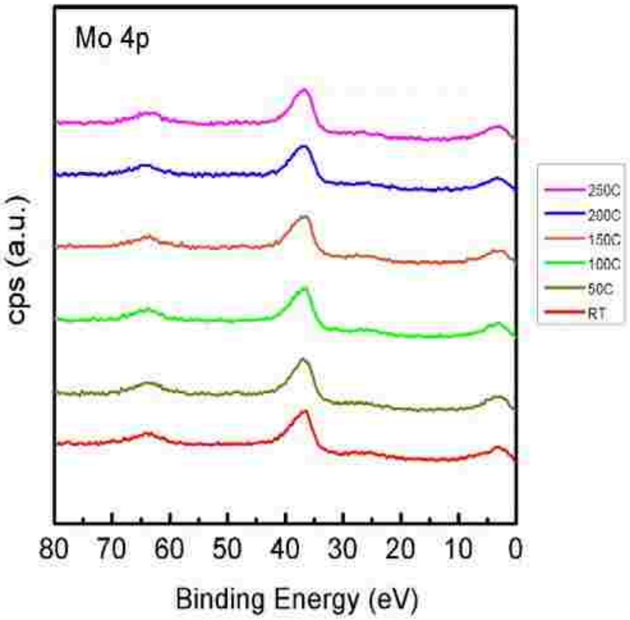

Figure 4.26: High resolution XPS spectra of the Mo 4*p* peak for the Mo films in the bulk.

Even though we represented the detail XPS analysis for the bulk of the Mo film, it is interesting to look at the high resolution spectra for the surface. Figure 4.27 shows the Mo *3d* peaks at the surface and Figure 4.28 show the comparison between the Mo *3d* peaks for the bulk and surface measurements. As observed in Figure 4.20, the quality of the Mo signal is better in the bulk compared to the surface, as the surface oxygen is removed.

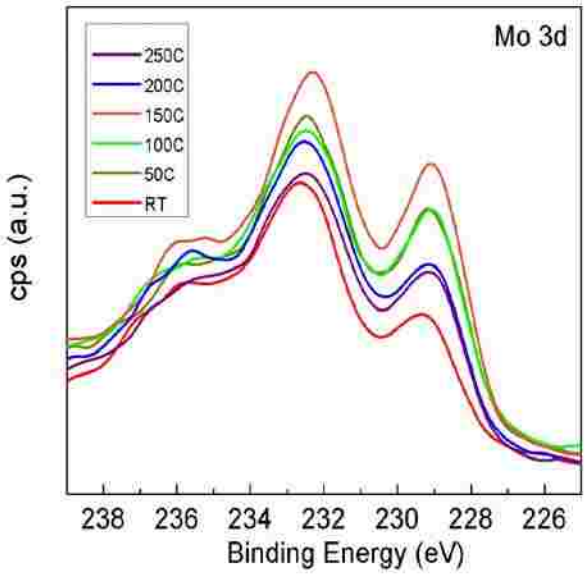

Figure 4.27: High resolution XPS spectra of the Mo 3*d* peak for the Mo films at the surface.

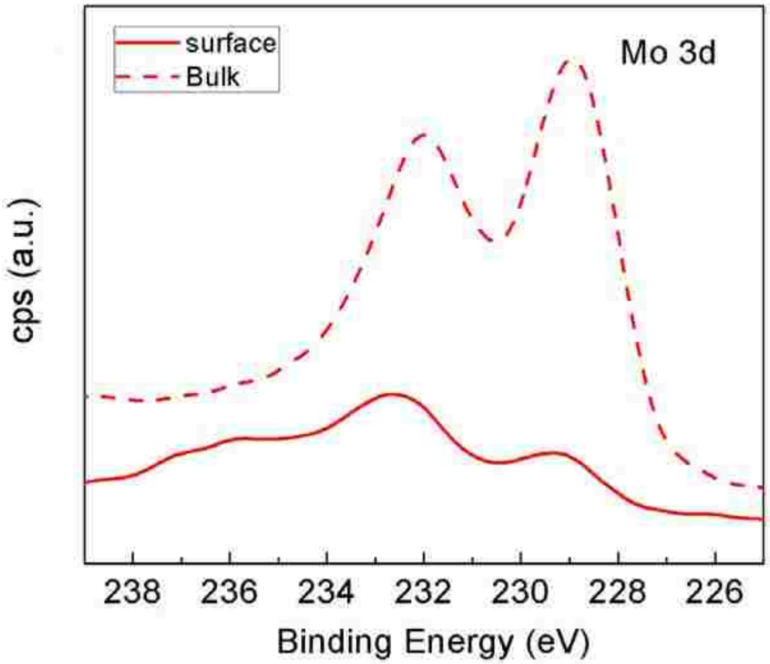

Figure 4.28: High resolution XPS spectra of the Mo 3*d* peak for the Mo films at the surface and in the bulk for room temperature deposition.

4.4 Modeling of the Effect of Substrate Temperature on Impurities Diffusion through Molybdenum Films

4.4.1 Basic Discussion on Diffusion Mechanism

In general, measurement of the diffusion coefficient in solids encompasses fitting experimental data to diffusion models that are established based on Fick’s laws of diffusion. In 1855, Fick first recognized the basic connection between two processes, i.e. diffusion and heat transfer by conduction, suggesting new laws of diffusion analogous to the theory of heat conductivity.

Diffusive flux (J) can be described by Fick’s first law where, in an isotropic material, the rate of transfer of the diffusant across a unit area of a section normal to the diffusion direction is proportional to the concentration gradient in the direction of diffusion, which is expressed by the following:

$$J = -D\Delta C \tag{4.1}$$

where *J* is the diffusive flux, *C* is the concentration and *D* is the diffusion coefficient. It should be noted that *D* often relies on the host materials.

For determining *D* experimentally, it is not convenient to use equation (4.1) as it requires the measurement of the steady-state concentration gradient and steady state flux. A more suitable form of equation (4.1) can be effortlessly obtained if the material balance across a volume of elements of the system is taken into account. This form of Fick's law relates the concentration gradient to the rate of change of concentration at a specified position by the following expression:

$$\frac{\partial c}{\partial t} = -\nabla\, \mathbf{J} \tag{4.2}$$

where *t* is the time. This equation can be reduced, assuming D is position independent and substituted it from equations (4.1) and (4.2), to Fick's second law:

$$\frac{\partial c}{\partial t} = D\boldsymbol{\nabla}^{\mathbf{2}}\boldsymbol{C} \tag{4.3}$$

where $\boldsymbol{\nabla}^{\mathbf{2}}$ is the Laplacian operator defined as:

$$\nabla^2 = \frac{\partial^2}{\partial x^2} + \frac{\partial^2}{\partial y^2} + \frac{\partial^2}{\partial z^2}$$

A semi-infinite slab is a perfect system that is applicable to large enough samples where the edge effect can be discounted and in addition where the films are much thicker than the length of diffusion [forest 66]. The solution for equation (4.3) for the system mentioned above is:

$$C = C_0 erfc\left(\frac{x}{2\sqrt{Dt}}\right) \tag{4.4}$$

where *erfc* is the complementary error function, C_0 is the source concentration, and x is the depth. A diffusion coefficient can be approximated from the experimental data by fitting equation (4.4) to the depth profile obtained from the measurement. Equation (4.3) must be solved using the applicable constraints in the cases where assumptions of a constant source or semi-infinite slab are not applicable. For systems that are too complex for an analytical solution, numerical methods should be used instead.

For the estimation of the diffusion coefficient through the developed model, either concentration data through depth profiling techniques (SIMS or Auger analysis) or surface accumulation data (for example, data obtained from XPS or Auger or any other surface analysis method) can be used. Depth profiling techniques include inducing diffusion for a certain period of time and subsequently measuring concentration as a function of depth. In this work, depth profiles obtained using secondary ion mass spectroscopy (SIMS) have been used.

It is impractical to obtain depth profiles for the cases where diffusion occurs through a very thin film with low concentration and surface accumulation methods are the best choice since diffusion must take place through the entire film. This method includes allowing the diffusing element to penetrate the entire sample and accumulate at the surface. The surface concentration of the accumulating elements can be measured as a function of time, which can be fitted to the diffusion models. Diffusion at the surface creates additional complexity in the model since both diffusion through the film and diffusion on the accumulating surface must be taken into consideration. Frequently surface diffusion takes place much faster than bulk diffusion, which helps in simplifying the analysis [59].

The diffusion mechanism involved in a crystalline solid is considerably different than that via gas or liquid because of the constraints imposed by the crystalline lattice. The vacancy mechanism is accounted to be one of the most prevailing diffusion mechanisms in solids. If the diffusing atoms are significantly smaller than host material atoms, diffusion can also take place by interstitial hops between lattice sites [58, 59]. Both the vacancy and interstitial mechanisms include a transition state where the diffusing atom is between sites as depicted in Figure 4.29 (top), and there is a corresponding activation energy for hopping between sites which is shown in Figure 4.29 (bottom).

This dependency on vacancy formation influences the faster diffusion along the grain boundaries with a requirement of low activation energy when compared to the diffusion rate through the grains, since it is more likely that large amount of disorder is formed due to the vacancies at the grain boundary [57]. This dissimilarity in diffusion rates is one of the reasons of non-ideal diffusion behavior seen in some polycrystalline materials [58]. The grain boundary diffusion coefficient can be orders of magnitude larger than the grain interior diffusion coefficient [57]. Diffusion in polycrystalline materials was categorized based on the difference among the grain interior diffusion length, the average grain width, and the grain boundary width and are classified as type A, B, and C (Figure 4.30), where Type A is uniform diffusion through grains and grain boundaries, type B is diffusion preferentially through grain boundaries and type C is diffusion entirely through grain boundaries.

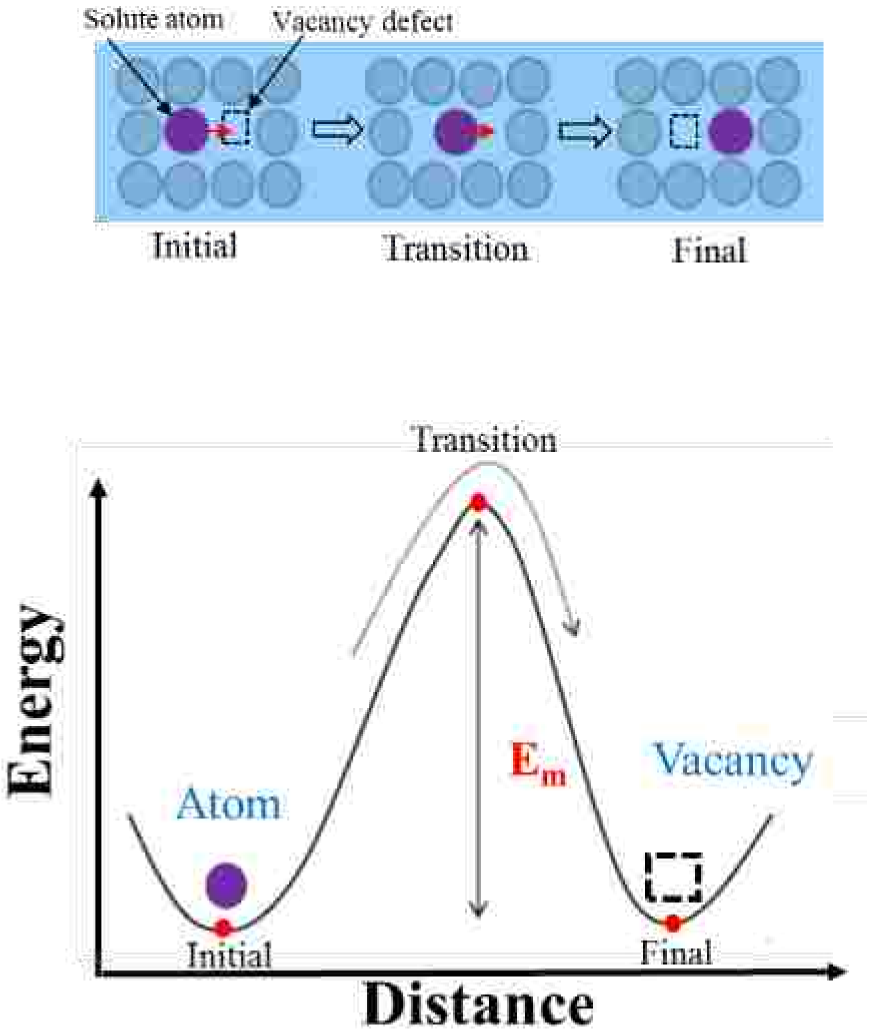

Figure 4.29: Vacancy mechanism with diffusing atom in transition state (top) and energy vs. position of diffusing atom showing the activation energy of a lattice jump (bottom).

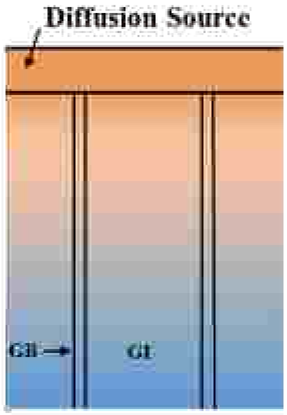

Type A

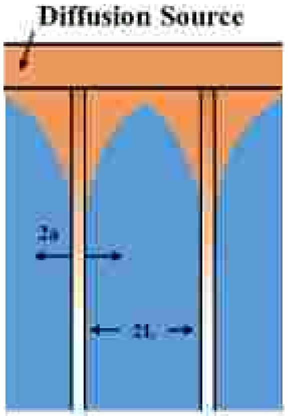

Type B

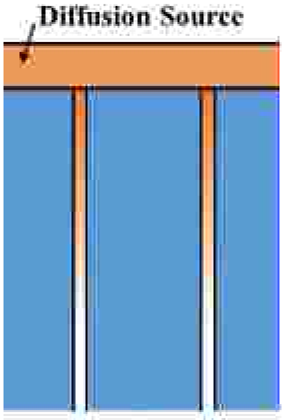

Type C

Figure 4.30: Usual concentration profiles in polycrystalline materials for type A, type B, and type C diffusion mechanism as labeled.

4.4.2 Preliminary Study of Diffusion Mechanism with a Simple Model

In the preliminary study, a simplified mathematical model was developed to get a better understanding of the mechanism behind the influence of temperature on the impurities diffusion process through the Mo films.

Impurity diffusion through the molybdenum films were modeled using Fick's law, which general form is defined by [58]:

$$\frac{\partial C(x,y,t)}{\partial t} = D(x,y)\nabla^2 C(x,y,t) \tag{4.5}$$

where C is the concentration of impurity and D is the diffusion coefficient. In our first model, diffusivity was considered to be ***only due to the contribution of diffusion through grain boundary*** (Type C). Here, y is defined as the direction parallel to the grain boundaries, and x is the direction perpendicular. Assuming the impurity diffusion happens mostly through the Mo grain boundaries, the above expression can be reduced to the following equation:

$$\frac{\partial C(x,t)}{\partial t} = D_{bound}\frac{\partial^2 C(x,t)}{\partial x^2} \tag{4.6}$$

where the boundary conditions are defined below:

$$C(x=0,t) = C_0 \qquad \frac{\partial C(x=L,t)}{\partial x} = 0 \tag{4.7}$$

Here, C_0 is the impurity concentration at the surface and L is the film thickness. In this preliminary study, it was assumed that the SLG has a very large Na diffusion coefficient (impurity considered here) that allows a constant concentration at the Mo/SLG interface. On the other hand, far from the Mo/SLG interface, the Na concentration is observed to be predominant, except at the Mo surface, which is neglected in this analysis.

The following initial condition was set:

$$C(x,t=0)=0 \tag{4.8}$$

This assumption is valid if the Mo film growth is assumed to be at least slightly faster than the Na diffusion. With these types of constraints, Bergman et al. derived the following solution [55]:

$$\frac{C_0 - C(x,t)}{C_0} = \sum_{n=1}^{\infty} K_n \exp(-\lambda_n^2 \frac{Dt}{L^2}) \cos(\lambda_n \frac{x}{L}) \tag{4.9}$$

where the coefficient K_n is [56]:

$$K_n = \frac{4 sin\lambda_n}{2\lambda_n + \sin(2\lambda_n)} \tag{4.10}$$

The values of λ_n are obtained from the transcended equation [41]:

$$\lambda_n \tan(\lambda_n) = A \tag{4.11}$$

where λ_n represents the Eigen values and A is a very large number. Incropera et al. [56] have found that, when the factor Dt/L^2 is larger than 0.2, the series solution can be approximated by the following equation:

$$\frac{C_0 - C(x,t)}{C_0} = 1.2733 \exp(-2.4674 \frac{Dt}{L^2}) \cos(1.5708 \frac{x}{L}) \tag{4.12}$$

SIMS data provided are in terms of intensities whereas the mathematical model above uses concentration values. A conversion was therefore performed, taking into account the geometry through which the SIMS depth profiles are obtained (Figure 4.31) as well as the contribution of the grains versus the grain boundaries in our specific case (Figure 4.32). The intensity of the beam (I) is proportional to the mass being sputtered (m), while the concentration (C) is equal to mass divided by the volume. The volume being sputtered (V) is given by:

V=At

where t is the depth that is sputtered over a unit time (Figure 4.31), and A is the area of the sputtering beam size (Figure 4.32), with both t and A constant. Therefore:

$$\frac{Intensity}{V} = \frac{Intensity}{At} \propto \frac{m}{V} = \mathrm{C}$$

Since t is constant, $\frac{Intensity}{A} \propto \mathrm{C}$

by fitting equation (4.12) to the experimental intensity data from SIMS analysis, the diffusion coefficient can be obtained using:

$$\frac{C_0 - C(x,t)}{C_0} = \frac{I_0 - I(x,t)}{I_0} \tag{4.13}$$

where I is the intensity of the impurity element (in this case Na) from the SIMS data and I_0 is the initial intensity of the impurity element (in this case Na) from the SIMS data from the glass source. The sharp increase and accumulation of Na at the Mo surface and the SLG/Mo interface features observed in the SIMS profile were not considered in this model. Influence of other parameters at the Mo surface will be studied in detail in the future. To extract the diffusivity values, Mo deposition time was taken to be 5400 seconds (90 minutes) long. The film thickness values are listed in Table 4.3.

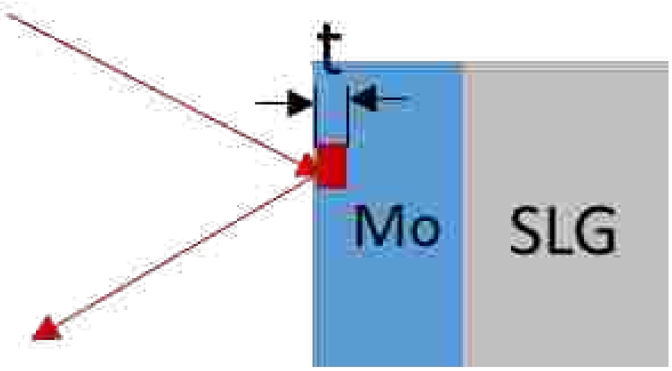

Figure 4.31: Schematic diagram demonstrating sputtering of Mo film for SIMS data acquisition. Note that the figure is not drawn to scale.

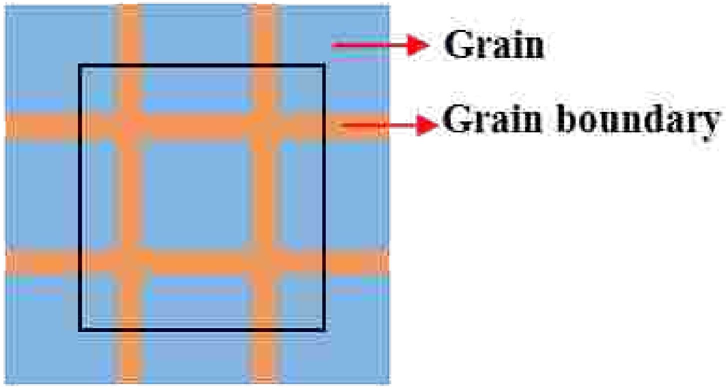

Figure 4.32: Hypothetical schematic diagram (top view) demonstrating grain, grain boundary and sputtering beam area A (black rectangle). Note that the figure is not drawn to scale.

Table 4.3 Film thickness values from cross-sectional SEM measurements.

T_{SS} (°C)	Film Thickness (nm)
23	550
50	450
100	500
150	490
200	530
250	500

Figure 4.33 plotted the comparison between simulated data (C/C_0 versus x/L) from the model and the experimental data from the SIMS depth profile, for all the deposition temperatures. The theoretical model and the experimental data are in good agreement for the temperatures 100, 150 and 200°C for the bulk part, but not as much for the regions near the surface of the films. At lower temperatures (RT and 50°C), the model does not fit well as the depth profile has a different shape, indicating a different diffusion process. At higher temperatures (above 250°C), the model does not fit as well, as a new shape for the depth profile appears, especially at the surface.

The values of the grain boundaries diffusion coefficient ($\mathbf{D_{boundary}}$) extracted from the model are reported in Table 4.4, along with the grain size (XRD), the term Dt/L^2 and the calculated grains diffusion coefficient ($\mathbf{D_{grain}}$). The term Dt/L^2 was checked and found to be larger than 0.2, indicating an appropriate approximation. The values of $\mathbf{D_{boundary}}$ and $\mathbf{D_{grain}}$ are also plotted as a function of temperature in Figure 4.34.

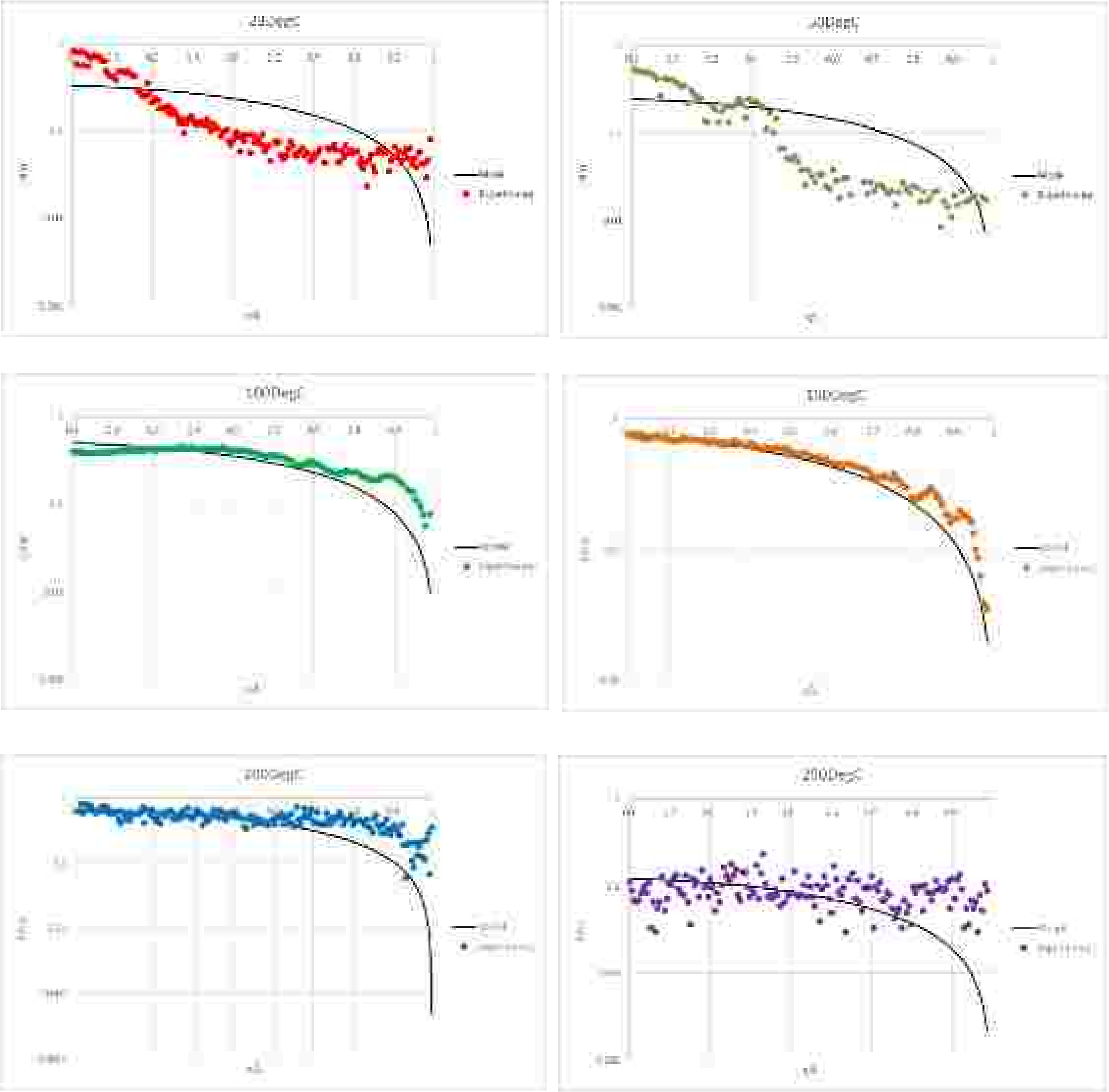

Figure 4.33: Comparison between simulated data (C/C_0 versus x/L) from the model and experimental data from the SIMS depth profile.

Table 4.4 Theoretical and estimated diffusion coefficient for Na through grain boundary and the grain along with simulation parameters.

T_{SS} (°C)	Modeled Boundary Diffusion Coefficient $D_{boundary}$ (cm^2/s)	Calculated Grain Diffusion Coefficient D_{grain} (cm^2/s)	Grain Size (nm)	D^*t/L^2
23	$3.0\ 10^{-13}$	$2.5\ 10^{-25}$	5	0.53
50	$2.5\ 10^{-13}$	$1.3\ 10^{-23}$	7	0.66
100	$1.7\ 10^{-13}$	$4.6\ 10^{-21}$	8	0.37
150	$1.0\ 10^{-13}$	$4.0\ 10^{-19}$	10	0.22
200	$1.3\ 10^{-13}$	$1.3\ 10^{-17}$	15	0.25
250	$4.4\ 10^{-13}$	$2.3\ 10^{-16}$	29	0.95

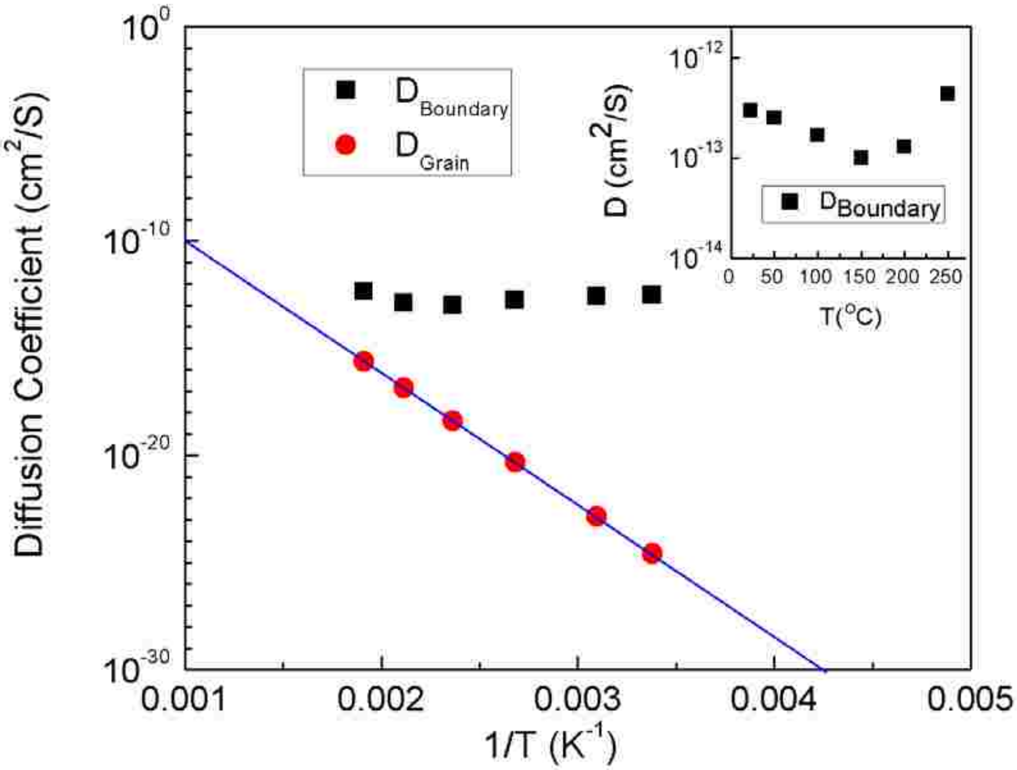

Figure 4.34: Grain boundaries diffusion coefficient extracted from the model as a function of temperature.

To ensure that the original hypothesis we could follow where a type C diffusion process was appropriate, the diffusion coefficients in the grain were calculated. An Arrhenius type relation was used with an activation energy E_a of 117 kJ/mol [60]. The pre-exponential factor was obtained by knowing that the Na diffusion coefficient in Mo is 2.3X10^{-10} cm^2/s at 800°C [38]. The diffusion coefficient in the grain is then given by:

$$D_{Grain}(T) = D_{0Grain}\exp(-\frac{E_a}{RT}) \quad (4.14)$$

The diffusion coefficients in the grain, as shown in Table 4.4, are effectively lower than the diffusion coefficients at the grain boundaries for the values taken.

It is interesting to note from Table 4.4 that the grain boundary diffusion coefficients stay within the same order of magnitude whatever the temperature is, while the grain diffusion coefficient change by 9 orders of magnitude. It is likely that another phenomenon is competing with the temperature change to cause such as small change of $D_{boundary}$. As we saw in the previous section, the level of oxygen is changing from one sample to another and could be part of this change of diffusion coefficient.

Overall, this shows that an enhancement of the mathematical model is needed to address the influence of the change in grain structures as the deposition temperature changes. One way to do that is by using numerical simulation on COMSOL.

4.4.2 Necessity for a new Diffusion Model

A modification of the theoretical model is required to accommodate the fact that the sputtering beam during SIMS data acquisition actually gathers contributions from both grain and grain boundary (Figure 4.35). One can see that depending on the deposition temperature, the proportion of grains and grain boundaries is drastically different.

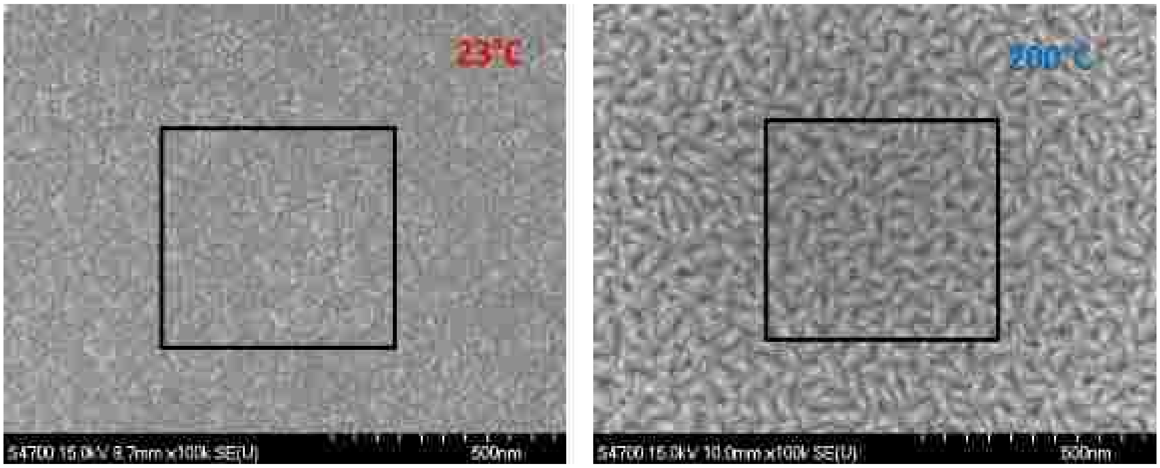

Figure 4.35: The fixed beam size sees the same area of the films during SIMS measurement (black rectangle) but the grain size increases as a function of T_{SS} and the beam encounters less grain boundary at higher temperature.

After a literature review and looking into numerous existing diffusion models [56] for various systems (such as diffusion kinetics in thick vs thin films), we observed that for most of the cases the models have restrictions of parabolic profiles. After a thorough analysis of the experimental SIMS depth profile data, comparing those with other models [57] and correlating the results from XRD and SEM measurements, it has been estimated at this point that the SIMS depth profiles are not well fitted by a parabolic profile. The theoretical models studied [57] do not include a compact equation to accommodate both the contribution of grain and grain boundary diffusion while extracting diffusivity values after applying a fit to the experimental data. The models also do not address the issue of evolution of grain structure and therefore having different parameters for different types of grain structures. This problem needs to be addressed in a new model.

4.5 Conclusions

In this chapter, the study involves investigating the microstructural, electrical and chemical properties of Mo films deposited on SLG for different substrate temperatures (T_{SS}) while keeping the deposition pressure and power at fixed values. The Mo films' structure was examined by X-Ray Diffraction (XRD). It was shown that the films had a preferred orientation along the (110) direction whatever the temperature was. A reduction of the FHWM with temperature indicated an increase in grain size, from 5 nm at RT to 29 nm at 250°C. AFM and cross section SEM shows little variation in surface roughness with temperature, which stays around 4-6 nm. Electrical properties of the films, obtained by Hall effect measurements, showed that the properties of the films remained stable above 50°C, but that the conductivity was lower for the RT samples. Using SIMS and XPS, the chemical properties and depth profile of the impurities were studied. It was observed that for all classical impurities diffusing from the glass (Na, K, Mg, Ca), T_{SS} made a difference, with Na and K raising from RT to 100C then decreasing, while Mg and Ca concentration were decreasing more uniformly. The films were oxidized, specifically at the surface, but no change in chemical bounding was observed by XPS, whatever temperature was used. A theoretical model was used to simulate the diffusion of impurities through the film, assuming it was mostly through grain boundaries. A good fit was obtained for the bulk part of the intermediate temperatures (100, 150, 200) but not for the low temperatures (which had a different profile shape) or the high temperature (which surface concentration was quite different). The diffusion coefficient through the grain boundaries was extracted from this modeling and shows a different trend than the calculated diffusion coefficient through the grains. This indicates that another competing phenomenon occurs, beside the change in temperature, probably link to a change in chemical composition occurring at the grain boundaries.

CHAPTER 5

STUDY OF VARIOUS BILAYER MOLYBDENUM FILMS AND ASSOCIATED CIGS SOLAR CELLS

5.1 Introduction

To obtain higher efficiencies in CIGS solar cells, a small amount of sodium incorporation is essential to improve the open circuit voltage and fill factor of the devices [ref]. The use of soda lime glass as the Na source is the simplest of all available methods. Sodium diffuses through the Mo layer when subject to high temperature (typically greater than 450°C) during the CIGS growth. The requirements of a bilayer Mo back contact have been introduced in the previous chapter. One of our collaborators from the University of Toledo reported an increase in V_{OC} and FF values when CIGS solar cells were fabricated on Mo films deposited at 250°C compared to those on room temperature Mo films [55]. In their work, extensive spectroscopic ellipsometry analysis was presented with some ex-situ electrical analysis, where better device performances were attributed to lower resistivity and higher density film obtained at 250°C. Further ex-situ analysis was not reported, specially the modification of the profile of various elements, such as Na and K, which play a crucial role in V_{OC} and FF for CIGS solar cells. The highest CIGS solar cell efficiency record holder company, Solar Frontier, expressed great interest in seeing detail systematic studies of the influence of substrate temperature and their corresponding outcome. They also have been conducting research [58] on the influence of Na and other elements for CIGS absorbing layer and the impact on device parameters, mainly V_{OC} and FF.

In this chapter, the influence of substrate temperature on bilayer Mo films has been studied. The films were characterized by Scanning Electron Microscopy (SEM) and X-ray Diffraction (XRD). Hall Effect measurements were also performed. The film morphology was studied with Atomic Force Microscopy (AFM). Secondary Ion Mass Spectroscopy (SIMS) was used to study different impurity profiles such as sodium, potassium, oxygen, magnesium and calcium. Devices were fabricated with these various back contacts (i.e. with Mo bilayer films deposited at various substrate temperatures) and the results were correlated with ex-situ measurements.

5.2 Characterization of Bilayer Molybdenum Films at Different Substrate Temperatures

For these experiments, molybdenum thin films were fabricated onto soda-lime glass (SLG) substrates using direct current (dc) magnetron sputtering. The argon pressure was set first at 10 mTorr and then at 3 mTorr, to obtain a traditional bilayer film. The substrate temperature (T_{SS}) was kept constant during each deposition, but was changed from one deposition to another to be either room temperature (RT), 100°C, 150°C or 200°C. The dc power was kept constant at 150 W. After deposition, the films were annealed in vacuum at 450°C to simulate the first stage process of the CIGS fabrication.

Figures 5.1 and 5.2 show SEM images (both plan-view and cross-section) of as-deposited and annealed films respectively with various T_{SS} in the range mentioned previously. It can be observed from the plan-view images that film surface structure gets smoother as T_{SS} increases for both as-deposited and annealed samples, except for the annealed sample with T_{SS} of 100°C, which appears to have comparatively a rougher surface. All the films have columnar structure (both as-deposited and annealed) and do not show significant variation as the deposition temperature varies. Also, the two layers deposited at two different pressures are not visible either due to very low thickness of the first layer and/or poor resolution of the SEM equipment.

Figure 5.3 shows the XRD spectra for Mo films deposited at different T_{SS} (samples labeled AD for as deposited). It was observed that the preferred orientation of the films was (110), whatever the temperature was. One can also observe that the full width at half maximum (FWHM) of the peak decreases with increasing temperature (Figure 5.4), indicating an increase in grain size [3]. The peak intensity increases for higher T_{SS}, which indicates an increase of the films' crystallization with temperature, as the thickness was kept constant. Another feature of this curve is a slight shift of the peak for each film (Table 5.1), which might indicate the variation in the average lattice spacing [4] when T_{SS} varies or a relaxation in the film stress.

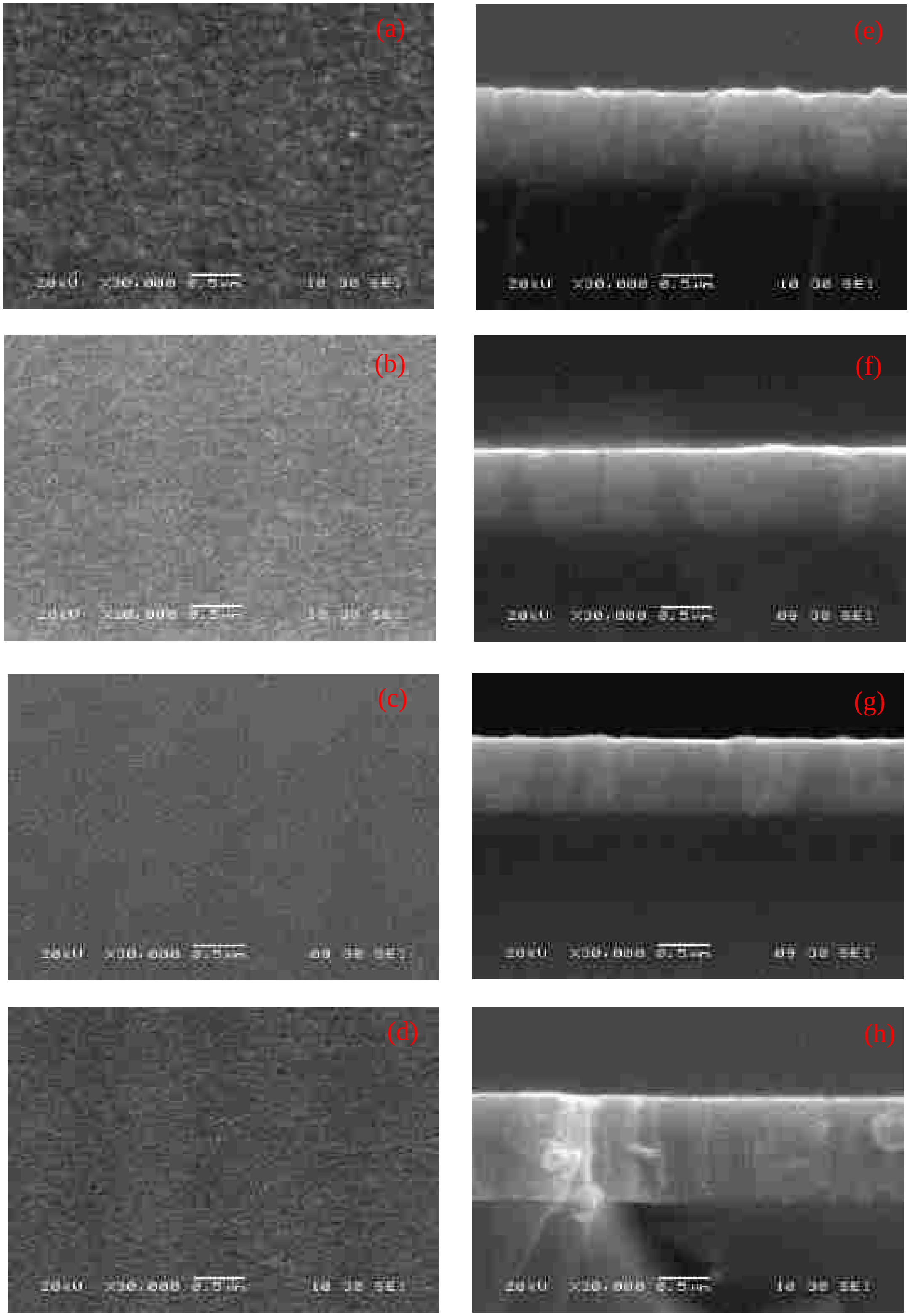

Figure 5.1: SEM images of as-deposited films, plan-view: (a) RT, (b) 100°C, (c) 150°C, (d) 200°C and cross-section: (e) RT, (f) 100°C, (g) 150°C, (h) 200°C.

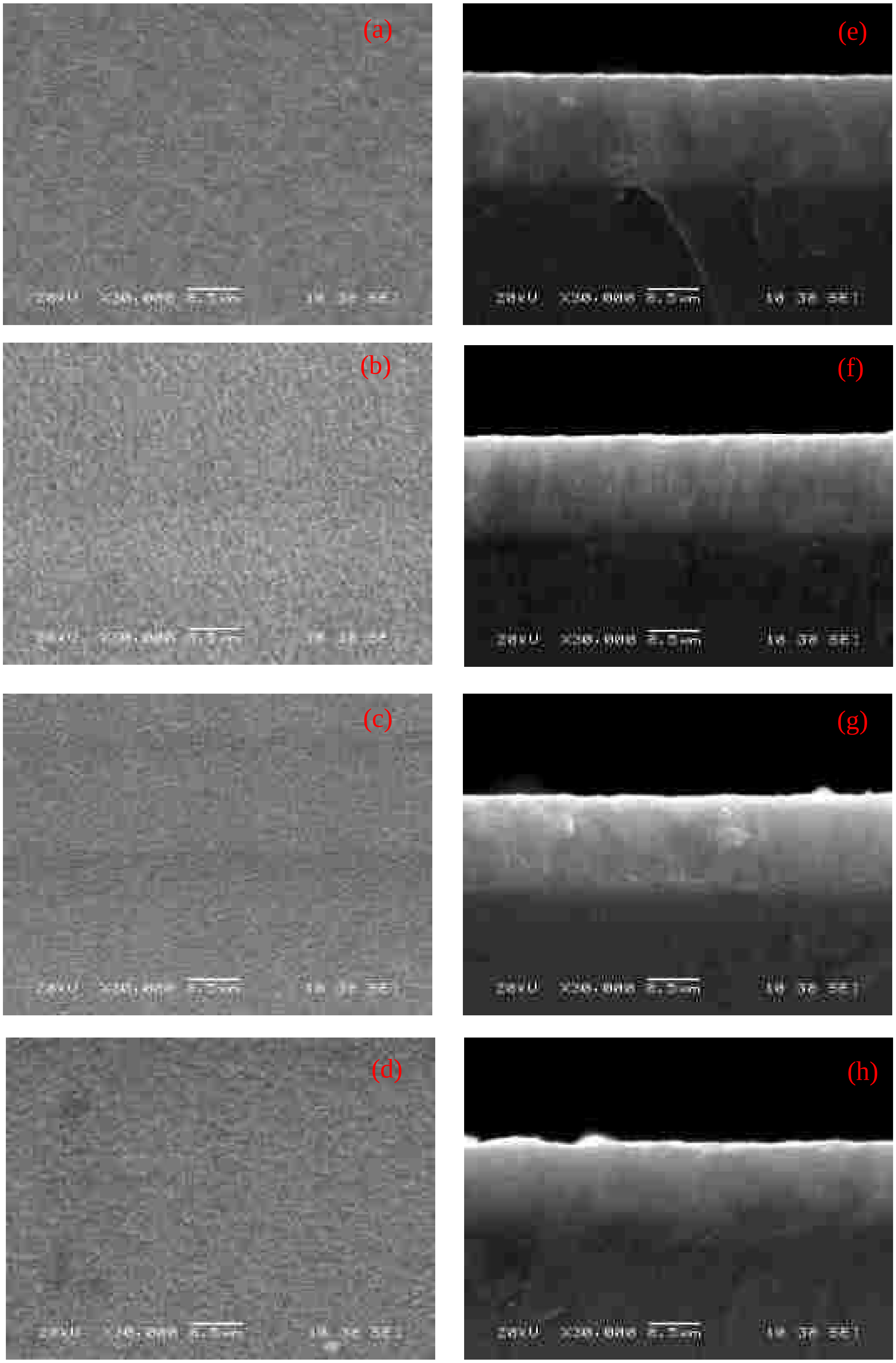

Figure 5.2: SEM images of annealed films, plan-view: (a) RT, (b) 100°C, (c) 150°C, (d) 200°C and cross-section: (e) RT, (f) 100°C, (g) 150°C, (h) 200°C.

Additional orientations at (220) and (211) were present for the films deposited at 100°C and 150°C, but were not observed at RT for the (220) and at 200°C for the (211). The (220) orientation increases with the (110) orientation as the temperature increases, as expected. The lattice constant and the d-spacing values have been summarized in Table 5.1 for the (110) peak.

These sets of samples were then annealed (samples labeled AN) in a vacuum at 450°C. The peak intensities decreased for all annealed samples when compared with the corresponding AD films. There is an especially significant reduction for the samples with T_{SS} of 100°C as well as no (220) peak (Figure 5.4). The FWHM values for the (110) orientation decreased for all annealed samples except for the samples with T_{SS} = 100°C.

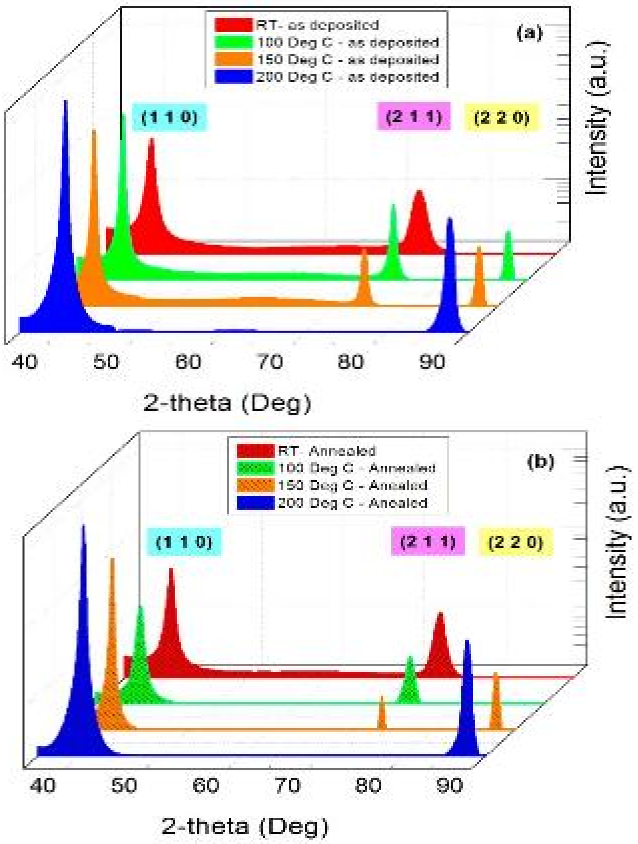

Figure 5.3: XRD patterns of the various bilayers Mo films on SLG as a function of substrate temperature (a) as deposited and (b) annealed.

Table 5.1 XRD peaks analysis of Mo films (as deposited and annealed) for various substrate temperatures.

T_{SS} (°C)	2θ (°)	d (Å)
RT-AD	40.379	2.231
RT-AN	40.750	2.221
100-AD	40.524	2.224
100-AN	40.517	2.224
150-AD	40.498	2.225
150-AN	40.505	2.225
200-AD	40.510	2.225
200-AD	40.536	2.223

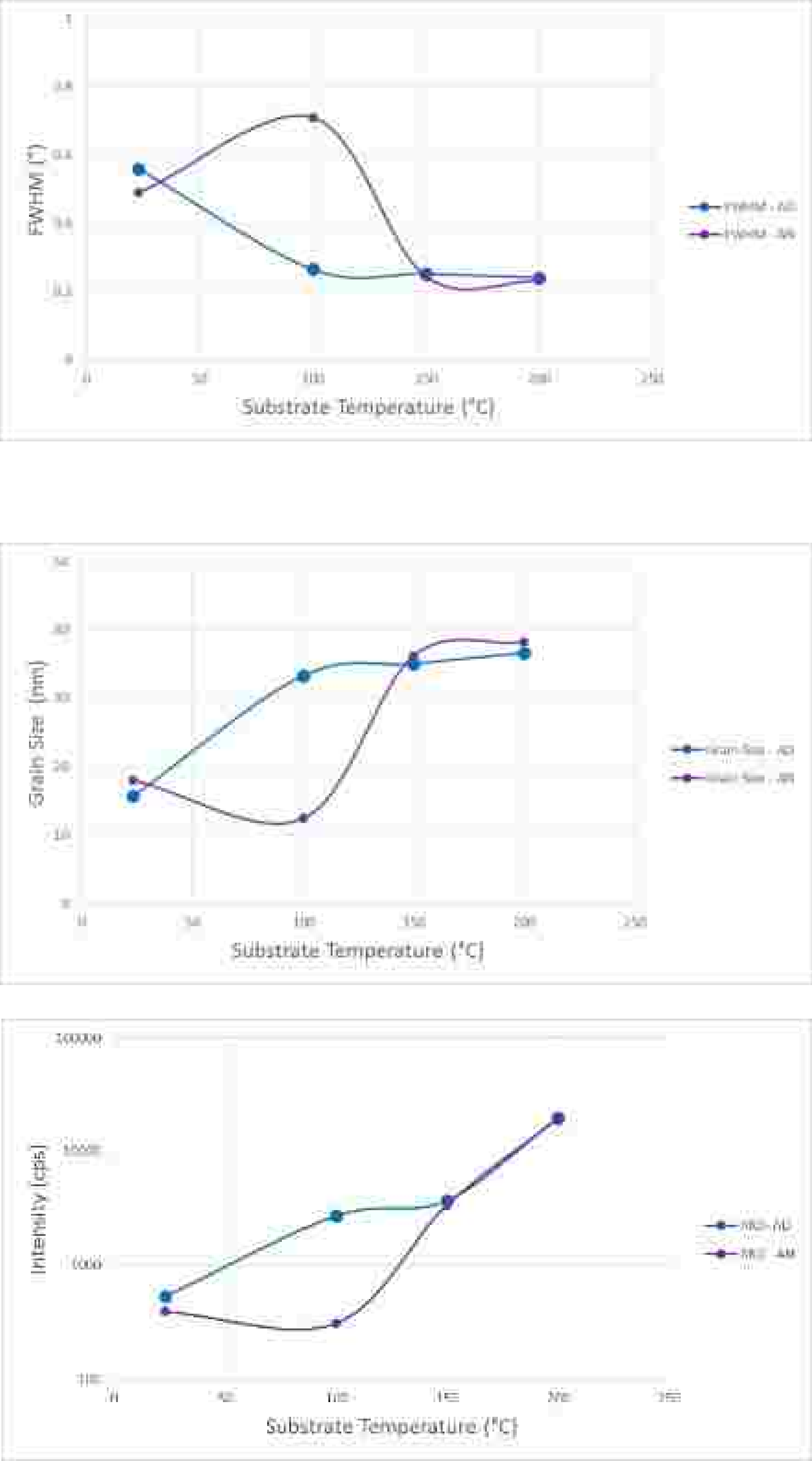

Figure 5.4: Comparison of as deposited and annealed Mo films for FWHM (top), grain size (middle) and XRD peak intensity (bottom).

Association between XRD peak intensity and calculated grain size for the as deposited (AD) and annealed (AD) films were made as shown in Figure 5.5. For AD films, both peak intensity and grain increases with T_{SS} with a sharp increase in grain size from room temperature to 100°C values. XRD peak intensity for the AN films follow the similar pattern those of the AD films. However, the grain size for the 100°C decreased drastically.

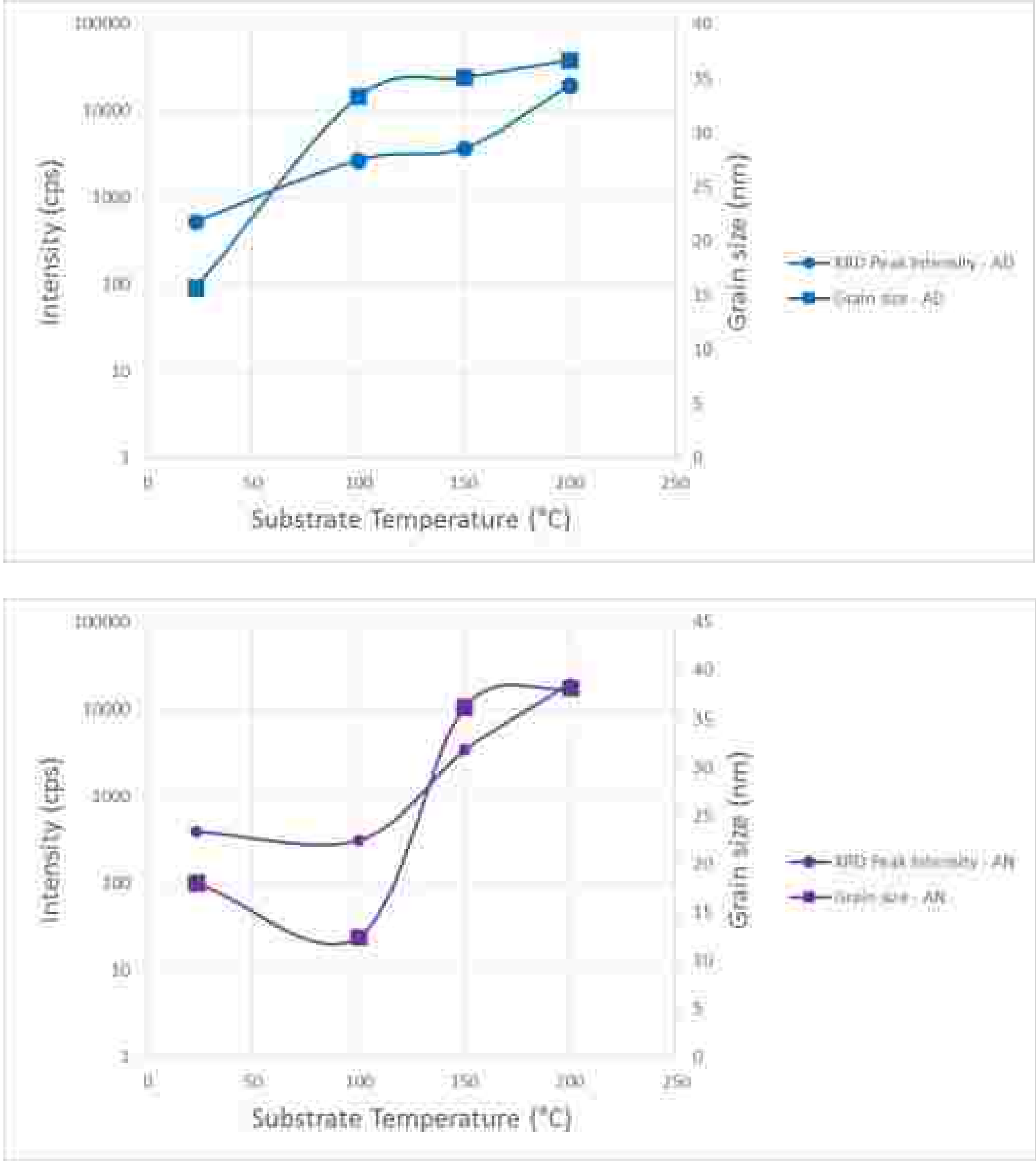

Figure 5.5: XRD peak intensity and calculated grain size association for the as deposited (top) and annealed (bottom) films.

Hall Effect measurements were performed on all as-deposited and annealed films. The resistivity values of these films from Hall Effect measurement are presented in Figure 5.6, and are compared with the resistivity values obtained through sheet resistance measurement. It can be seen that both measurement data are in agreement. For both AD and AN films, the resistivity tends to decrease as T_{SS} increases.

To analyze this decrease in resistivity, the conductivity of these films was correlated with the XRD peak intensities (Figure 5.7). For both AD and AN films, increase in peak intensities can be observed, which is an indication of better crystallinity and hence the better conductivity.

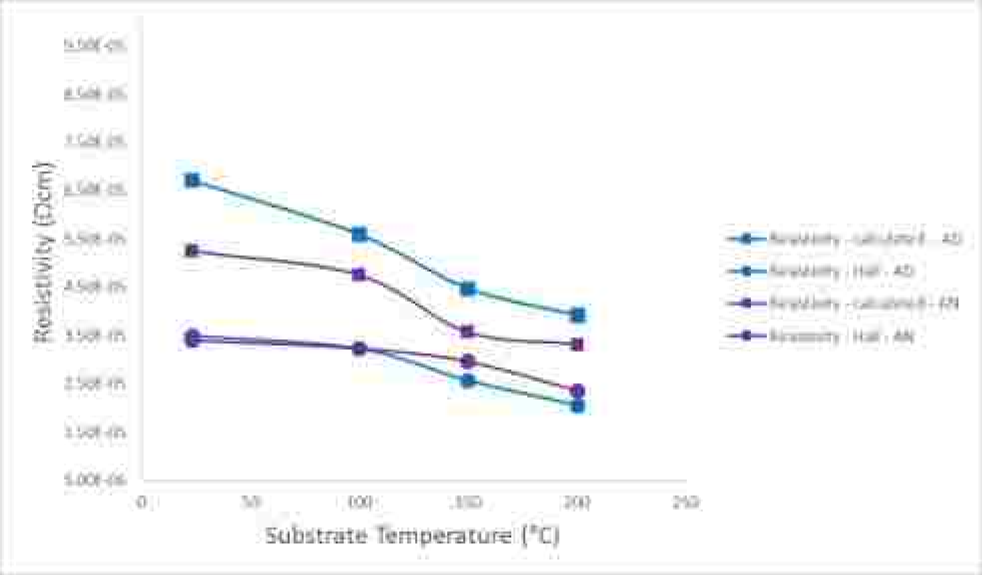

Figure 5.6: Resistivity of the as deposited and annealed films measured with Hall Effect and calculated from sheet resistance values.

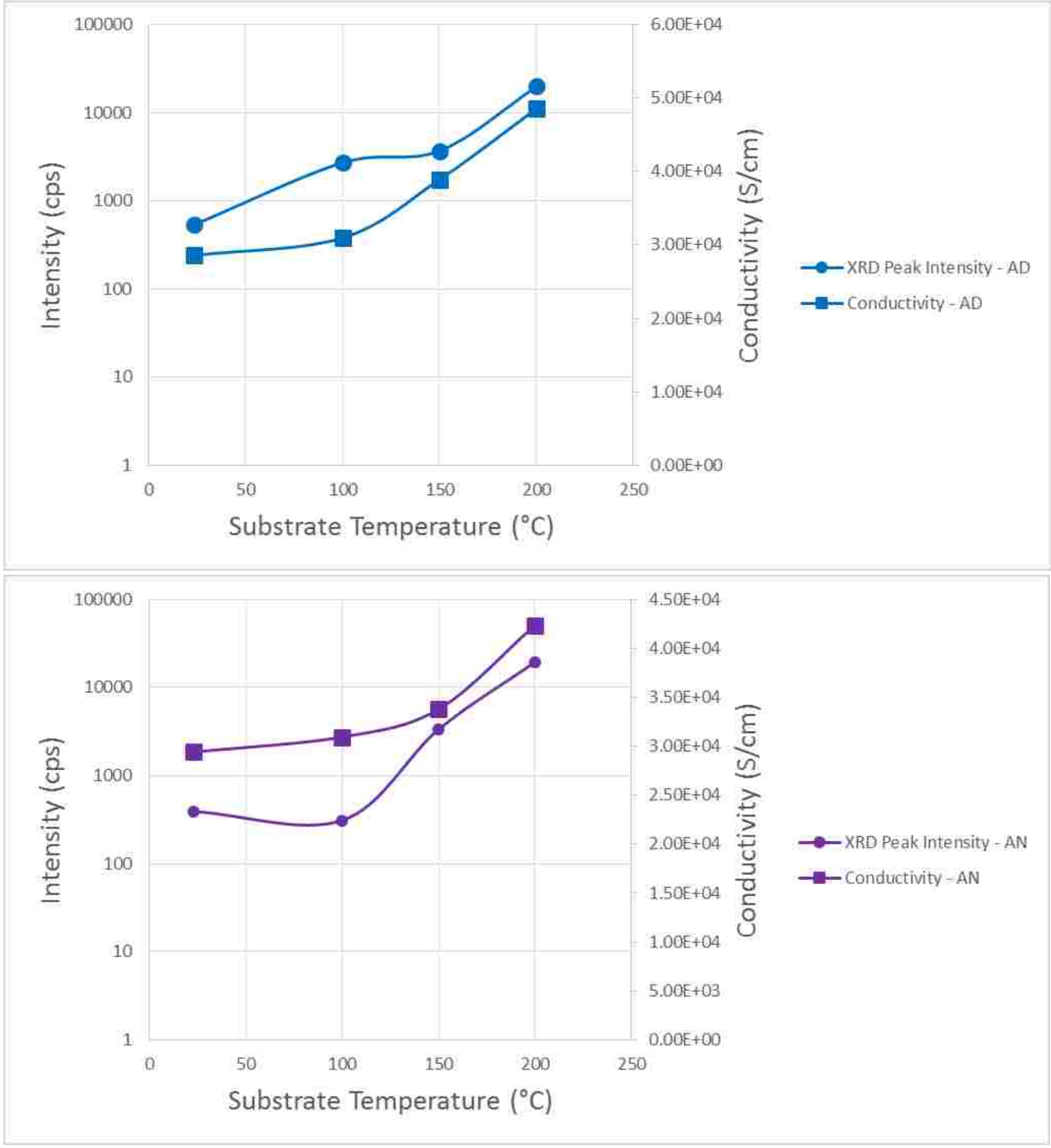

Figure 5.7: Correlation of XRD peak intensity and conductivity for as-deposited (top) and annealed (bottom) films on SLG as a function of substrate temperature.

In Figure 5.8, a comparison between single and bilayer films was made for the FWHM and grain size values. Only as-deposited bilayer films were used for the comparison. FWHM decreases for both types of films as the T_{SS} increases which is an indication of larger grain size. It is interesting to note the effect of deposition pressure on both FWHM and grain size. Films deposited with higher pressure exhibit higher FWHM values which results in smaller grain size for all the temperatures in this study.

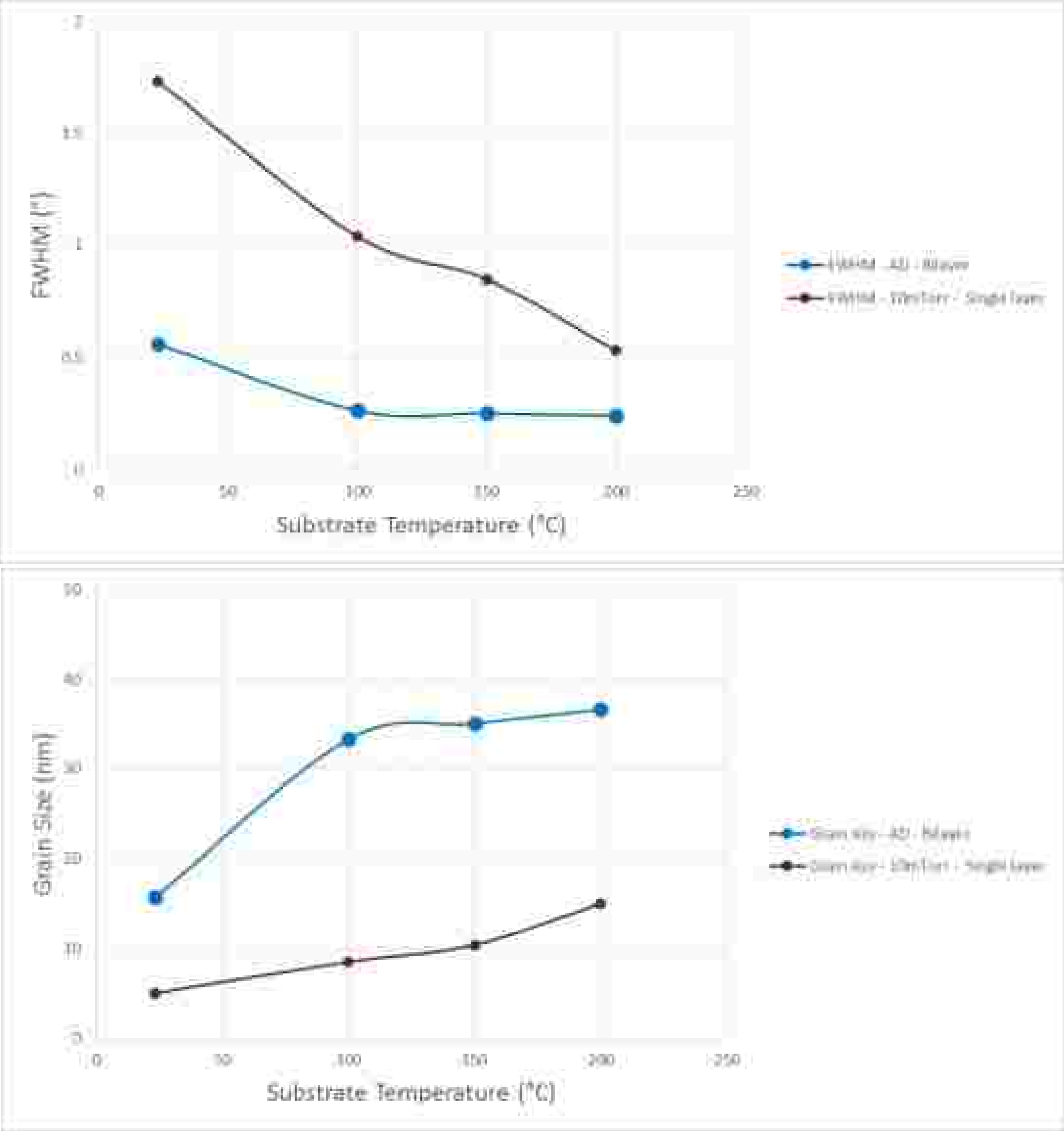

Figure 5.8: Comparison of FWHM (top) and grain size (bottom) values between single layer (deposited at 10mTorr) and as-deposited (AD) bilayer films as a function of T_{SS}.

The film morphology measured by AFM for the as deposited and annealed samples as a function of T_{SS} is shown in Figure 5.9. The films deposited at 200°C exhibit relatively smoother surface compared with the other films. The RMS roughness decreases from 6.37

nm to 3.65 nm, as substrate temperature increased from room temperature to 200°C (Figure 5.10). For the AN samples, the roughness decreases slightly for all temperatures, except for the samples deposited at T_{SS} of 100°C, which roughness increased to 9 nm. Figure 5.11 shows the RMS roughness values for both bilayer and single layer films. In this case only as-deposited bilayer films are used for the comparison and the top layer is deposited at 3 mTorr pressure as opposed to 10 mTorr pressure for the single layer film growth. Roughness values for bilayer films decrease as the T_{SS} increases where the single layer films exhibit the opposite. This reverse trend could be due to the difference in deposition pressure, which causes the substrate temperature variation to have a different effect on these two sets of samples.

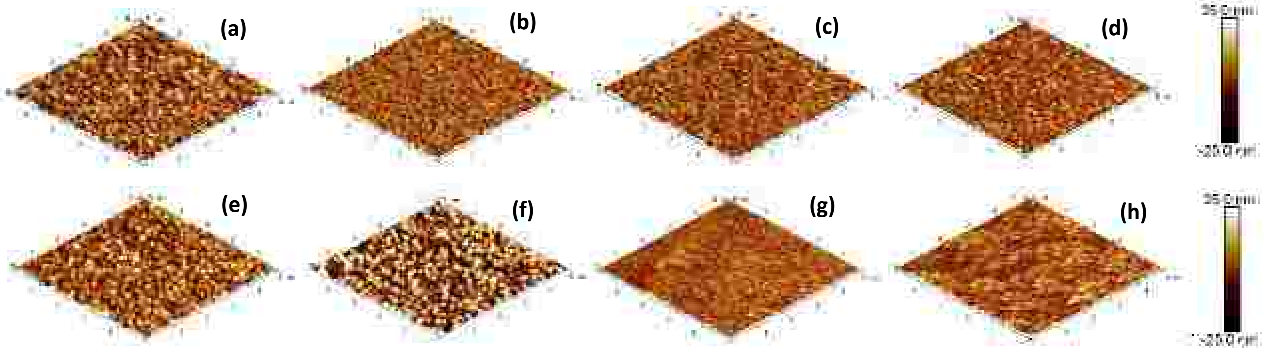

Figure 5.9: AFM images of the Mo films: as deposited (a) RT, (b) 100°C, (c) 150°C, (d) 200°C and annealed (e) RT, (f) 100°C, (g) 150°C, (h) 200°C.

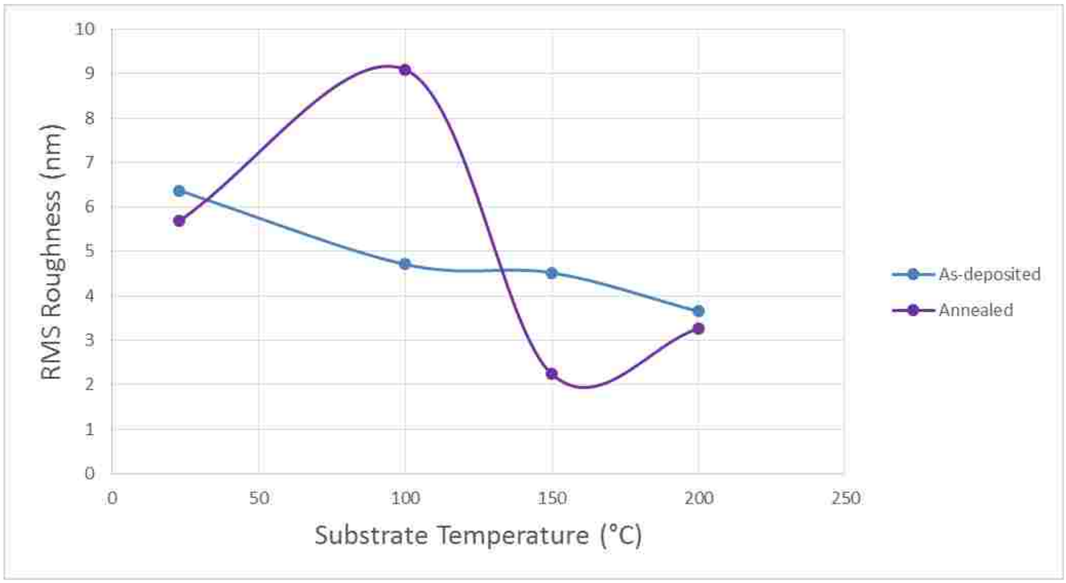

Figure 5.10: Comparison of RMS roughness values between as-deposited (AD) and annealed (AN) bilayer films as a function of T_{SS}.

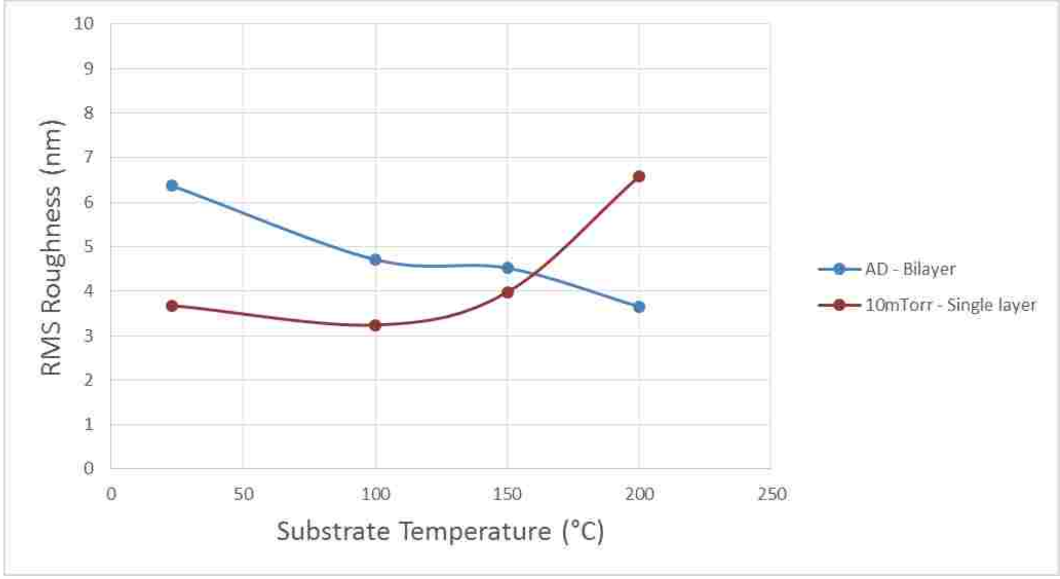

Figure 5.11: Comparison of RMS roughness values between single layer (deposited at 10mTorr) and as-deposited (AD) bilayer films as a function of T_{SS}.

SIMS depth profiles were used to characterize the sodium (Na) concentrations through both AD and AN Mo films as a function of T_{SS} (Figure 5.12). A sharp edge appears at the glass interface for all the films, and is highlighted in the figures. These four samples have slightly different thickness, as confirmed with Profilometer measurements. Due to differences in thickness and in the scan rate during SIMS measurement, all measurement data did not have the same number of points and for all the plots, depth profiles were aligned at the glass/film interface for better visualization. None of the plots for demonstrating depth profile were normalized. It is necessary to add at this point that quantification with SIMS data is not very accurate. Distinctive diffusion profiles for two different pressure values can be observed easily and have been labeled. This is due to the fact that change in deposition pressure introduces change in grain density, which is a controlling factor for diffusion mechanism (ref). If we look at the 10 mTorr part of the profile, we can see that Na diffusion is higher for the majority portion of the film with T_{SS} of 100°C and starts to decrease as T_{SS} increases. For the 3 mTorr pressure portion of the films, the highest Na signal can be observed for the room temperature film and a gradual decrease can be seen as T_{SS} increases. For the annealed films, the Na signal level decreases with T_{SS} throughout the entire bilayer. Na profiles for AD and AN samples were compared for individual temperatures separately and it was found that, for all cases, AN samples had higher signal levels for both deposition pressures. A similar trend was observed in the case of O_2 depth profiles for both AD and AN films when all four temperature profiles were compared together (Figure 5.13).

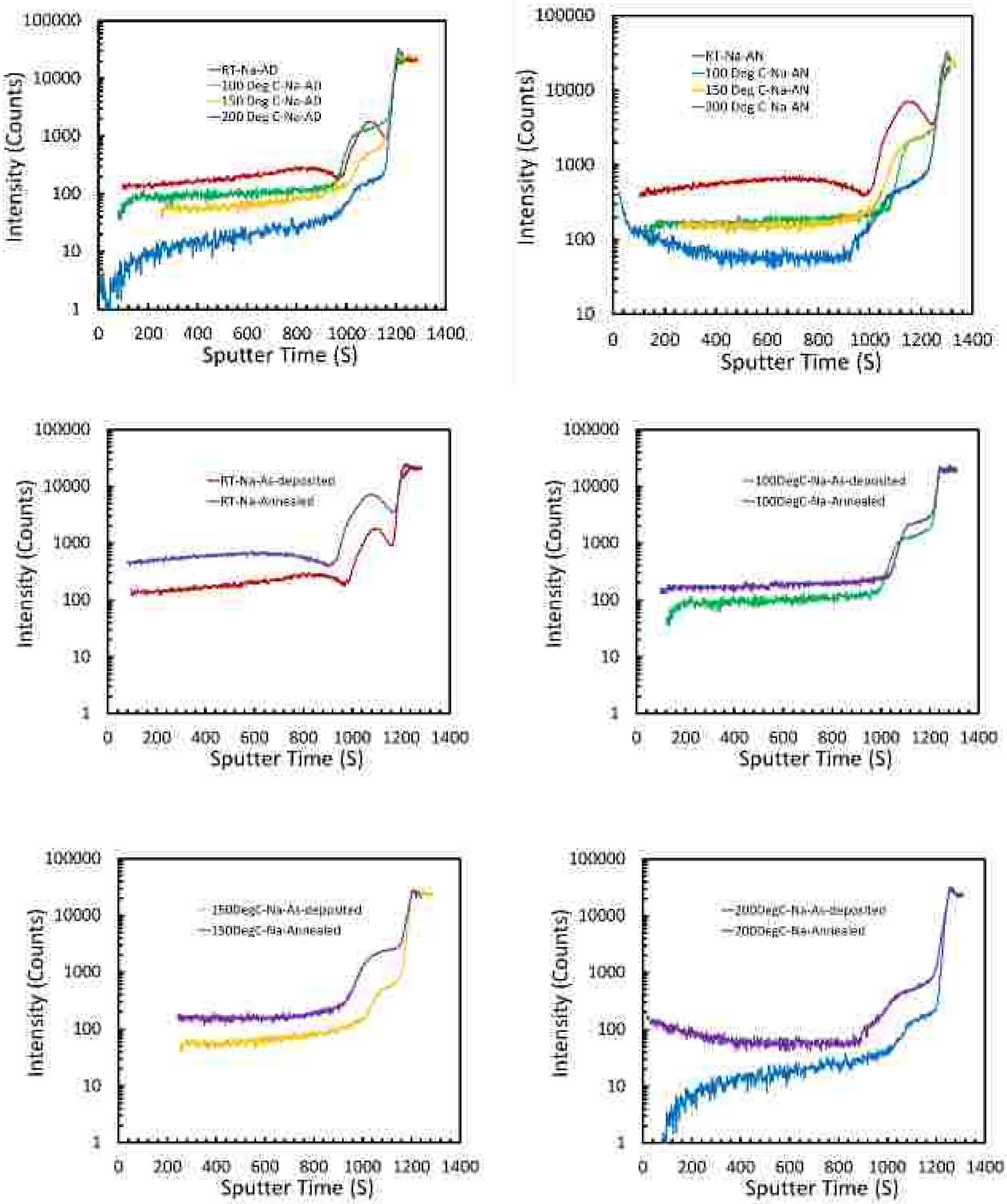

Figure 5.12: SIMS analysis for Na depth profiles of the as deposited (AD) and annealed (AN) Mo films on SLG as a function of substrate temperature. The AD and AN films are compared separately for all four T_{SS}.

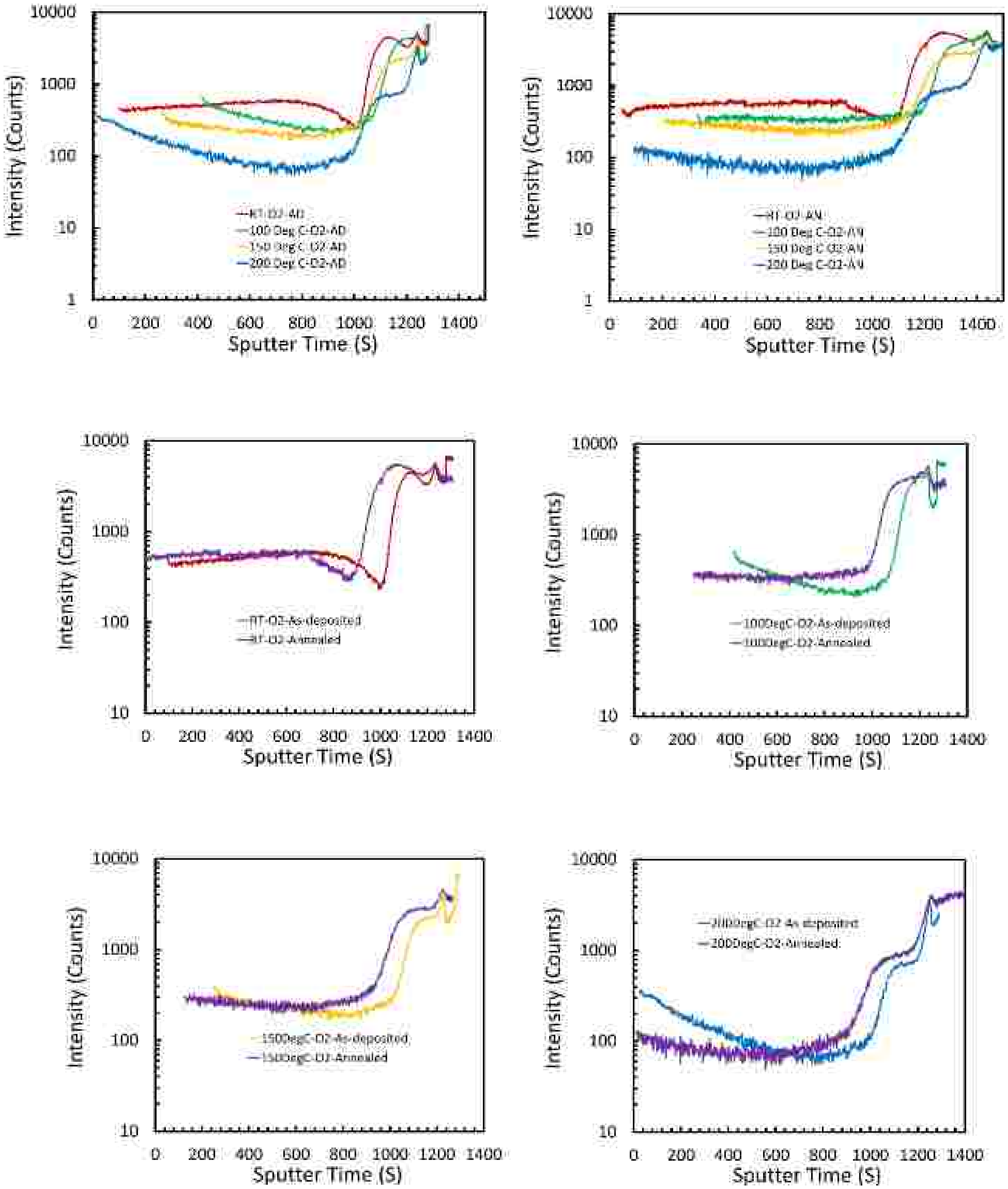

Figure 5.13: SIMS analysis for O_2 depth profiles of the as deposited (AD) and annealed (AN) Mo films on SLG as a function of substrate temperature. The AD and AN films are compared separately for all four T_{SS}.

However, the comparison between AD and AN films for individual temperatures separately for O_2 did not show the similar profile as for Na. AN films had higher O_2 for 10 mTorr deposition pressure and for the second layer with 3 mTorr pressure, O_2 had more or less similar intensity level. Association of oxygen level with that of the Na level has been attempted, and a correlation can be observed in general for the portion of the films deposited at 10 mTorr pressure and more prominent for the 3 mTorr region, i.e. the oxygen level decreases as the deposition temperature increases. Similar correlation was observed and has been discussed in chapter 4.

If we look at Figure 5.14, we can see that, for the K signal, the intensity level is higher for a certain portion of the film with T_{SS} of 100°C and starts to decrease as T_{SS} increases, similar to the Na depth profile. However, the influence of the deposition temperature for the high pressure region of the film does not exhibit a similar nature, i.e. the K intensity is at a similar level except for the sample with T_{SS} of 200°C, which is lower than the other 3 samples. These features completely change when the samples are annealed. The overall K intensity level increases around 10 orders of magnitude for the annealed samples when compared with the as-deposited samples. The diffusion profile in the 10 mTorr region of the annealed samples changes drastically especially for the room temperature sample and it can be seen distinctly that the K intensity starts to decrease as the deposition temperature increases. When the K intensity level for as-deposited and annealed were compared individually for each temperature, it can be seen that the intensity increased significantly throughout the entire film for all four samples, which is quite unlike the case for Na and O_2 profiles.

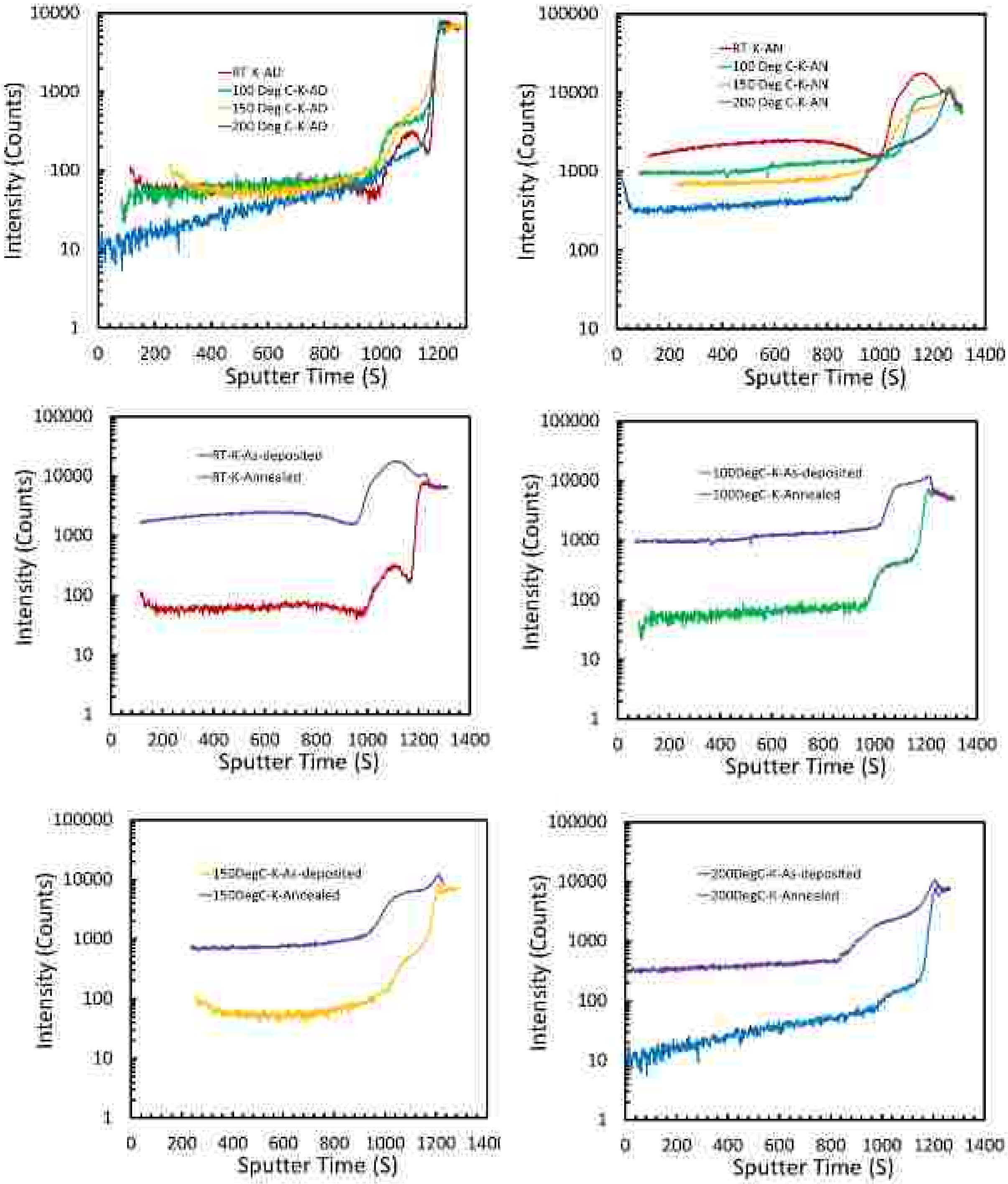

Figure 5.14: SIMS analysis for K depth profiles of the as deposited (AD) and annealed (AN) Mo films on SLG as a function of substrate temperature. The AD and AN films are compared separately for all four T_{SS}.

MoO_2 profiles for as-deposited and annealed films (Figure 5.15) show similar features: in general, the intensity decreases as the deposition temperature increases. Ca and Mg intensity levels are almost in the noise level for both as-deposited and annealed films (Figure 5.16, 5.17 respectively). Only for room temperature as-deposited sample, Ca can be seen in the film slightly. It might be due to the reason that these elements evaporate from the glass substrates when subject to elevated temperatures and do not get to diffuse as the film keeps growing.

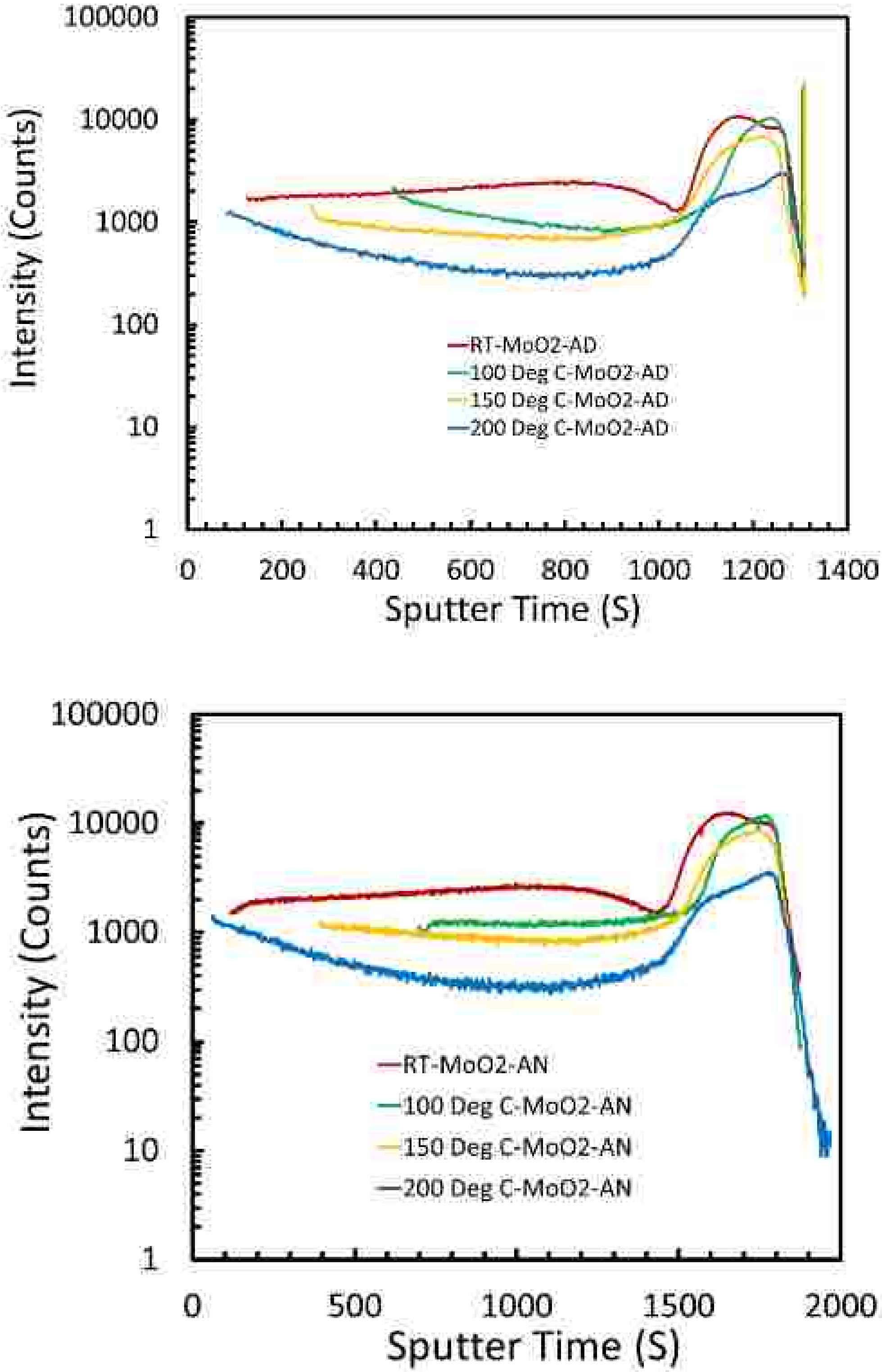

Figure 5.15: SIMS analysis for MoO_2 depth profiles (a) as-deposited (AD) and (b) annealed (AN) of the Mo films on SLG as a function of substrate temperature.

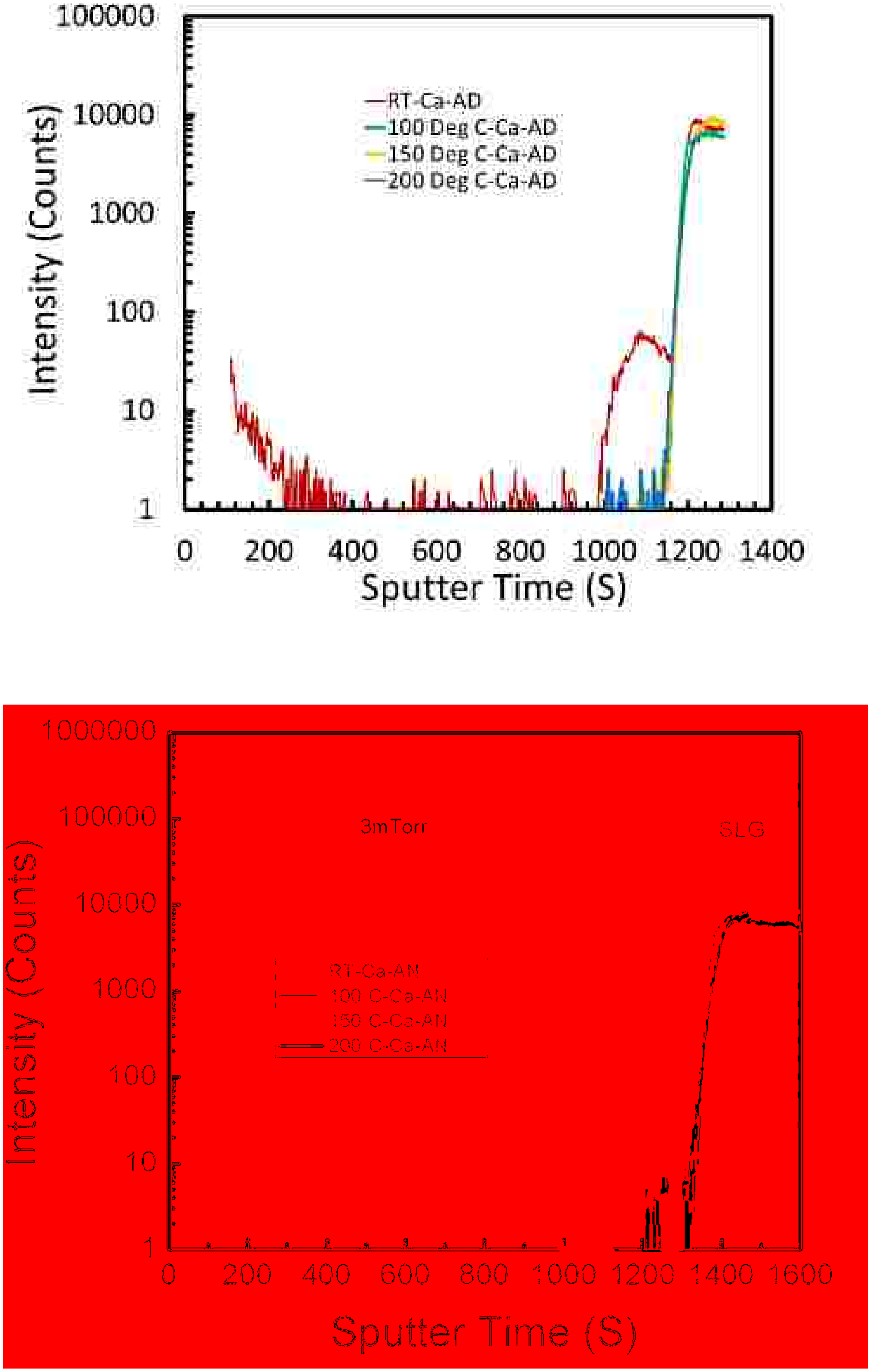

Figure 5.16: SIMS analysis for Ca depth profiles (a) as-deposited (AD) and (b) annealed (AN) of the Mo films on SLG as a function of substrate temperature.

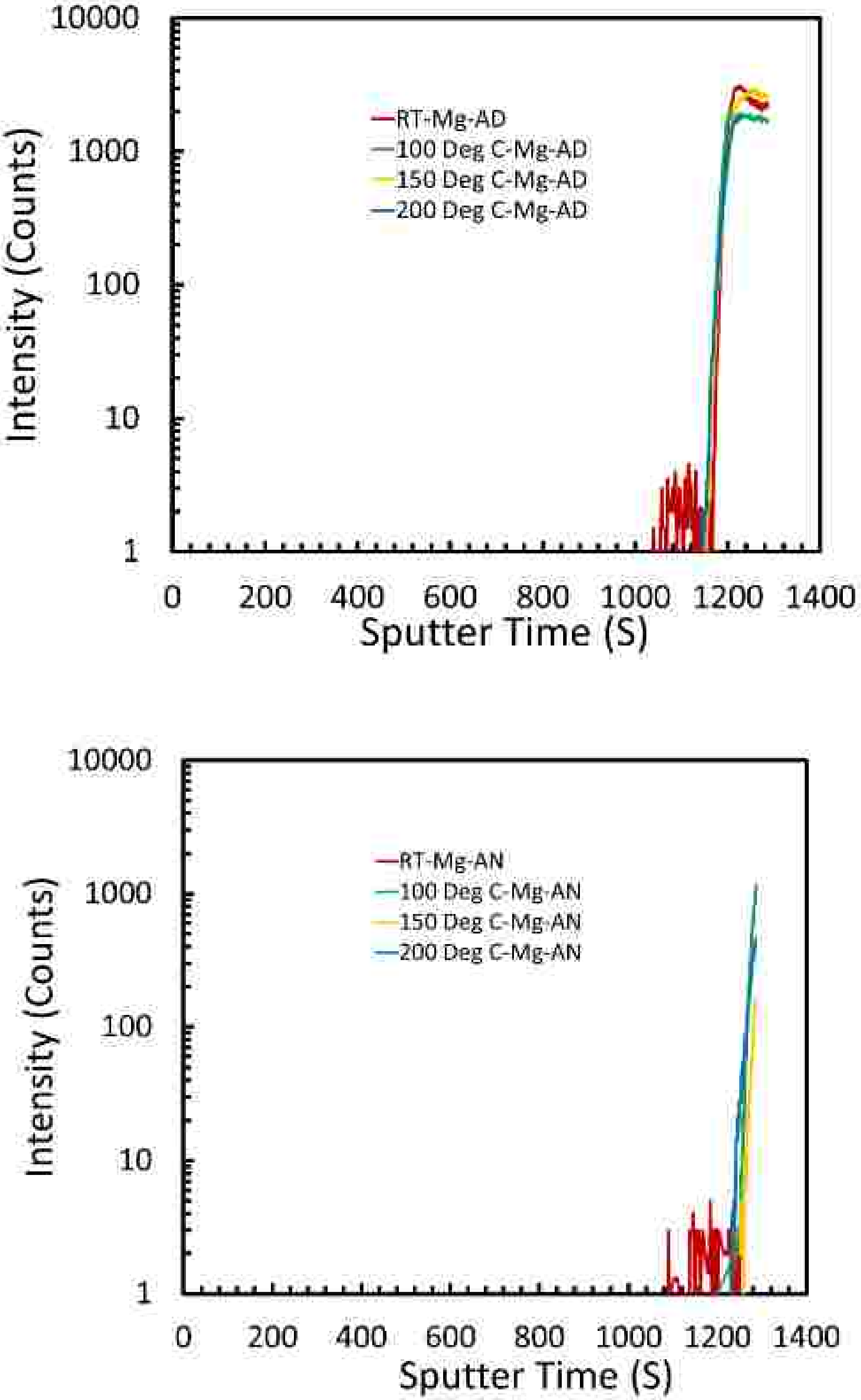

Figure 5.17: SIMS analysis for Mg depth profiles (a) as-deposited (AD) and (b) annealed (AN) of the Mo films on SLG as a function of substrate temperature.

Figure 5.18 shows the influence of T_{SS} on the sodium intensity level. One has to note that this is not an absolute estimation. Even though SIMS is poor in measurement in terms of quantification as mentioned before, it is interesting to see the similar behavior in the Na intensity level especially for T_{SS} = 100°C when compared with bilayer and single layer films from Chapter 4. The intensity levels were normalized as these measurements were performed in different facilities and the sensitivity factor differs from equipment to equipment.

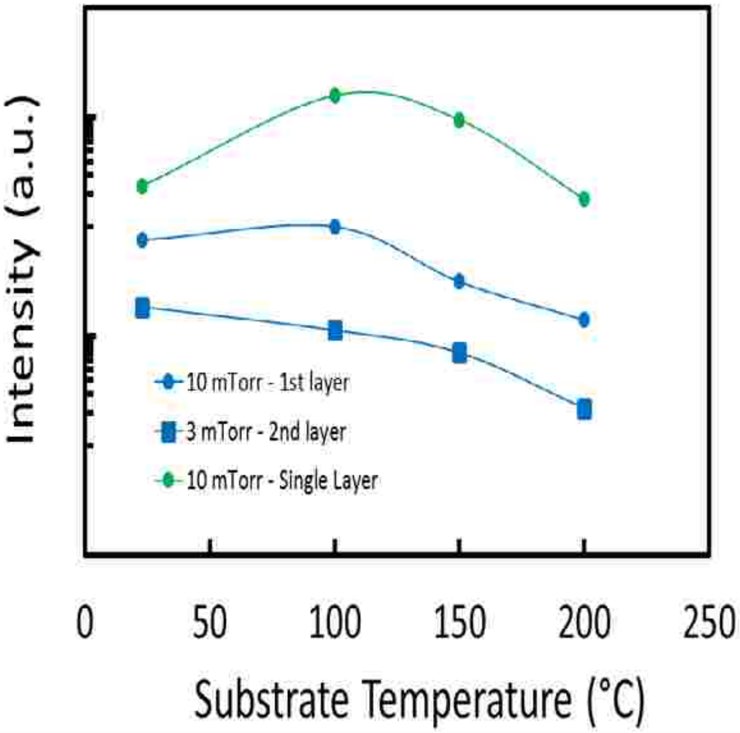

Figure 5.18: Na intensity as a function of T_{SS} from SIMS analysis, comparing single (deposited at 10 mTorr pressure) and bilayer films (1st layer deposed at 10 mTorr followed by a 2nd layer where the pressure was 3 mTorr). In all cases the intensity values were chosen from the middle of the film.

5.3 CIGS Solar Cells on Different Molybdenum Films

Figure 5.19 and 5.20 show the J-V and QE plots for the CIGS solar cell devices fabricated using the steps discussed in Chapter 1. Here, four different Mo back contacts were used which were deposited with 4 different substrate temperatures as listed in Table 5.2. Table 5.2 also lists the solar cell parameters. It can be seen that the highest efficiency was obtained when room temperature Mo films were used. All the other three devices have lower efficiency, mostly due to a lower FF. From the material analysis, it is observed that the films with a higher substrate temperature provided lower resistivity (Figure 5.6), which helps reduce series resistance and lead to better quality devices. Also, the surface was smoother for high T_{SS}, which should allow for better interface. On the other hand, SIMS analysis showed a lower Na level in the film with higher T_{SS}, which is known to degrade V_{OC} and FF. Consequently, as a result of these opposing effects, no significant changes were observed in overall device performance.

Semi-logarithmic plot of the J-V curve reveals much more information about the device compared to the linear one. Various regions of the J-V curve as shown in Figures 5.21 and 5.22 are dominated by different loss mechanisms and are used to obtain the diode parameters listed in Table 5.2. Figure 5.24 shows the change in diode parameters as the T_{SS} changes.

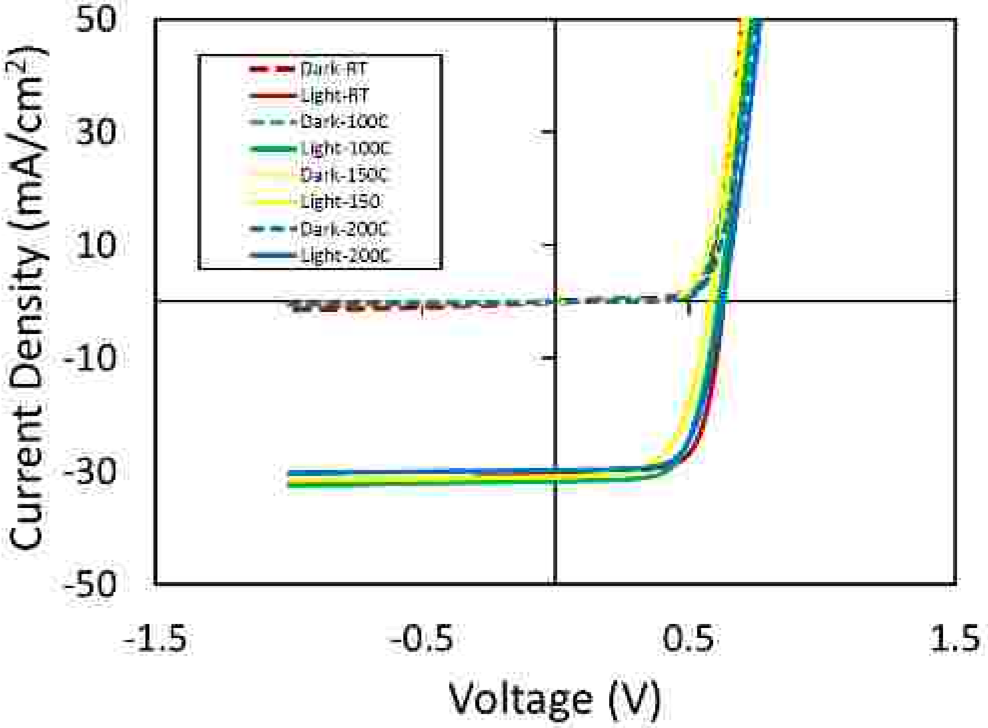

Figure 5.19: JV measurements of the devices with different Mo back contacts.

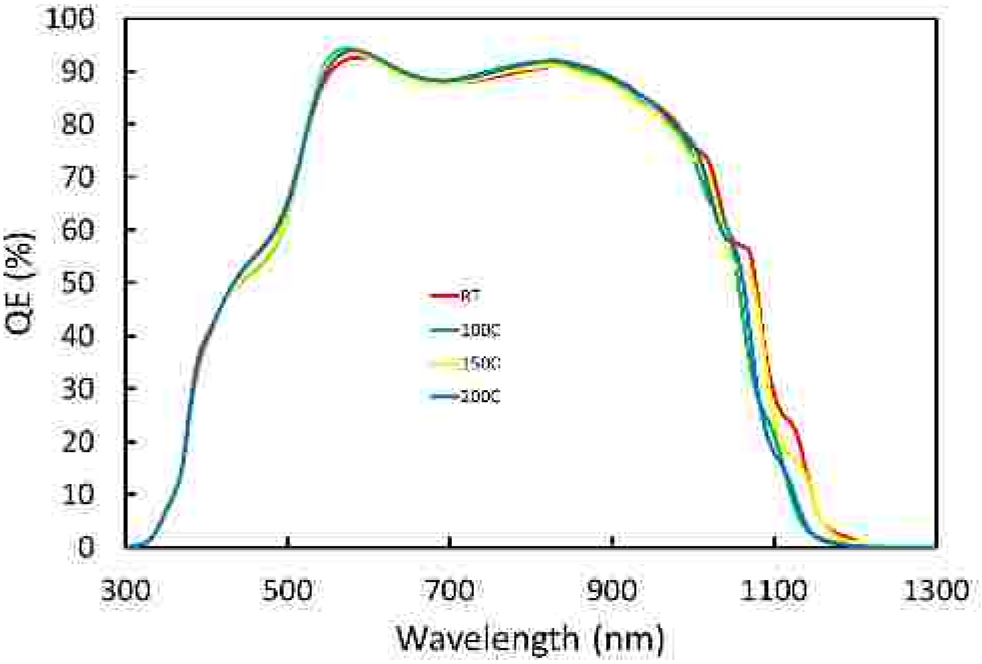

Figure 5.20: Quantum efficiency measurements of CIGS solar cell devices with different Mo back contacts.

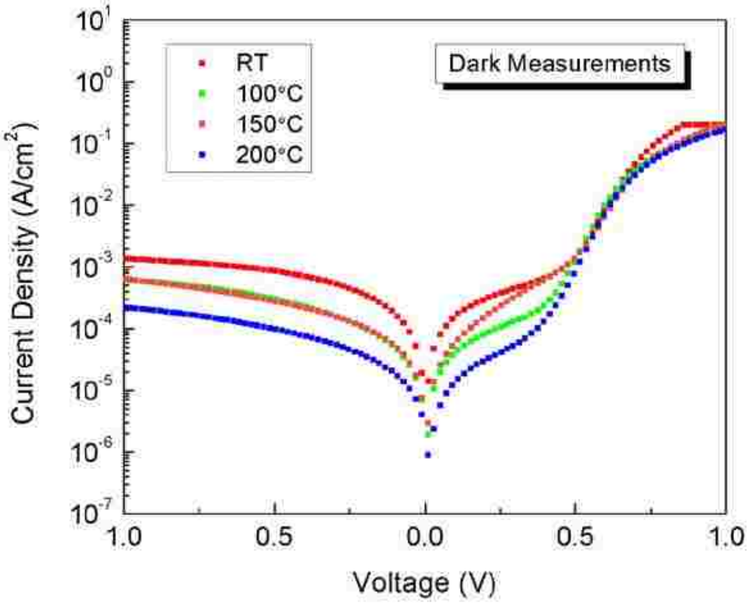

Figure 5.21: Comparison of dark JV plots for the best cells in semi-logarithmic scale.

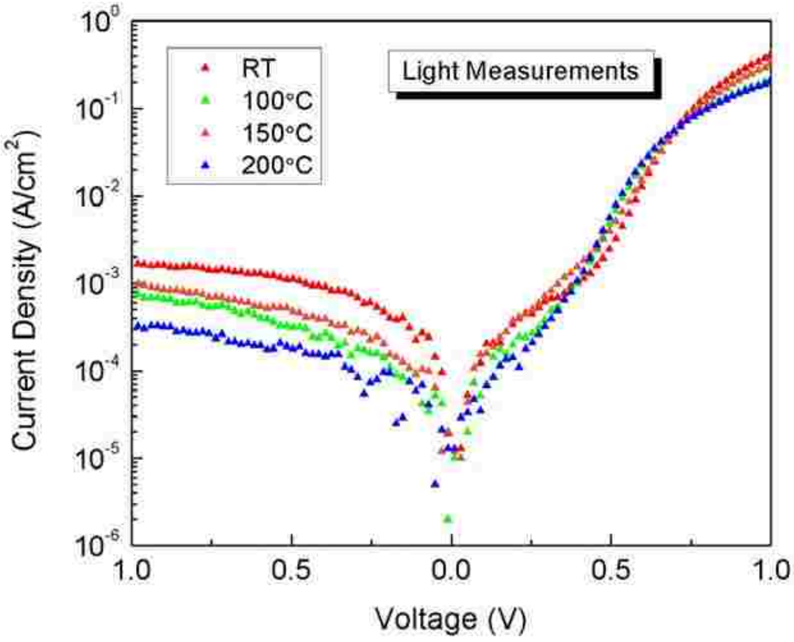

Figure 5.22: Comparison of light JV plots for the best cells in semi-logarithmic scale.

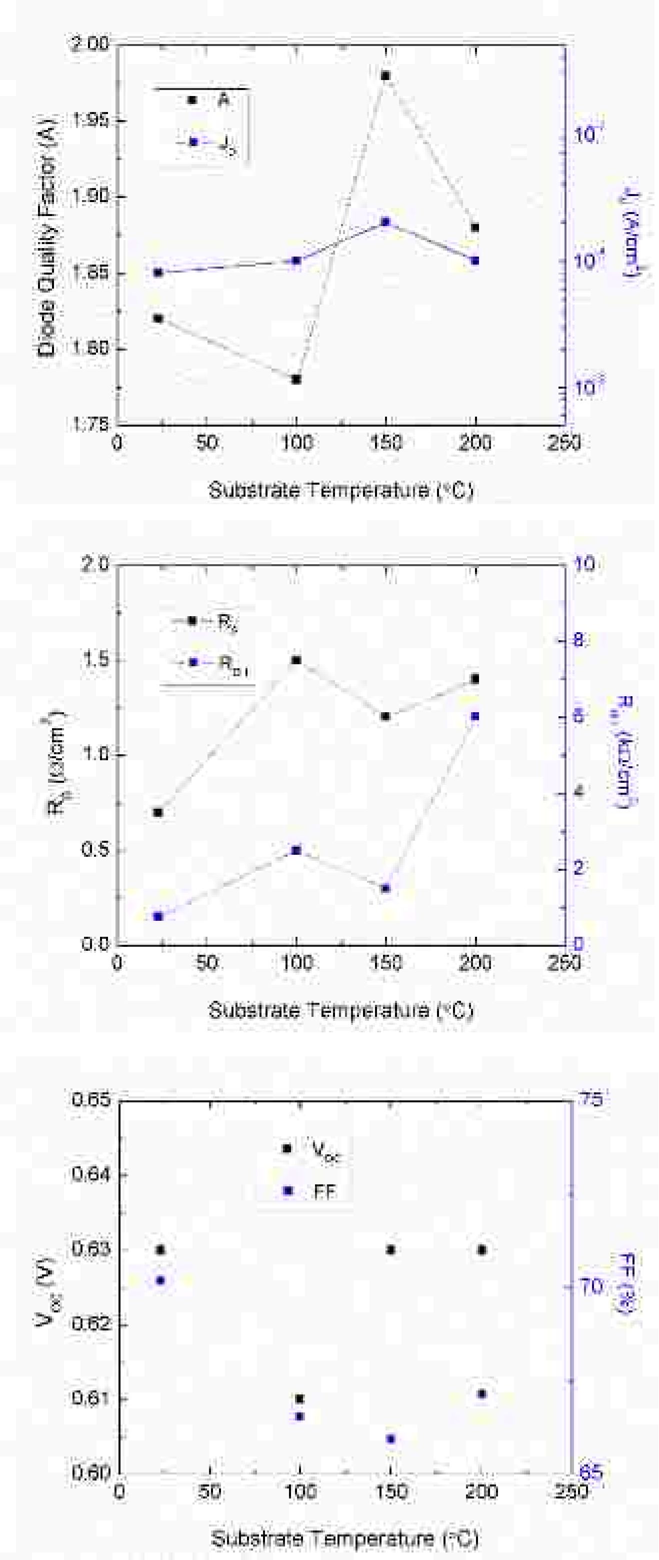

Figure 5.23: Plots showing A and J_0 (top), R_S and R_{SH} (middle) and V_{OC} and FF (bottom) as a function of T_{SS}.

Table 5.2 Summarized device parameters of CIGS solar cell deposited with different Mo back contacts. Diode parameters listed here were obtained from the dark measurements.

T_{SS} (°C)	**V_{OC} (V)**	**J_{SC} (mA/cm^2)**	**FF (%)**	**Efficiency (%)**	**Bandgap (eV)**	**A**	**J_0 (A/cm^2)**	**R_{SH} (kΩ/cm^2)**	**R_S (Ω/cm^2)**
23	0.63	34.3	70.2	15.1	1.12	1.82	8×10^{-09}	0.75	0.7
100	0.61	33.7	66.5	13.7	1.15	1.78	1×10^{-08}	2.5	1.5
150	0.63	32.9	65.9	13.8	1.16	1.98	2×10^{-08}	1.5	1.2
200	0.63	33.9	67.1	14.3	1.15	1.88	1×10^{-08}	6.0	1.4

As one can see in Table 5.2 and in Figure 5.23, the main change occurs for FF if we look at all substrate temperatures. The changes in current observations for all three higher temperatures are minimal and seem to be due more to a change in band gap than anything else, as illustrated by the QE measurements (Figure 5.20). The change in FF, on the other hand, is there for all three higher T_{SS}, and seems to be coming for an increase in series resistance. At the same time, the shunt resistance increases for higher T_{SS}, which is positive, but does not seem to compensate enough for the change in series resistance and slight increase in reverse saturation current.

5.4 CONCLUSIONS

It is of interest to note that all characterizations (SEM, XRD, AFM, and SIMS) for the 100°C are consistent, in that it exhibits unusual behaviors. It might be due to any sort of chemical reaction happening during the growth process in the sputtering chamber that is causing a change in the film formation. The role of Mo in controlling Na incorporation from soda lime glass using a modified deposition process has been studied thoroughly. Influence of electrical properties on the CIGS solar cell parameters has been discussed. It is important to note that the enhancement in efficiency obtained by the group at the University of Toledo might be due to better resistivity and Na control even though SIMS analysis has not been disclosed in their recent published articles. Their process temperature and deposition conditions differ from the facility we have, hence might be the reason of not producing a similar result. After in depth device analysis, it can be observed that a room temperature device shows better device efficiency, mostly due to a lower series resistance and reverse saturation current. Improvement in electrical properties for higher deposition temperature was not backed up by higher sodium diffusion in the film, hence no significant changes were observed from the devices performance specifically V_{OC} and FF. In the future, TEM cross-section could provide useful information regarding grain boundaries density, which is associated with sodium diffusion. As usual for solar cells fabrication, it can be established that obtaining higher efficiencies relies on fine tuning of multiple parameters, including elements present only in the films.

CHAPTER 6

CONCLUSIONS

6.1 Conclusions

Currently various technology options are available for harvesting the power of the sun, an energy source which is sustainable, and to produce electricity straight from this source by the photovoltaic effect. Among them, $Cu(In,Ga)Se_2$ has gained noteworthy momentum as a promising high efficiency and low cost thin film solar cell material. $Cu(In,Ga)Se_2$ (CIGS) solar cells are the most efficient polycrystalline thin films solar cells today with an efficiency of 22.6%. For high efficiency devices, efficient transport of the photogenerated carriers via the entire solar cell stack demands the same importance as the generation of these carriers, which can assure device quality $Cu(In,Ga)Se_2$. In order to achieve this target, it is vital to improve the back contact layer properties in the solar cell stack. The best performance from CIGS solar cells is achieved until now when molybdenum is used as the back contact material. It fulfills the most requirements for an effective back contact, particularly chemical and mechanical compatibility with the other deposition processes, high conductivity, low contact resistance with the CIGS layer, and matching thermal expansion coefficient. The deposition process and parameters play a vital role in attaining a layer with suitable properties. The main objective of this work is to comprehend the effect of different substrates, substrate heating and deposition process conditions on diffusion of various impurities and on the properties of the molybdenum films.

In Chapter 1, an introduction of solar cell technology, an outline of the dissertation objectives, and motivation were presented.

In Chapter 2, the materials properties of the molybdenum films and the characterization techniques used to analyze the molybdenum films and devices were reviewed. Characterization methods ranging from in-situ, real time growth monitoring to the characterization techniques for measuring the parameters of the completed solar cell device have been discussed. It is always suggested to utilize more than one characterization tool for the same material for developing a complete idea on a certain study, by correlating and thus confirming the obtained results and have a broader understanding about the properties of a particular material or a final device.

In Chapter 3, the *in-situ* and *ex-situ* ellipsometry analysis of the molybdenum films grown on different substrates have been discussed and correlated with Hall Effect measurement and AFM analysis. XRD and SEM analysis have been presented to study the structural properties of the films. It was shown that whatever the substrate, we had a Volmer-Weber growth grain size around 4-5 nm and conformal deposition. SIMS depth profiles of sodium through molybdenum and CIGS films were presented and compared between SLG and BSG substrates. Substrates with Na lead to film with lower resistivity and high amount of Na throughout them. Finally, the solar cells fabricated on SLG and BSG substrates were presented to illustrate the influence of sodium on device performance.

In Chapter 4, the effect of substrate temperature on sputtered molybdenum films were demonstrated. XRD, SEM and AFM analysis have been done to present structural and surface morphology properties as a function of temperature. Hall Effect measurement is done to study the electrical characteristics. In addition, SIMS and XPS data are presented to demonstrate the chemical analysis. Chapter 4 also offers an overview of the theoretical model used in order to simulate and understand grain boundary diffusion mechanism for impurities like sodium, potassium, and oxygen through Mo films for different substrate temperatures. Overall, we observed that higher T_{SS} leads to larger grain size but not to change in surface roughness. The films overall have a similar resistivity except for the ones at RT which were higher. The SIMS depth profiles for the film with T_{SS}=100°C showed higher Na, O and K signals level, which might explain the difference in Na diffusion through the films via a link to MoOx. However, no change in chemical bounding was observed by XPS. The Sodium diffusion was well described with diffusion through grain boundary, with a model having a good fit for intermediate temperatures (100, 150, 200) allowing extraction of $D_{boundary}$ and D_{grain} for the first time.

In Chapter 5, the influences of annealing on bilayer molybdenum films used as back contact for CIGS solar cells were presented. XRD, SEM, and AFM techniques were used for studying the film properties. Hall Measurement was performed on these films as well. For chemical analysis, SIMS depth profile of different elements was performed and discussed thoroughly. CIGS solar cells fabrication processes, described in Chapter 1, were implemented to fabricate complete solar cell devices on these films and detail device analysis were presented. Overall, all characterizations (SEM, XRD, AFM, and SIMS) for the 100°C were consistent, in that it exhibits unusual behaviors, which might be due to any sort of chemical reaction happening during the growth process in the sputtering chamber. The RT device showed better device efficiency, mostly due to a lower R_S and J_0. Improvement in electrical properties for higher deposition temperature was not backed up by higher sodium diffusion in the film. Hence, no significant changes were observed from the devices performance specifically V_{OC} and FF.

6.2 Future Work

SIMS analysis, correlated with device analysis, for the films deposited on high temperature thick glass with and without sodium barrier would be an interesting addition for complete understanding of the diffusion process. It would also be interesting to introduce new diffusion models to accommodate different diffusion mechanisms that have been observed from the initial study and analysis. We would also need to do TEM analysis to extract grain size and grain boundary width, which are essential for absolute measurement and would help develop a better diffusion modeling. A new diffusion model for the bilayer films could also provide further insight on the effect of deposition pressure. Finally, changing the deposition pressure, duration, and temperature to fabricate different sets of bilayer films, allowing the control incorporation of Na, might allow enhancing the device performance.

REFERENCES

[1] J. K. Leggett. Half Gone: Oil, Gas, Hot Air and the Global Energy Crisis, Portobello Books (2005).

[2] A. Ken Zwiebel, The terawatt challenge for thin-film PV, NREL/TP-520-38350, 2005

[3] M.A OpenEI. Transparent Cost Database. Available from: http://en.openei.org/apps/TCDB/.

[4] C. A. Wolden, J. Kurtin, J. B. Baxter, I. Repins, S. E. Shaheen, J. T. Torvik, A. A. Rockett, V. M. Fthenakis, and E. S. Aydil , "Photovoltaic manufacturing: Present status, future prospects, and research needs". J. of Vacuum Science & Technology A: Vacuum, Surfaces, and Films, 29(3): p. 030801-030801-16, (2011).

[5] http://www.solar-frontier.com/eng/news/2015/C051171.html.

[6] J. A. Del Cueto, S. Rummel, B. Kroposki, C. Osterwald, and A. Anderberg, "Stability of CIS/CIGS Modules at the Outdoor Test Facility over Two Decades,", 33rd IEEE Photovoltaic Specialists Conference San Diego, California, May 11–16, 2008.

[7] G. G. Voorwinden, R. Kniese, and M. Powalla, "In-line Cu(In,Ga)Se2 co-evaporation processes with graded band gaps on large substrates," Thin Solid Films, vol. 431-432, pp. 538—542, 2003

[8] K. Ramanathan, R. Noufi, B. To, D. L. Young, R. Bhattacharya, M. A. Contreras, R. G. Dhere, G. Teeter "Processing and Properties of Sub-Micron CIGS Solar Cells" in Conference Record of the 2006 IEEE 41h World Conference on PV, 2006, p. 380.

[9] R. F. Pierret, Semiconductor device fundamentals, New York: Addison- Wesley Publishing Company, Inc (1996).

[10] K. D. G. I. Jayawardena, L. J. Rozanski, C. A. Mills, M. J. Beliatis, N. Aamina Nismy and S. Ravi P. Silva, "Inorganics–in- organics: recent development and outlook for 4G polymer solar cell", Nanoscale 5, 8411-8427 (2013).

[11] F. Haug, Edevelopment of CIGS superstrate thin film solar cells, Ph.D. Thesis, Swiss Federal institute of Tech. 2001.

[12] M K. Zweibel, Harnessing Solar Power: The Photovoltaics Challenge (Plenum Press, New York, (1990).

[13] A D. M. Chapin, C. S. Fuller, G. L. Pearson, "A new silicon p-n junction photocell for converting solar radiation into electrical power", J. Appl. Phys. 25, 676-677 (1954).

[14] M. A. Green, K. Emery, Y. Hishikawa, W. Warta, and E. D. Dunlop, "Solar cell efficiency tables (version 42)." Prog. Photovolt: Res. Appl. 21, 827 (2013).

[15] M. A. Green, “Third generation photovoltaics: solar cells for 2020 and beyond” Physica E 14, 65 (2002).

[16] W. Shockley, and H. J. Queisser, “Detailed Balance Limit of Efficiency of p-n junction Solar Cells”, J. Appl. Phys. 32, 510 (1961).

[17] Orgass, K., Schock, H. W., and Werner, J. H., “Alternative back contact materials for thin film Cu(In,Ga)Se_2 solar cells.” Thin Solid Films 431-432, 387 (2003).

[18] Scofield, J. H., Asher, S., Albin, D., Tuttle, J., Contreras, M., Niles, D., Reedy, R., Tennant, A., and Noufi, R., “Sodium diffusion, selenization, and micostructural effects associated with various molybdenum back contact layers for CIS-based solar cells.” In: Proc. of the 24th IEEE Photovoltaic Specialists Conference, pp.164, (1995).

[19] Scofield, J. H., Duda, A., Albin, D., Ballard, B. L., and Predecki, P. K., “Sputtered molybdenum bilayer back contact for copper indium diselenide-based polycrystalline thin-film solar cells.” Thin Solid Films 260, 26 (1995).

[20] Rockett, A., “The effect of Na in polycrystalline and epitaxial single-crystal $CuIn_{1-x}Ga_xSe_2$.” Thin Solid Films 480-481, 2 (2005).

[21] Al-Thani, H. A., Hasoon, F. S., Yang, M., Asher, S., Alleman, J. L., Al-Jassim, M. M., and Williamson, D. L., “The effect of Mo back contact on Na out-diffusion and device performance of Mo/Cu(In,Ga)Se_2/CdS/ZnO solar cells.” In: Proc. of the 29th IEEE Photovoltaic Specialist Conference (pp. 720). 2002.

[22] Kadam, A. A., Jahagirdhar, A. H., and Dhere, N. G., “Effect of stresses in molybdenum back contact film on properties of CIGSS absorber layer.” Mater. Res. Soc. Symp. Proc. 865, F14.13.1 (2005).

[23] Gordillo, G., Grizalez, M., and Hernandez, L. C., “Structural and electrical properties of DC sputtered molybdenum films.” Solar Energy Mater. Solar Cells 51, 327 (1998).

[24] Nagano, J, “Electrical resistivity of sputtered molybdenum films.” Thin Solid Films 67, 1 (1980).

[25] Miyata, N., and Akiyoshi, S., “Preparation and electrochromic properties of rf-sputtered molybdenum oxide films.” J. Appl. Phys. 58, 1651 (1985).

[26] Tinone, M. C. K., Haga, T., and Kinoshita, H., “Multilayer sputter deposition stress control.” Journal of Electron Spectroscopy and Related Phenomena (Netherland) 8, 461 (1996).

[27] Wada, T., “Microstructural characterization of high-efficiency Cu(In,Ga)Se_2 solar cells.” Solar Energy Mater. Solar Cells 49, 249 (1997).

[28] Assmann, L., Bernede, J. C., Drici, A., Amory, C., Halgand, E., and Morsli M., “Study of Mo thin films and Mo/CIGS interface properties.” Appl. Surf. Sci. 246, 159 (2005).

[29] Martinez, M. A., and Guillen, C., "Effect of r.f. sputtered Mo substrate on the microstructure of electrodeposited $CuInSe_2$ thin films." Surface Coatings and Technology 110, 62 (1998).

[30] "Photovoltaic Applications using Spectroscopic Ellipsometry", LOT Oriel Group, Europe, J.A. Woollam Co., Inc, (2008).

[31] K. Vedamr, Thin Solid Films, 313-314 (1998).

[32] "Guide to using WVASE 32, Spectroscopic ellipsometry data acquisition and analysis software", J.A. Woollam Co., Inc, (2008).

[33] Dieter K. Schroder, "Optical Characterization", Semiconductor Material and Device Characterization, 3rd edition, Arizona, United States, A John Wiley and Sons, Inc., Publication, Arizona, United States, (2006).

[34] V. Ranjan, "Enhancement of the deposition processes of $Cu(In,Ga)Se_2$ and CdS thin films via In-situ and Ex-situ measurements for Solar cell application," Ph.D. Thesis, The University of Toledo, USA (2010).

[35] R.M.A Azzam, N.M. Bashara, "Ellispometry and Polarized light", North Holland Publishing Company, England, (1977).

[36] Tompkins Harland G., "A user's Guide to Ellipsometry" Academic Press, Arizona, United States, (1993).

[37] Hiroyuki Fujiwara, "Spectroscopic Ellipsometry: Principles and Applications", John Wiley and Sons, Inc., Publication, (2007).

[38] K. Aryal, H. Khatri, R. W. Collins, and S. Marsillac, International Journal of Photoenergy, 723714, (2012).

[39] N. Kasai and M. Kakudo, "Springer series in chemical physics: preface," Springer Series in Chemical Physics, vol. 80, pp. 364– 365, (2005).

[40] R. V. Forest, E. Eser, B. E. McCandless, R. W. Birkmire, and J. G. Chen, "Understanding the Role of Oxygen in the Segregation of Sodium at the Surface of Molybdenum Coated Soda-Lime Glass," AIChE Journal, Vol. 60, No. 6, (2014).

[41] T. L. Bergman, A. S. Lavine, F. P. Incropera, and D. P. DeWitt, Introduction to Heat Transfer, New Jersey: John Wiley & Sons Inc. (2011).

[42] F. P. Incropera, D. P. DeWitt, T. L. Bergman, and A. S. Lavine, Fundamentals of Heat and Mass Transfer, New Jersey: John Wiley & Sons Inc. (2007).

[43] F. Kessler, D. Rudmann, *Solar Energy 77*, p. 685-695, 2004.

[44] Stöcker, "Taschenbuch der Physik", *Verlag Harri Deutsch*, 1998.

[45] S. M. Sze, "Physics of semiconductor devices", John Wiley& Sons press, New York, (1981).

[46] W. N. Shafarman, S. Siebentritt, and L. Stolt, "Cu(In,Ga)Se2 Solar Cells ." In: A. Luque, and S. Hegedus, (eds.), Handbook of Photovoltaic Science and Engineering, Wiley, NewYork, p.547 (2011).

[47] A.L. Patterson, "The Scherrer Formula for X-Ray Particle Size Determination", Physical review 56, 978 (1939).

[48] M. A. Contreras, B. Egaas, K. Ramanathan, J. Hiltner, A. Swartzlander, F. Hasoon and Rommel Noufi, “Progress toward 20% efficiency in CIGS polycrystalline thin-film solar cells”, Prog. Photovolt. Res. Appl. 7, 311-316 (1999).

[49] S. Marsillac, M. N. Sestak, J. Li and R. Collins, Advanced Characterization Technique for thin film Solar cells, “Spectroscopic Ellipsmetry”, (eds. D. A. Ras, T. Kirchartz, and U. Rau) Wiley-VCH Verlag GmbH& Co. KGaA, (2011).

[50] R. W. Collins, and B.Y. Yang,"In situ ellipsometry of thin-film deposition – implications for amorphous and microcrystalline Si growth." J. Vac. Sci. Technol. Bl, 1155 (1989).

[51] H. G. Tompkins, “A User’s guide to ellipsometry”, Academic press, New York, (1992).

[52] R. M. A. Azzam and N. M. Bashara, “Ellipsometry and Polarized light”, Holland, Amsterdam, 1977. Tompkins, “A User’s guide to ellipsometry”, Academic press, New York, (1992).

[53] H. Fujiwara, “Spectroscopic Ellipsometry: Principles and applications”, John Wiley & Sons Ltd, (2007).

[54] R.W. Collins and A.S. Ferlauto, in: Handbook of Ellipsometry. Edited by H.G. Tompkins and E.A. Irene, p. 94, (William Andrew, Norwich, NY, (2005).

[55] F. Wooten, “Optical properties of solids”, New York, Academic press, (1972).

[56] J. A. Stoke. L. R. Dahal, J. Li, N. J. Podraza, X. Cao, X. Deng, and R. W. Collins, “Optimization of Si:H multijunction n-i-p solar cells through the development of deposition phase diagrams”, Proc. 33rd IEEE Photovolt. Spec. Conf., IEEE, New York, Art No. 413 (2008).

[57] R. D. Guenter, “Modern Optics”, Wiley, (1990).

[58] D. Guettler, A. Chirila, S. Seyrling, P. Bloesch, S. Buecheler, X. Fontane, V. Izquierdo Roca, L. Calvo-Barrio, A. Perez-Rodriguez, J. Morante, A. Eicke, and A. Tiwari, “Influence of NaF incorporation during Cu(In,Ga)Se2 growth on microstructure and photovoltaic performance”, in 35th IEEE Photovoltaic Specialists Conference (PVSC), pp. 003420–003424 (2010).

[59] A. Rockett, J. S. Britt, T. Gillespie, C. Marshall, M. M. Al Jassim, F. Hasoon, R. Matson, and B. Basol, Na in selenized Cu(In,Ga)Se2 on Na-containing and Na free glasses: distribution, grain structure, and device performances, Thin Solid Films 372, 212 (2000).

[60] R. Scheer, H.W. Schock, “Chalcogenide Photovoltaics: Physics, Technologies and Thin Film Devices” Wiley-VCH Verlag GmbH & Co. KGaA, (2011).

TASNUVA ASHRAFEE

Department of Electrical and Computer Engineering
Old Dominion University
231 Kaufman Hall, Norfolk, VA 23529

Phone: 757-639-5492
E-mail: tashrafee@gmail.com
Website: tashrafee.weebly.com

EDUCATION

Ph.D.	Electrical Engineering Old Dominion University (ODU), Virginia, USA	GPA: 3.95/4.00
M.S.	Applied Physics, Electronics and Communication Engineering University of Dhaka, Bangladesh	GPA: 4.00/4.00
B.Sc.	Applied Physics, Electronics and Communication Engineering University of Dhaka, Bangladesh	GPA: 3.78/4.00

TECHNICAL SKILLS

- **Cleanroom Experience:**

Metal evaporation (thermal and electron-beam), sputtering (RF and DC), Atomic Layer Deposition, Chemical Bath Deposition

- **Characterization:**

I-V and QE measurements, Hall Effect measurement, 4-point Probe sheet resistance measurement, Profilometer, Secondary Electron Microscopy, Atomic Force Microscopy, X-ray Diffraction, In-situ and ex-situ Spectroscopic Ellipsometry

- **Simulation software:** COMSOL, LabView, wxAMPS, SCAPS
- **Tools:** Origin, major word processors, spreadsheet programs, presentation programs

WORK EXPERIENCE

- **Graduate Research Assistant,** Electrical and Computer Engineering, ODU, VA
- **Graduate Teaching Assistant,** Electrical and Computer Engineering, ODU, VA
  - **ECE 332: Microelectronic Materials and Processes**: Grading home works and assisting students with their course related problems
  - **ECE 387: Microelectronics Device Fabrication**: Instructed lab experiments; evaluated assignments
- **Lecturer,** Independent University, Bangladesh
  - **Taught Courses:** ECR 101: Electronics I, ECR 206: Solid State Electronics
  - **Advising** undergraduate students

GRADUATE COURSEWORK

Semiconductor Process Technology, Fundamentals of Solar Cells, Optical Fiber Communications, Non-thermal Plasma Engineering, Semiconductor Characterization, Electronic Materials, Advanced Instrumentation

SELECTED PUBLICATIONS

Journal

1. **T. Ashrafee,** T. Erickson, K. Aryal, G. Rajan, S. Karki, V. Ranjan, A. Rockett, R. W. Collins, S. Marsillac, "Study of Annealed Molybdenum Films as a Back Contact for CIGS Solar Cells," (in preparation 2017)
2. **T. Ashrafee,** Y. Erkaya, K. Aryal, G. Rajan, S. Karki, V. Ranjan, A. Rockett, R. W. Collins, S. Marsillac, "Study of ZnS Films Deposited by ALD Process with Alternative Sulfur Source," (in preparation 2017)
3. S. Karki, P. Paul, G. Rajan, **T. Ashrafee**, K. Aryal, P. Pradhan, R.W. Collins, A. Rockett, A.R. Arehart, S.A. Ringel, S. Marsillac, "In-situ and Ex-situ Characterizations of CIGS Solar Cells with KF Post Deposition Treatment," *IEEE Journal of Photovoltaics*, 7 (2016)
4. S. Haq, **T. Ashrafee**, M. Begum, T. Sharmin, N. Bhowmick, Z. H. Mahmood, "Room Temperature Synthesis and Characterization of Au Nanoparticles," *Advanced Materials Research*, 159 (2010)

Conference Proceedings

1. **T. Ashrafee,** K. Aryal, G. Rajan, S. Karki, V. Ranjan, A. Rockett, R. W. Collins, S. Marsillac, "Effect of Annealing on Molybdenum Films used as a Back Contact for $Cu(In, Ga)Se_2$ Solar Cells," *43rd IEEE Photovoltaic Specialists Conference*, June 2016, Portland OR
2. O. Ayala, **T. Ashrafee,** G. Rajan, S. Karki, K. Aryal, V. Ranjan, A. Rockett, S. Marsillac, "Modeling of the Effect of Substrate Temperature on Na Diffusion Through Molybdenum Films," *43rd IEEE Photovoltaic Specialists Conference*, June 2016, Portland OR
3. C. G. Bailey, S. Babcock, M. Lichty, G. Rajan, **T. Ashrafee**, S. Marsillac, S. Maximenko, R. J. Walters, E. McClure, B. L. Smith, S. M. Hubbard, "Thin-film vapor-liquid-solid growth of InP for III-V photovoltaics," *SPIE Photonic West*, January 2016, San Francisco, CA
4. **T. Ashrafee,** K. Aryal, G. Rajan, S. Karki, V. Ranjan, A. Rockett, R.W. Collins, S. Marsillac, "Effect of Substrate Temperature on Sputtered Molybdenum Film as a Back Contact for $Cu(In,Ga)Se_2$ Solar Cells" *42nd IEEE Photovoltaic Specialists Conference*, June 2015, New Orleans LA
5. G. Rajan, K. Aryal, **T. Ashrafee**, S. Karki, A. Ibdah, V. Ranjan, R.W. Collins, S. Marsillac, "Optimization of Antireflective coatings for CIGS solar cells via Real Time Spectroscopic Ellipsometry," *42nd IEEE Photovoltaic Specialists Conference*, June 2015, New Orleans, LA
6. K. Aryal, G. Rajan, **T. Ashrafee,** V. Rajan, P. Aryal, A. Rockett, R. Collins, S. Marsillac, "Real time Spectroscopic Ellipsometry Studies of ultrathin CIGS films deposited by 1-stage, 2-stage and 3-stage co-evaporation process," *40th IEEE Photovoltaic Specialists Conference*, June 2014, Denver, CO
7. K. Arya, Y. Erkaya, G. Rajan, **T. Ashrafee**, A. Rockett, R. W. Collins, S. Marsillac, "Comparative Study of ZnS Thin Films Deposited by CBD and ALD as a Buffer Layer for CIGS Solar Cell," *38th IEEE Photovoltaic Specialists Conference*, June 2013, Tampa FL